PERFORMANCE ANALYSIS OF EXHAUST AIR ENERGY RECOVERY WIND TURBINE

SEYEDSAEED TABATABAEIKIA

FACULTY OF ENGINEERING

UNIVERSITY OF MALAYA

KUALA LUMPUR

2016

PERFORMANCE ANALYSIS OF EXHAUST AIR ENERGY RECOVERY WIND TURBINE

SEYEDSAEED TABATABAEIKIA

THESIS SUBMITTED IN FULFILMENT OF THE REQUIREMENTS FOR THE DEGREE OF DOCTOR OF PHILOSOPHY

FACULTY OF ENGINEERING
UNIVERSITY OF MALAYA
KUALA LUMPUR

2016

UNIVERSITY OF MALAYA

ORIGINAL LITERARY WORK DECLARATION

Name of Candidate: **Seyedsaeed Tabatabaeikia**

(I.C/Passport No:

Registration/Matric No: **KHA130103**

Name of Degree: **Doctor of Philosophy**

Title of ~~Project Paper/Research Report/Dissertation/~~Thesis ("this Work"):

Performance Analysis of Exhaust Air Energy Recovery Wind Turbine

Field of Study: **Computational Fluid Dynamic**

I do solemnly and sincerely declare that:

(1) I am the sole author/writer of this Work;
(2) This Work is original;
(3) Any use of any work in which copyright exists was done by way of fair dealing and for permitted purposes and any excerpt or extract from, or reference to or reproduction of any copyright work has been disclosed expressly and sufficiently and the title of the Work and its authorship have been acknowledged in this Work;
(4) I do not have any actual knowledge nor do I ought reasonably to know that the making of this work constitutes an infringement of any copyright work;
(5) I hereby assign all and every rights in the copyright to this Work to the University of Malaya ("UM"), who henceforth shall be owner of the copyright in this Work and that any reproduction or use in any form or by any means whatsoever is prohibited without the written consent of UM having been first had and obtained;
(6) I am fully aware that if in the course of making this Work I have infringed any copyright whether intentionally or otherwise, I may be subject to legal action or any other action as may be determined by UM.

Candidate's Signature Date:

Subscribed and solemnly declared before,

Witness's Signature Date:

Name:
Designation:

ABSTRACT

Recovering energy from exhaust air systems is an innovative idea. A specific wind turbine generator has been designed in order to achieve this goal. This device consists of two Giromill vertical axis wind turbines (VAWT) combined with four guide vanes and two diffuser plates. The working principle of this design was simulated using the ANSYS Fluent computational fluid dynamics (CFD) package and the results were compared to the experimental ones. The result shows that the optimum position of wind turbine that produces the highest power is when the shaft of the turbine is shifted 150 mm from the centre of discharge outlet. The theoretical analysis also shows that the turbine produces highest power at this position because the positive torque area of the turbine match the highest wind velocity from the cooling tower model. It was perceived from the results that by introducing the diffusers and then the guide vanes, the overall power output of the wind turbine was improved by approximately 5% and 34%, respectively, compared to using VAWT alone. In the case of the diffusers, the optimum angle was found to be 7°, while for guide vanes A and B, it was 70° and 60° respectively. These results were in good agreement with experimental results obtained in the previous experimental study. Overall, it can be concluded that exhaust air recovery turbines are a promising form of green technology. The optimization was carried out in the next step. It was aimed to optimize the overall system energy generation and simultaneously guarantee that it does not violate the cooling tower performance in terms of decreasing airflow intake and increasing fan motor power consumption. The variable factors for the optimization are the wind turbine rotor position, modifying diffuser plates, and the introduction of separator plates to the design. The generated power coefficient was selected as optimization objective. Unlike most of previous optimizations in the field of wind turbines, response surface methodology (RSM) as a method of analytical procedures optimization has been

utilised in this study by using multivariate statistic techniques. Both computational and optimization results were validated by experimental data obtained in the laboratory. Results showed that the optimization strategy could improve the wind turbine generated power by 48.6% compared to baseline design. Meanwhile, it is able to enhance the fan intake airflow rate and decrease fan motor power consumption. The obtained optimization equations were also validated by both CFD and experimental results and a very good agreement is achieved.

ABSTRAK

Pemulihan tenaga daripada system ekzos udara adalah suatu idea yang inovatif. Sebuah generator kincir angin telah direka untuk mencapai matlamat tersebut. Peranti ini terdiri daripada dua Giromill Kincir Angin Berpaksi Menegak (VAWT) digabungkan dengan empat bilah pandu dan dua plat resapan. Prinsip kerja reka bentuk ini disimulasikan menggunakan pakej Dinamik Bendalir Berkomputer (CFD) ANSYS Fluent dan keputusannya dibandingkan dengan keputusan eksperimen lain. Keputusan eksperimen menunjukkan kedudukan optimum kincir angin bagi menghasilkan kuasa tertinggi adalah apabila shaf kincir angin tersebut berkedudukan 150 mm dari pusat saluran discaj. Analisis teori juga menunjukkan bahawa turbin menghasilkan kuasa tertinggi pada kedudukan tersebut kerana kawasan daya kilas positif sepadan dengan halaju angin dari model menara penyejuk. Keputusan mendapati dengan menggunakan peresap dan bilah pandu, penjanaan kuasa keseluruhan kincir angin masing-masing meningkat kira-kira 5% dan 34% berbanding dengan menggunakan VAWT sahaja. Dalam kes penggunaan peresap, didapati sudut optimum adalah pada 7° manakala bagi bilah pandu A dan B masing-masing adalah pada 70° dan 60°. Keputusan ini adalah selaras dengan keputusan eksperimen yang diperolehi dalam kajian sebelumnya. Secara keseluruhannya, dapat disimpulkan bahawa ekzos pemulihan turbin udara adalah suatu kaedah yang boleh diharapkan untuk teknologi hijau. Langkah seterusnya adalah untuk mendapatkan konfigurasi yang optimum bagi penjanaan tenaga yang optimum tanpa memberikan kesan yang negatif terhadap prestasi menara penyejuk terutama dari segi penggunaan kuasa dan kadar aliran udara. Kedudukan rotor kincir angin, modifikasi plat-plat peresap, dan penambahan plat-plat pemisah dalam reka bentuk dianggap sebagai faktor berubah untuk pengoptimuman. Kecekapan penjanaan kuasa oleh kincir angin adalah objektif pengoptimumn ini. Dalam kajian ini, metodologi respon permukaan (RSM) sebagai kaedah analitikal digunakan dalam proses pengoptimuman

menggunakan teknik-teknik statistik yang multivariat. Kedua-dua pengiraan dan keputusan pengoptimuman disahkan oleh data percubaan yang diperolehi dalam ujian makmal. Keputusan menunjukkan bahawa strategi optimum boleh meningkatkan penjanaan kuasa kincir angin menjanakan kuasa sehingga 48.6% berbanding dengan reka bentuk biasa. Sementara itu, ia mampu meningkatkan kadar aliran udara dan mengurangkan penggunaan kuasa motor kipas. Rumus pengoptimuman yang diperolehi juga disahkan oleh kedua-dua CFD dan hasil percubaan dan satu persetujuan sangat baik dicapai.

ACKNOWLEDGMENTS

In the name of God, the almighty, the all wise.

This dissertation would not have been possible without the guidance and help of several individuals who contributed and extended their valuable assistance in the preparation and completion of this study.

First and foremost, I would like to express my sincere gratitude to my supervisor, Dr. Nik Nazri Nik Ghazali for the guidance, support and most importantly, the opportunity to undertake my PhD. He provided me with an outstanding atmosphere for doing research. Without his encouragement and effort, this thesis would not have been completed. Thanks to my Co-supervisor, Dr. Chong Wen Tong, for his academic guidance and exceptional moral support during my study. Without his encouragement and effort, this thesis would not have been completed. All their support inspired me to hurdle all the obstacles in the completion of this research work.

I also would like to thank all members of the Advanced Computational Laboratory and Renewable Energy & Green Technology Laboratory. The members have always been dear friends and may our path crossed over sometime in the future.

Thanks to Ministry of Education Malaysia that financially supported my tuition fee and living allowance through Malaysian Technical Cooperation Programme (MTCP).

My deepest gratitude goes to my family for their unflagging love and support throughout my life; this dissertation was simply impossible without them. I cannot find words to express my gratitude to my parents who spared no effort throughout my life to provide the best possible environment for me to grow up and achieve my goals in life. I admire the unconditional love and constant support of my wife, Noushin. She, like an intimate friend, shared all my joy and sorrow during my study. None of my achievements would have been possible without her support.

TABLE OF CONTENTS

LIST OF FIGURES

LIST OF TABLES

LIST OF SYMBOLS AND ABBREVIATIONS

A	Swept turbine area
BEM	Blade element momentum
CFD	Computational fluid dynamics
$C_{t,\ average}$	Average of mechanical torque coefficient
$C_{p,\ average}$	Average power coefficient
F_T	Tangential force
GIT	Grid independency test
k	Kinetic energy
L	Turbulent length
R^*	Monotonic divergence
P	Dynamic pressure
SST	Shear stress transport
URANS	Unsteady Reynolds averaged Navier-Stokes
U	Air velocity
VAWT	Vertical axis wind turbine
W	Relative velocity
Greek	
α	Diffuser angle
β	Angle of guide-vane A
θ	Azimuth angle
λ	Tip speed ratio
μ	Viscosity
ν_{eff}	Effective kinematic viscosity
ρ	Density
ψ	Angle of guide-vane B
ω	Angular velocity

LIST OF APPENDICES

CHAPTER 1: INTRODUCTION

This chapter will introduce the necessity and importance of this research and lay out the aims and objectives of the work. The layout of the remainder of this thesis will be addressed as well.

1.1 Necessity of a Wind Turbine in Urban Areas

In the current era, due to the limitation of fossil fuels and environmental concerns such as carbon emission and global warming, there is a considerable impetus to find more sustainable energy sources. Among all of the sustainable forms of energy, the application of wind energy has increased rapidly because it is not only renewable and abundant but also environment-friendly. Therefore, it causes no atmospheric emissions causing acid rain or global warming related issues (Manwell et al., 2010). One of the closest competitors to wind energy is solar energy that has its own ramifications—it heats up the atmosphere and causes air movement.

However, in comparison with the overall demand for energy, the scale of wind power usage is still trivial; in particular, the level of development in Malaysia is extremely low due to various reasons (Commission, 2014). For one, local suitable areas suitable for wind power plants are limited and the average velocity of the local wind is low (Sung, 2013). Therefore, the development of a new wind power system to generate a higher power output, especially in areas with lower wind speeds and complex wind patterns, is an urgent demand.

In order to address this issue, various innovative designs have been proposed to either augment energy generation of existing wind turbines (Chong et al., 2013; Chong et al., 2013; Foreman, 1981; Foreman and Gilbert, 1979; Foreman et al., 1978; Moeller and Visser, 2010; Ohya and Karasudani, 2010), or harvest wind generated from

unnatural sources (Chong et al., 2011). One of these innovative designs is called an exhaust air energy recovery wind turbine generator in which the high-speed wind, exhausted from a cooling tower fan, is considered as the source of energy. The objective of this study is to achieve the optimum design for this wind turbine using computational fluid dynamic (CFD) simulation.

To achieve the highest performance of the exhaust air energy recovery wind turbine, its aerodynamic performance has to be investigated first. There are two main ways to determine the aerodynamic performance, the experimental and numerical simulation. The numerical approach can be reached by several methods such as CFD simulation, Blade Element Momentum (BEM) theorem, and Golstein's vortex theorem (Shahizare et al., 2016a; Shahizare et al., 2016b). An experimental and numerical study on aerodynamic characteristics of an H-Darrieus turbine using BEM theorem was carried out by Mertens et al. (2003). A blind study comparison was also arranged by the National Renewable Energy Laboratory (NREL) (Simms et al., 2001) on a two-bladed horizontal axis wind turbine (HAWT) in a NASA-AMES wind tunnel under different operating conditions. Although, even in the simplest working operating condition the BEM predictions showed a 200% deviation from the experimental values, CFD codes consistently presented better performance.

In order to perform the CFD simulation of vertical axis wind turbines (VAWT), the Unsteady Reynolds Averaged Navier Stokes (URANS) equations are needed to be solved (McTavish et al., 2012). In simulation studies, the numerical predictions are compared to results of experimental tests to validate the applied numerical methods. In the case of VAWT simulation, the power coefficient is generally chosen for results analysis (Chowdhury et al., 2016). Testing a large model in the laboratory is not practical. Hence, some researchers (Qin et al., 2011) have validated their CFD methods on small scale turbines. Although for two-dimensional (2-D) simulation a large

discrepancy could be seen, by considering the cost of simulation, the result can still be satisfactory.

From previous experimental studies of Chong et al. (2014), it was concluded that this new invention is not only capable of recovering 13% of the energy but also it does not give any significant negative impacts on the cooling tower performance provided that it is installed in a correct position. The optimum position of the VAWT rotor was also experimentally tested by Fazlizan et al. (2015). It was shown that the best vertical and horizontal distances from the exhaust fan central axis are 300 mm and 250 mm respectively. In another experimental study, Chong et al. (2014) also discussed the effect of adding diffuser plates and guide vanes on the power output.

The works discussed above regarding the exhaust air energy recovery wind turbine are mostly experimental and analytical. The CFD validation regarding these experimental data has not been reported yet.

1.2 Aim and Objectives

In this study, an exhaust air energy recovery wind turbine generator is introduced. Two methods of computational fluid dynamic (CFD) and experimental are used to validate the performance of the exhaust air energy recovery wind turbine. This study aims to define and optimise the potentials of this novel wind turbine in order to achieve higher generated power.

The study has the following objectives:

- Identifying the parameters of scaled recovery system model to carry out aerodynamic analysis of them and determining the system performance.
- Optimising the novel recovery system structures by considering each parameter effect and creating the final model.
- Determining the performance of the ultimate model and validating it.

- Investigating the technical and economic feasibility of the exhaust air energy recovery wind turbine generator and its possible effect on the cooling tower performance.

1.3 Thesis Layout

This thesis addresses the flow investigation and optimisation of a novel wind turbine exhaust air recovery wind turbine, designed to be used in urban areas, using CFD and experimentation. The work is divided into seven chapters including a conclusion chapter presents the research contribution summary as well as suggestions for further work. Each chapter is broken down as follows:

- Chapter 2 consists of a critical literature review on the relevant areas, including the conventional wind turbines development, flow characteristics in built-up areas, and existing urban wind turbine technologies. A discussion is also carried out to; firstly, evaluate the disadvantages of current wind turbines and then to understand the significance a novel wind turbine development.
- Chapter 3 introduces the methodologies used to analyse the wind turbines performance.
- Chapter 4 evaluates the design concept and model parameters of the novel exhaust air energy recovery system. The performance of the novel wind turbine is also determined by CFD modelling and then validated by experimental test. Furthermore, the effects of diffuser plates and guide vanes on the system performance are investigated.
- Chapter 5 addresses the optimization of the exhaust air recovery system and validation of the optimization results.
- Chapter 6 details the technical and economic feasibility of the system.

- Chapter 7 presents the conclusions, research contributions, and then makes suggestions for the further work.

CHAPTER 2: URBAN WIND TURBINES DEVELOPMENT

This chapter will present and estimate the available wind turbines to define their pros and cons in application for built-up areas. In addition, the requirements of an appropriate urban wind turbine have also been discussed.

2.1 Introduction to Wind Turbine

Since early recorded history, the application of wind energy was in the form of vertical axis windmills that could be found thousands of years ago at the Persian-Afghan borders around 200 BC (Carlin et al., 2003). Windmills in the form of horizontal axis were later (1300-1875 AD) spread to the Netherlands and the Mediterranean countries (Fleming and Probert, 1984). The most significant wind turbine development milestone was reached in 1973 after the oil crisis once the U.S government decided to get involved in the wind energy research and development (de Carmoy, 1978; Thomas and Robbins, 1980). Nowadays, the modern wind turbine is defined as a machine that generates electricity from wind energy.

The horizontal axis wind turbines are the most widely used kind of modern wind turbines. The transformation process of these modern wind turbines is based on a net positive torque on a rotating shaft, which is produced by the aerodynamic lift force. Then, the mechanical power generated by the torque is transformed to electricity using a generator. Indeed, the wind energy can only be harnessed at the locations with specific wind characteristics. In general, the wind conditions of countryside or coast areas are more appropriate for electricity generation. Thus, most of the modern wind farms are situated far from cities. Due to the remote locations of wind farms, the cost of energy transit has been increased. Thus, the researchers vigorously attempt to move wind farms as close as possible or even inside urban areas.

However, there is also a huge amount of wind resources in urban areas. Implementing urban wind turbines not only makes it possible to capture wind energy at locations with high-energy demands but also is able to reduce the cost and waste during electricity transit significantly. Before moving into urban wind turbines, conventional wind turbine structures and features are reviewed briefly and the pros and cons of applying conventional or small-scaled conventional wind turbines are discussed.

2.2 Conventional Wind turbines

2.2.1 Lift and Drag Force Wind Turbines

According to driving forces, the wind turbines can be categorised into two types, drag machines and lift machines. In the drag machines, the drag force is utilised to generate power. The windmills used in the Middle East more than a thousand years ago (Miller, 1988) are an example of this type of turbines. The lift machines exploit the lift force to generate powers and they are the most commonly used modern commercial wind turbines. Conventionally, lift-driven turbines generate higher power comparing to drag force ones. Therefore, the lift force turbines are the most widely commercialised wind turbines. Although, the drag force turbines had been utilised thousands of years the lift force ones, due to their low efficiency, their usage was not as widespread as lift force ones. Fundamentals and the working principles of these two types of wind turbines explain the reason. Figure 2.1 shows the flow through a drag force wind turbine where U is the undisturbed airflow speed, ω is the rotor angular velocity and r is the rotor radius.

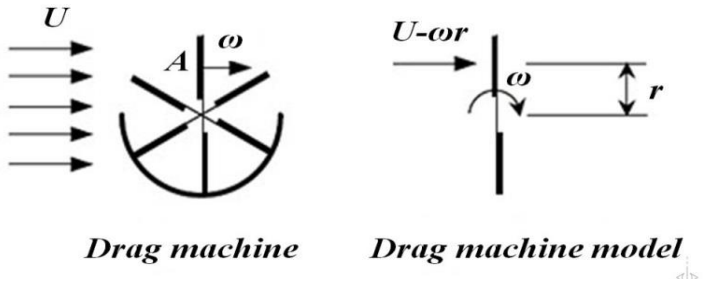

Figure 2.1: Simple drags machine and model (Zhang, 2014)

The drag force (F_D), can be shown as a function of the relative wind velocity at the rotor surface as below:

$$F_D = C_D[\frac{1}{2}\rho(U-\omega r)^2 A] \tag{2.1}$$

Where A is the drag surface area and C_D is the three-dimensional (3D) drag coefficient.

A torque is generated by the drag force and rotational velocity of the rotor, so that the power output can be defined as a function of blade radius (r):

$$P = C_D[\frac{1}{2}\rho A(U-\omega r)^2]\omega r = (\rho A U^3)[\frac{1}{2}C_D\lambda(1-\lambda)^2] \tag{2.2}$$

The power coefficient can also be presented as a function of the tip speed ratio (λ):

$$C_P = [\frac{1}{2}C_D\lambda(1-\lambda)^2] \tag{2.3}$$

It can be perceived from equation 2.3 that, the power coefficient of a drag force wind turbine is zero when the tip speed ratio is either zero or one. The power coefficient reaches to its peak, 0.18, when $\lambda = 1/3$. It is obvious that the power coefficient is much lower than Betz limit of 0.593. This reason limits the application of pure drag force wind turbines in modern wind energy industry. The drag force wind turbines can never rotate faster than the wind velocity. Therefore, in these wind turbines, the relative wind velocity interacting with the blades (U_{rel}) is limited to the free stream and can be expressed as:

$$U_{rel} = U(1-\lambda) \qquad (\lambda\langle 1) \tag{2.4}$$

It can be understood from Equation 2.4 that the relative velocity (U_{rel}) of a drag force wind turbine is always lesser than the free stream flow (U). However, this phenomenon is vice versa for a lift force wind turbine in which the relative velocity (U_{rel}) is always greater than free stream flow (U). As a result, lift force wind turbines have usually higher efficiency than drag force wind turbines. The relative wind speed of a lift wind turbine is shown in Figure.2.2.

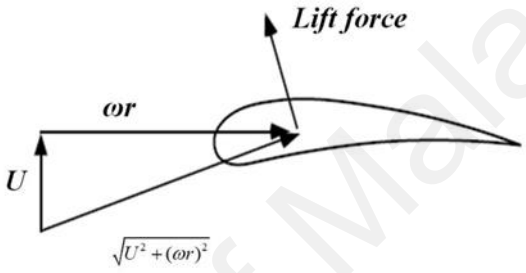

Figure 2.2: Relative velocity of a lift force wind turbine

From Figure.2.2, it can be inferred that the relative wind spee at the aerofoil of a lift machine can be expressed as,

$$U_{rel} = \sqrt{U^2 + (\omega r)^2} = U\sqrt{1+\lambda^2} \tag{2.5}$$

Equation 2.5 shows that in lift machines, the achievable relative wind velocity is much greater than drag machines. Since, the driving force is proportional to the relative velocity square, greater generated forces can be achieved by lift machines than drag ones with an identical surface area. One of the significant effective factors on wind turbines power generation is force. However, the maximum achievable power coefficient for some drag-based machines, such as the Savonius rotors, is about 0.18 and in some cases the tip speed ratios might be higher than 1.

2.2.2 Horizontal Axis Wind Turbine (HAWT) and Vertical Axis Wind Turbine (VAWT)

As mentioned earlier, the lift driven force wind turbines have potential to generate higher power coefficient. Therefore, they are the most commonly used modern commercial wind turbines. According to the direction of working axes, there are two types of lift-driven force wind turbines, namely horizontal axis wind turbine (HAWT) and vertical axis wind turbine (VAWT). Each type of wind turbines has its own advantages and disadvantages which makes them suitable for various conditions. The HAWTs have been considerably advanced and widely used over the last decades and are a dominant technology in modern wind energy industry. The higher energy efficiency of HAWTs has led to their wide application. However, this higher energy efficiency occurs only when the energy quality, wind speed and direction is high (Ghosh and Prelas, 2011). VAWTs are likely to demonstrate better operational performance in complex wind conditions, such as high wind turbulence, fluctuations and directional variability. Adequate and full consideration of all aspects such as sustainability and environmental matters will increase the applicability of wind energy. According to different structural features, the VAWTs are able to fulfil the energy generation necessities that cannot be obtained by HAWTs. The structural features of HAWTs and VAWTs have their own merits and drawbacks that significantly influence their application in urban areas.

2.2.2.1 Horizontal Axis Wind Turbine (HAWT)

Since the last decade, three-bladed horizontal axis wind turbines (HAWTs) are most frequently used wind turbines in the form of wind farms. HAWTs are widely applied due to their higher power coefficient compared to other turbines. As shown in Figure.2.3, in theory, the HAWTs power coefficient is very close to the curve of ideal efficiency. The main advantage of a HAWT is high power output compared to the

other wind turbines. However, HAWTs have also their own drawbacks due to their structural features complexity.

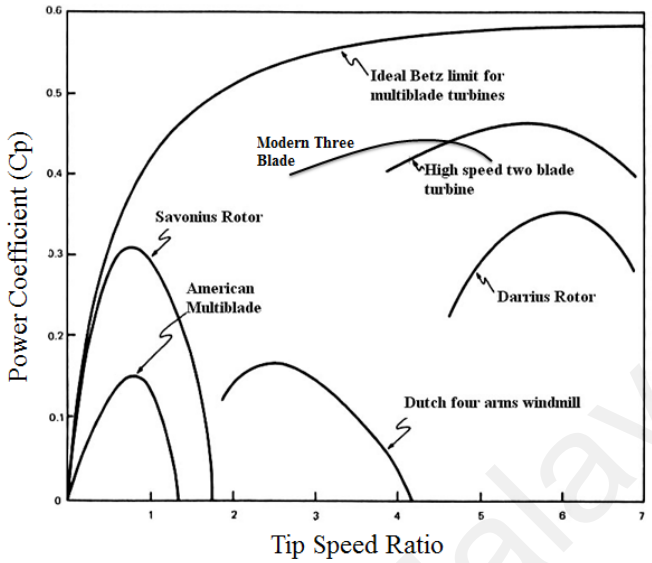

Figure 2.3: Rotor efficiency against tip speed ratios for different types of wind turbine (Schaffarczyk, 2014)

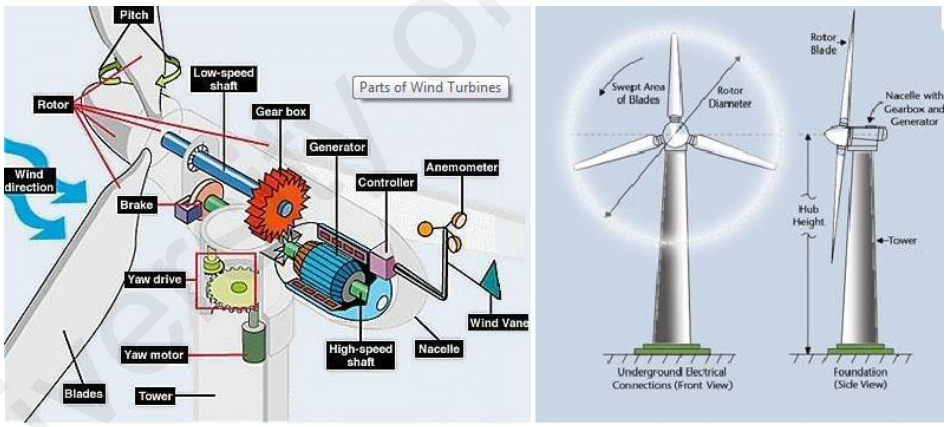

Figure 2.4: Wind turbine components (Khan, 2011)

Figure 2.4. shows the structure of a modern HAWT. The main rotor shaft and the generator are located on the top of a tower. An optimum power output can be achieved by applying a yawing mechanism to face the rotor to the unstable wind directions. The modern HAWTs yawing mechanism assists the blades to harness the maximum wind velocity through a computer controlled system. The height of a tower is another factor that influences the HAWTs power output. Indeed, a taller tower provides higher wind velocities approaching the wind turbine (Spera, 2009). However, their exceeding

height compromises their application in built-up areas. Moreover, increasing the HAWTs' tower height not only rises the transportation and installation costs but also the manufacturing cost will be swelled as the supporting tower needs to take the entire load from the blades, rotor and gear box on the top. Since HAWTs own several moving parts, the maintenance cost is also high (Mittal et al., 2010). In conclusion, HAWTs cannot be widely used in urban areas mainly due to their poor integration with urban environments.

2.2.2.2 Vertical Axis Wind Turbine (VAWT)

Most of the researches on modern VAWT design were done in the late 1970s and early 1980s (Williams et al., 2005). Later, it was revealed that HAWTs are more efficient; therefore, the interest in VAWTs was declined. However, researchers have recently regained interest in VAWT as there are various considerable advantages for VAWTs over HAWTs (Howell et al., 2010). Some of these merits are listed below:

- VAWTs do not require yawing constantly toward the wind directions.
- Since the VAWTs rotational speed is less than HAWTs, they emit less noise pollution.
- The manufacture cost of The VAWTs' blades are usually simpler and have constant sections so the fabrication cost is lower than HAWTs'.
- The VAWTs have a potential to withstand stronger winds through changing stalling behaviour therefore they have higher operational safety during gust conditions.

One of the major advantages of VAWTs is the low repairs cost. All VAWTs compartments are placed on the ground; therefore, they can be accessed at ease and quicker for maintenance purposes. The self-starting ability is another significant factor for a wind turbine in order to be used in urban areas (Van Bussel and Mertens, 2005).

However, poor self-starting capability is a significant drawback of VAWTs (Kirke, 1998). Conventionally, VAWTs have three or more blades, but not all of them will face the airflow direction. When the turbine blade movement and the wind directions are parallel, an extra load will be imposed on the blades causing negative or zero torque. Since VAWTs operate effectively in the case of highly uneven and turbulent wind flow patterns, they are the perfect candidates for small-scale uses in urban areas. Their axisymmetric nature facilitates wind energy extraction process when the wind direction is uneven. In addition, their base-mounted generator location allows comparatively easy maintenance procedure and it makes them more appropriate for small-scale installation in cities compared to conventional horizontal axis turbines.

Base on driving forces, vertical axis wind turbines can be divided into two categories, lift force and drag force. Initially, VAWTs operated as drag devices (Savonious) and only recently researchers have focused on the lift driven VAWTs after a French engineer, Darrieus, suggested the first lift driven VAWT in 1925 (Hau, 2013). Based on their own features, two types of VAWTs have been utilised in inner-city areas:

Darrieus wind turbines: The Darrieus wind turbines were first designed in 1931 (Paraschivoiu, 2002). Since this type of wind turbines is driven by the lift force, it owns the highest efficiency among VAWT types; however, its starting capability is poor. The Darrieus wind turbines are categorised as two major groups, egg-beater and Giromill turbine. Typical structures of Darrieus wind turbine are shown in Figure 2.5. With the maximum efficiency of 0.42, the performance of egg-beater Darrieus wind turbine is acceptable. The egg-beater type usage is limited due to the high complexity and cost of blades manufacturing (Eriksson et al., 2008). The Giromill turbine blades are straight blades so it is suitable for small-scaled and roof top applications. The Giromill turbines blades can have either fixed or variable pitch (Gorelov and Krivospitsky, 2008), and it

helps to tackle the low starting torque issue of VAWTs (Howell et al., 2010; Islam et al., 2008). The Giromill turbines power efficiency is around 0.23, which is relatively higher than other drag driving machines.

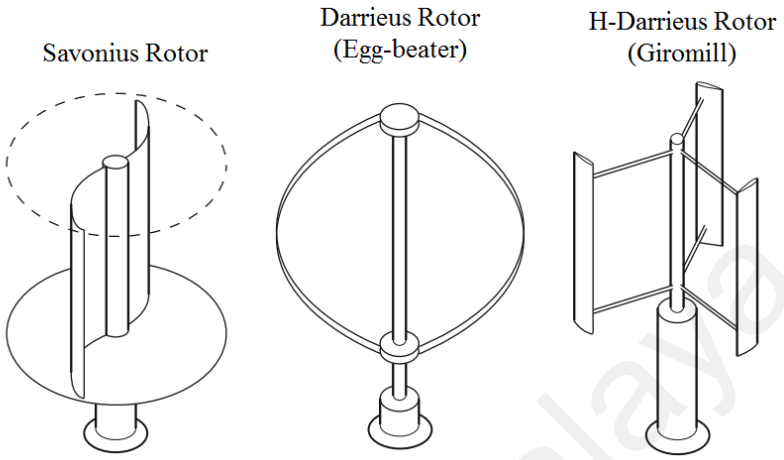

Figure 2.5: Types of vertical axis wind turbines

Savonius wind turbine: This type of drag force wind turbine was introduced by S.J. Savonius in the 1920s (Kyozuka, 2008). It typically comprises of cup-shaped half or hollow cylinders attached to a central rotating shaft. Figure 2.5 illustrates a typical Savonius wind turbine. The Savonius wind turbine owns the merits of VAWTs; however, its structure has been improved. These merits can be listed as follows (Akwa et al., 1992),

- Cheap and simple construction
- Operating in uneven flow directions
- Low tip speed ratio and low noise level
- low moving parts wear
- various rotor structure options
- High static and dynamic moment

The Savonius wind turbine efficiency is lower compared to Darrieus wind turbine efficiency and varies from 5% to 20% (Gorelov and Krivospitsky, 2008). Due to the

lower power efficiency, the Savonius wind turbine has not been commercialised and is generally used for wind velocimetry applications. According to the recently published results, operational conditions, geometric and airflow parameters affect the Savonius rotor performance significantly (Menet, 2004). It can thus be concluded that this type of wind turbine is not fit to be used in urban areas.

2.3 Urban Wind Turbines Requirements

The wind energy is one of the cheapest renewable sources with high potential to meet the energy consumption requirements in built-up areas. Wind turbine technologies and complex flow conditions in urban environment have limited the installation and applications of wind turbines in these areas. Previously, the restrictions of employing conventional wind turbines were addressed. In order to build an ideal urban wind turbine, urban wind characteristics should be first studied.

The wind characteristics in inner-city areas are intensely influenced by urban terrains. The complexity of achieving high power outputs for wind turbines in an urban area will be increased by three factors of low wind velocity, high turbulence intensity and frequent changing flow directions (Makkawi et al., 2009). In an urban area, low wind speed and high turbulence intensity are produced by ground topography, which is affected by buildings layouts and roofs geometries. Thus, utilising the wind energy in urban areas requires consideration of two important matters, location and installation. It can be perceived from the literatures (Abohela et al., 2013; Millward-Hopkins et al., 2013; Walker, 2011) that wrong location of a turbine on a building roof causes the diminishment of power output to zero for substantial periods of time even when the wind blows strongly. To find out the way to exploit wind energy in the inner-city areas, the flow characteristics affected by buildings have been studied intensively (Yang et al., 2016). Three factors, including roof geometry, building height and urban configuration, are able to decrease the urban wind turbines performance (Abohela et

al., 2013). The locations of wind turbines on different roof shapes are vital to take advantage of the increasing wind speed, which causes more energy to be captured. The impacts of several roof types and locations with various wind directions have been studied. In one study, three different roof types, namely pitched, pyramidal and flat one, were investigated in different directions of approaching flow (Ledo et al., 2011). Abohela et al. (2013) also indicated that the wind acceleration can be affected by various roof types. Some of roof types indicated the capability to increase streamwise velocity significantly and produce more energy. For instance, it was indicated that the flat roofs could provide a higher and more consistent power density than the other roof types. Mertens analysed and evaluated the effect of different heights of wind turbines located on buildings (Mertens, 2002). It was indicated that different building heights would cause almost identical flow patterns on top of the roof (Abohela et al., 2013).

However, considering the effects of ground roughness proved that an increase in the building height could increase the acceleration. In other words, high-rise buildings bring higher potentials in acceleration increment than shorter buildings. In recent years, the flow characteristics in urban environment have attracted more attentions so that many researches have been investigated the flow characteristics in urban areas. It was reported that the urban configuration influences the flow characteristics significantly (Baik et al., 2000). Another factor that affects the flow character is the interaction between buildings. These interactions are divided in two groups; first group considers buildings as roughness elements, therefore, the interactions between urban roughnesses, urban airflows and atmospheric boundary layer are investigated. Second group considers the urban airflow more microscopically within street canyons and urban canopies. Regarding the first group, the preliminary work was performed by Grimmond and Oke (1999) using the morphometric methods. In their study, the wind

profiles in various urban areas were reviewed and analysed. Moreover, available roughness parameter models were summarized. In order to determine the effects of various heights of buildings on flow velocity, several CFD simulations were carried out by Abohela et al. (2013). The simulation results proved that the buildings, where the wind turbines are installed, should be higher than surrounding ones.

The position of wind turbine can be notably affected by the details of flow around buildings. The simulation of flow characters around a single high-rise building was carried out by Abohela et al. (2013). It was elucidated by Murakami et al. (1988) that an approaching flow toward a building is separated into four main streams. The first stream is deviated over the building; the second one is diverged down the windward façade, while the other two are strayed to the two sides of the buildings. A stagnation point (*St*) with highest pressure is formed at flow deviation point, while flow changes the direction from the stagnation point to lower pressure zone. Figure 2.6 depicts the flow characters through a building found by Abohela et al. (2013). A horseshoe-shaped vortex was created on front face of the cube and extended along the sides (V_1). There are four main streams; downwards the windward facade (S_1), above the cube roof (S_2) and two sides stream (S_3). The approaching flow was detached and then reattached in the leeward direction of the cube (*Rx1*). It was remarked that the distance of the stagnation points (*St*) from ground is related to the building height, which in this study was around 0.8h. It was found that the maximum negative pressure occurs at the location of 0.05h from the windward edge of the roof. Accordingly, it was concluded that the free stream approaching building could cause two effects. One effects on acceleration of free stream flow velocity and the other increases in turbulence intensity. The acceleration of flow velocity results in increase of power output of a wind turbine. In contrast, increasing of turbulence intensity results in reduction of power output of a

wind turbine. Thus, these two parameters should be considered in installing wind turbines in urban areas.

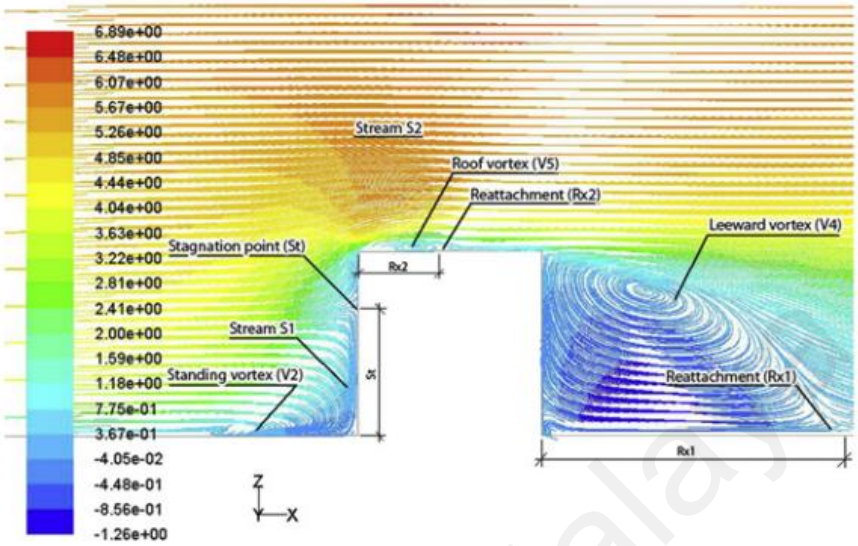

Figure 2.6: Streamwise velocity pathlines passing through the vertical central plane (Abohela et al., 2013)

Moreover, urban environments should also be considered for installation of urban wind turbine. In order to achieve widespread application of urban wind turbines, their integration with buildings should not be underestimated. Since these wind turbines are placed at high population density areas, safety and noise emission should be considered in their design. In fact, the high speed rotation of wind turbine blades can cause danger and noise pollution. There are two main sources of wind turbine noise. One is mechanical noise that is generated by the fans, generator and gearbox due to the vibration of the system. Another source of noise pollution is the aerodynamic noise caused by the interaction between the blades and wind. In recent years, the mechanical noise issue is almost solved hence many researches have been moved to aerodynamic noise (Göçmen and Özerdem, 2012; Laratro et al., 2016; Narayanan et al., 2015). Slowing down the wind turbine rotating speed is one of the efficient ways of noise reduction. The high rotating speed of a wind turbine can also be dangerous. Hence, the noise and safety problems can be solved if a wind turbine rotating speed is controlled.

To sum up, it can be concluded that, the safety and noise levels should be clarified to minimise the cautions of wind turbine installation for people. Unfortunately, the erroneous installation of rooftop wind systems without adequate consideration of safety, structural building integrity or turbine performance has caused a negative reputation of urban wind energy (Anderson et al., 2008).

2.4 Development of Urban Wind Turbines

Indeed, an efficient way to decrease carbon dioxide emission is to utilise wind energy in inner-city areas. Despite the abundance of wind energy resources in these areas, the wind energy usage is narrowed due to complex wind conditions. Applying the wind energy in such areas has become an attractive field for researches recently. In theory, it is estimated that over 30% of the UK's electricity supply could be provided using wind energy by the year 2025 (Kota et al., 2015). To date, several wind turbines with different structures, including micro HAWT wind turbines, ducted wind turbines and omni-direction-guide-vane wind turbines, have been productively installed in the built-up environments. Three possible wind turbine strategies were introduced by The EC-funded Project WEB (Campbell et al., 2001):

- Simply siting conventional wind turbines in a built-up area;
- Retro-fitting wind turbines installed on existing buildings;
- Specially designed wind turbines for better integration with buildings.

In the following sections, existing and developing concepts of urban wind turbines will be discussed according to these three possible strategies.

2.4.1 Simply Sitting Conventional Wind Turbines

There are three categories of conventional wind turbines such as large turbines (>1 MW), medium turbines (40kW-1MW) and micro turbines (<40kW) (Spera, 2009) according to the power output. The most obvious difference between micro and the

other two types of wind turbines is that the Micro wind turbines are installed where the power is needed. These micro turbines are normally located on the top of houses to generate power for the remote homes off the grid. Based on the market requirements, the developments of micro turbines have increased rapidly. These turbines are also divided in two categories of horizontal and vertical axis one. In the next section, these two types of simplified micro wind turbines will be introduced.

2.4.1.1 Micro Horizontal Axis Wind Turbine

On the contrary to large HAWTs, the micro-HAWTs are able to be installed on the roof tops of houses, remote populations and even boats (Syngellakis et al., 2006). The wind conditions of these places are not suitable for conventional wind turbines to generate power due to available obstacles and area topology that cause turbulence and slow down the flow. A good solution is application of the micro-HAWTs due to their acceptable start-up response to low speed winds. Nonetheless, the blade size of micro-wind turbines is relatively small and it limits their power generation capability. Implementation of multiple rotor blades can increase the starting torque and then improves their performance (Wood, 2004). Increasing the number of blades results in a quick start, thus the turbines can operate at much lower cut-in wind speeds. Consequently, there would be an increase in the micro-wind turbines efficiency. The other characteristics of rotors, including the chord length, twist distribution, number of blades, aerofoil profile and the tip speed ratio (λ), should also be optimised. Blade optimization makes the power coefficients of wind turbines close to the Betz limit of 59.2%. However, the main drawback is that HAWTs operate with yaw control systems that are costly and require high level of maintenance.

2.4.1.2 Micro Vertical Axis Wind Turbine

Although HAWTs are more efficient in operation, vertical axis wind turbines (VAWTs) play a significant role in the micro-wind turbines market (Gunnell et al.,

2009). Considering the structural feature, VAWTs offer greater advantages in terms safety and operation in built-up areas. Axisymmetric design of VAWTs and location of gearbox and generator on the ground make them much more suitable for urban environments (Dayan, 2006). Accordingly, two significant merits can be achieved. One is the easy access to perform turbine maintenance, and the other is reduced loads on the turbine tower that results in reduction of material installation costs. Savonius wind turbine is the most extensively used micro VAWT due to its low cost and reduced environmental impacts. The Savonius wind turbines work fundamentally based on wind drag forces but take advantages of lifting forces. These types of turbines perform in gust conditions when most of lift wind turbines require to be stopped (Vries, 1983). The Savonius turbine blade profiles also play a critical role in performance improvement. Thus, several blade profile types have been investigated and two notable types, namely Bach-type rotor and semi-circular blades, have shown the maximum power coefficient of 25%. The usage of Savonius wind turbines is still limited. It can be explained by two reasons. First, two uncontrollable situations in urban areas, such as flow conditions and flow parameters, strongly affect the performance of these wind turbines. Second, due to slow-running behaviour of Savonius wind turbines, they are not sufficient in energy generation (Menet, 2004).

2.4.2 Retro-Fitting Wind Turbine

Retro-fitting wind turbines refer to a group of small-scaled conventional HAWTs and VAWTs. Some attachable compartments have been designed and installed on the conventional wind turbines to enhance their suitability and productivity in built-up areas. There are two most popular retro-fitting wind turbines, the diffuser augmented wind turbines (DAWT) (Gilbert et al., 1978) and zephyr wind turbinse (Pope et al., 2010).

2.4.2.1 Diffuser Augmented Horizontal Axis Wind Turbine

In diffuser augmented wind turbines, horizontal axis wind turbine is surrounded by a diffuser structure to capture and concentrate the airflow (as shown in Figure.2.7). The primary idea of such wind turbines was suggested and studied by Gilbert et al. (1978) and Igra (1981). In their investigation, a large open angle diffuser was utilised to achieve wind flow concentration. In order to prevent the pressure loss caused by flow separation, the boundary layer control method was applied. Since the wind energy is proportional to the wind velocity cubed, even a minor rise in the approaching wind speed can improve power output significantly. The further work was performed by Bet and Grassmann (2003). In their research, a shrouded wind turbine with a wing-profiled ring structure was developed which almost doubled the system power output compared to the bare wind turbine. Ohya et al. (2008) studied the flanged diffuser wind turbines both computationally and experimentally. The flange part was attached at the diffuser outlet section to generate a low-pressure region near wake of the diffuser. Therefore, more mass flow can be sucked into the diffuser, which improves the wind turbine efficiency. In one study, the flanged diffuser wind turbine was investigated in real situation. It was shown that its performance can be increased by four to five times compared to the conventional wind turbine (Ohya et al., 2008). In addition, the diffuser structure not only can reduce the noise emission but also it improves the safety factor (Abe et al., 2005). Therefore, application of diffusers can improve the appropriateness and efficiency of HAWTs in urban areas.

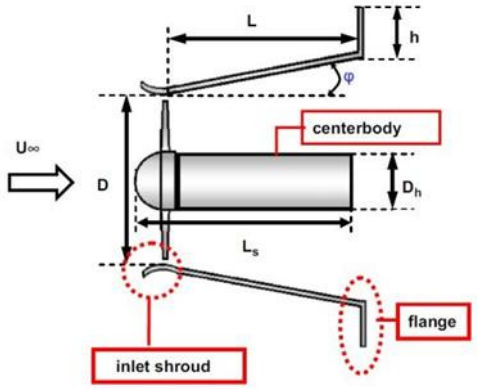

Figure 2.7: Flanged diffuser wind turbine (Ohya et al., 2008)

2.4.2.2 Zephyr Vertical Axis Wind Turbine with Stator Vanes

Previous studies showed that efficiency of VAWT is dramatically lower than HAWT. Many researches have been carried out to improve the VAWT performance. One of the notable improvements in VAWT has been the introduction of the zephyr vertical axis wind turbines that use stator vanes (as shown in Figure.2.8). The flow conditions approaching the wind turbine can be optimized by stator vanes. The flow is first guided through a ring of still stator blades to modify the angle of incidence and accelerate the wind velocity. Hence, the flow can reach to the rotor blades in a specific direction to improve the wind turbine performance. By implementing stator vanes, the flow turbulence and consequently the aerodynamic loading on turbine blades can be reduced (Pope et al., 2010). The theoretical and practical analyses were performed by Pope et al. (2010). In their study, the power coefficient is determined about 0.12, which is not acceptable for commercial applications. However, power coefficient improvement of whole system can be obtained by optimization of prototype parameters, including design of blades, stator vanes and the distance between stator ring and rotor. Pope et al. (2010) derived some equations which relates to the power coefficient to tip speed ratio (λ). It was indicated that the maximum value of power coefficient could be achieved at $\lambda=0.4$ and it decreases for higher values of λ. These outcomes are useful for further development of the prototypes.

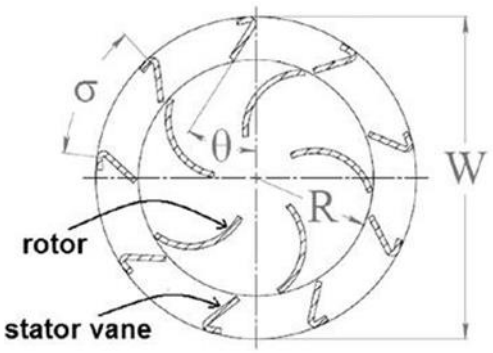

Figure 2.8: Sketch of zephyr wind turbine with stator vanes (Pope et al., 2010)

2.4.3 Specially Designed Wind Turbines

Although some improvements have been obtained by attached structures, conventional wind turbines still owns some inherent limitations resulted from their structural features. Many researches on innovation of urban wind turbines have been studied recently. These newly designed wind turbines are applicable in urban areas. In design procedure of such new wind turbines the merits of available wind turbines and complex flow conditions in built-up areas have been considered. This approach has resulted in three remarkable designs, including ducted, crossflex and vertical resistance wind turbines.

2.4.3.1 Ducted Wind Turbine

The ducted wind turbine is an alternative to conventional wind turbines to be applied in inner-city areas. The original concept of this wind turbine was introduced as a patent by Webster (1979) as depicted in Figure 2.9. Generally, an extreme turbulence is generated by buildings so the duct was designed to protect wind turbine from this turbulence. A high-pressure zone is formed on vertical walls facing the on-coming wind, while a low-pressure one is generated along the building roof. It is well proven that the wind velocity and direction are affected by pressure difference.

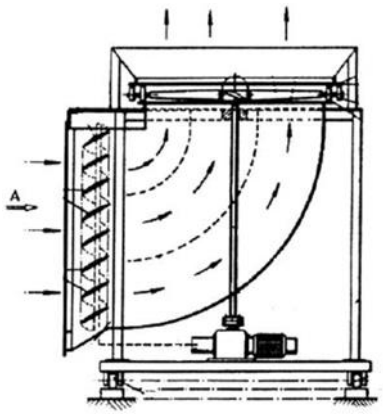

Figure 2.9: Original ducted wind turbine from patent by Webster (1979)

The ducted wind turbine exploits the available pressure difference generated by the wind flow around and over a building to push air through wind turbine. Many researches were performed to determine and improve the ducted wind turbine power output. A single unit of ducted wind turbine was analysed for a long period (Grant and Kelly, 2003) and then its effectiveness and robustness in operation was investigated. Dannecker and Grant (2002) performed a wind tunnel test on both curved and straight ducts to determine report their potential performance. In another study, Grant et al. (2008) developed a mathematical model to predict the power outputs under the usual operating circumstances. Then, the accuracy of mathematical model was validated by experimental work. It was shown that, this wind turbine is a feasible alternative to small-attached conventional devices to the buildings roofs. The duct structure has also a considerable potential to excess the conventional Betz limit.

2.4.3.2 Crossflex Wind Turbine

Sharpe and Proven (2010) designed the crossflex wind turbine to fulfil the requirements of turbines in urban areas. It is a new modification of Darrieus wind turbine owing flexible blades system. The vertical shaft on crossflex wind turbine is responsible to work in various flow directions and some flexible aerofoil blades are attached to the top and bottom of this rotating shaft. Figure.2.10 shows the conceptual design of a crossflex wind turbine. To enhance the efficiency, blades whit low solidity

and low internal mass can be utilised. The crossflex turbine structure is deemed to have the capability to achieve not only a better self-starting ability, but also a reduction in loads on the shafts and bearings. The supporting structure of a crossflex wind turbine is rigid; therefore, the vibration is reduced. The capability to be installed at walls or corners of a building is one the merits of crossflex turbines. Thus, a significant installation capacity per building can be attained. Another important factor of crossflex wind turbine is that they have a good integration with buildings. Sharp and Proven (2010) were examined the theoretical modelling of crossflex wind turbine using the multiple streamtube momentum balance approach. The wind turbine prototypes were also examined at Newberry tower in Glasgow, Scotland. It was found that the high-rise buildings are the most appropriate locations to install crossflex wind turbines; therefore, they are not suitable to be utilised in wind farm arrangements or on short buildings. Experimental studies revealed that flow velocity should be higher than 14 m/s to achieve the highest power output from crossflex wind turbines. Hence, it was suggested that their installation is only suitable in the area where free stream velocity is greater than 14 m/s. Further investigation is required to improve their performance in low flow speed conditions.

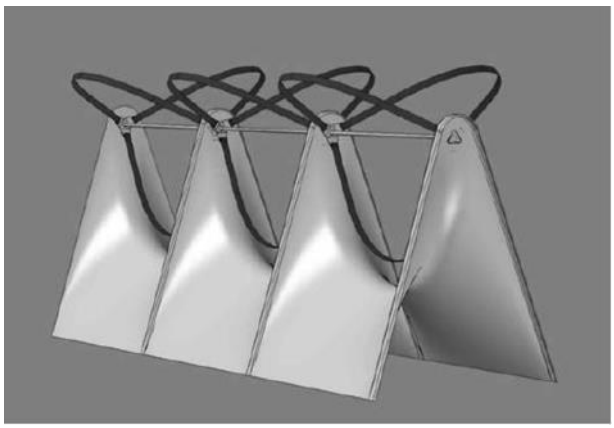

Figure 2.10: Concept of crossflex wind turbine (Sharpe and Proven, 2010)

2.4.3.3 Vertical Resistance Wind Turbine

The vertical resistance wind turbine is a typical structure of drag force VAWT. Since VAWTs perform better in the turbulent wind conditions found in an urban area, they are capable to be implemented in urban environment (Dayan, 2006; Mertens, 2002). The drag force based systems are expected to be less sensitive to turbulence and are less noisy as well. The history of using vertical resistance wind turbines goes back to thousands of years ago. Apparently, the oldest one is the so-called "*Persian"* windmill that was recorded in 9th Century AD in the area of Sistan in eastern Persia (Hau, 2013). The vertical resistance wind turbine was first modified to be used in urban environment by Muller et al. (2009). Utilising disks and pressure difference were two significant modifications proposed by Muller and colleagues. In order to increase the drag coefficient, two disks were located at the top and bottom of the turbine body. Theoretically, this modification is able to increase the drag coefficient from 1.2 to 2, results in 29.6% increment in the maximum efficiency. Figure 2.11 illustrates the conceptual design of a vertical axis resistance wind turbine. During the blades rotation, high-pressure and low-pressure zones are generated on the side of the obstacle facing the flow direction zone and on the lee side respectively. This pressure difference significantly affects the wind turbines performance. In resistance energy converters, the pressure difference is considerably high; therefore, the overall performance of this wind turbine is high. Muller et al. (2009) carried out theoretical and experimental studies on a specially designed wind turbine. In the theoretical study, it was indicated that the maximum efficiency of the resistance vertical axis wind turbine was about 48-61% and it was measured about 42% in the experiment. It was also showed that the wind turbine efficiency could even be increased 6% to 7% by increasing the blades number from four to six. The most significant merit of the

vertical resistance wind turbine is its components simplicity compared to other urban wind turbines.

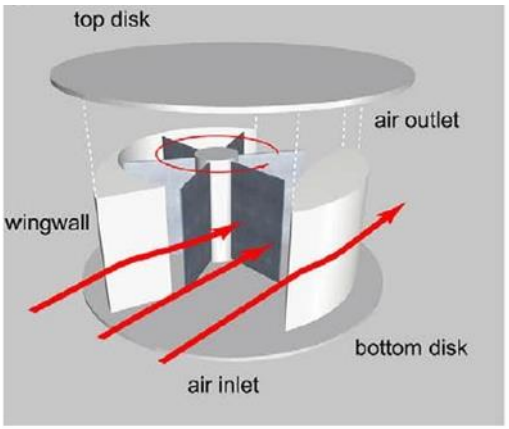

Figure 2.11: Concept of vertical axis resistance wind turbine (Müller et al., 2009)

2.4.4 Recovering Energy from Unnatural Wind Sources

The Unnatural wind is considered as the air movement that is available from the manufactured systems or operations such as cooling tower, exhaust air and other ventilation systems. The high-speed, consistent and predictable wind produced by such systems is suitable to be recovered into energy. Natural wind is neither available nor reliable enough to be utilized for electrical energy generation in many cases. Most of the countries situated in the equatorial region, like Malaysia, experience low wind speed throughout the year (Tan et al., 2013). Extracting wind energy by using conventional wind turbine in this situation does not seem to be feasible. Therefore, innovative ideas of harnessing wind energy from unnatural wind resources using on-site energy generators may be one of the ways to generate electricity for urban commercial buildings. The concept of on-site renewable energy generation is to extract energy from renewable sources close to the populated area where the energy is required (Chong et al., 2011).

As for energy recovery from wind resources, Berenda and Ferenci (1996) filed a patent on a system that captures and converts the wind energy to electrical energy using the horizontal axis wind turbine positioned in front of an exhaust fan. Referring to the

patent document, the exhaust air from a system is blown horizontally while the HAWTs are arranged in a line perpendicular to the exhaust wind flow. Another patent is presented by Cohen (2002) to generate electricity from an air conditioning exhaust. A shroud is mounted as an extension to the exhaust air outlet to enclose the discharge air. Wind from the outlet will rotate the turbine that is placed in the shroud. The system is likely to cause an obvious blockage effect to the outlet and the exhaust heat might accumulate at the shroud. Therefore, this might negatively affect the air conditioning exhaust performance.

2.4.5 Exhaust Air Energy Recovery Turbine Generator

One of the latest designs to recover energy from exhaust air systems was proposed and patented by Chong.et al. (2013). The earlier design of this invention can be seen in Figure 2.12. Later, several modifications were carried out in order to improve this exhaust air energy recovery wind turbine generator and minimize the blockage effect of it on the cooling tower performance. In some experimental studies, Chong et al. (2014) and Tan et al. (2013) concluded that this new invention is not only capable to recover the energy by 13% but also it does not impose any significant negative impacts on the performance of the cooling tower if it is installed in the correct position. The most optimum position of the VAWT rotor is also experimentally tested by Fazlizan et al. (2015). It was shown that the best vertical and horizontal distance from the exhaust fan central axis is at 300 mm and 250 mm respectively. In another experimental study, Chong et al. (2014) discussed the effect of adding diffuser plates and guide vanes on the power output. The works discussed above regarding the exhaust air energy recovery wind turbine are mostly experimental and analytical. No computational and numerical validation regarding to these experimental data have not been reported yet.

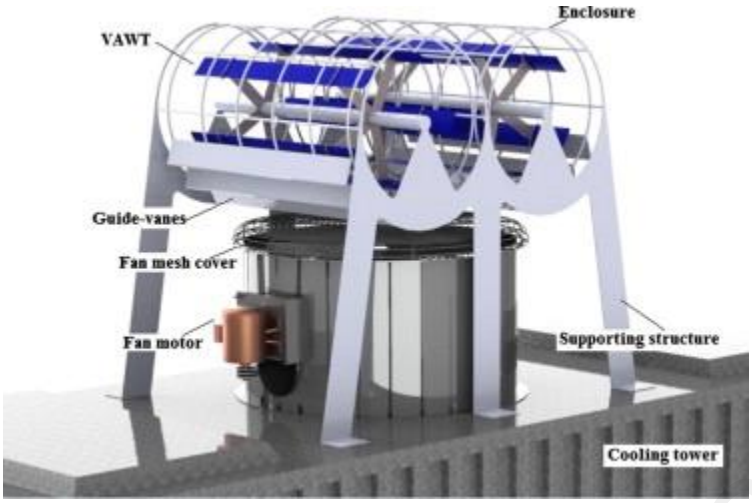

Figure 2.12: Conceptual design of the exhaust air energy recovery turbine

2.5 Discussion

In this section, it is explained that why the wide application of the available wind turbines in urban areas is limited. The conventional wind turbines technology, including horizontal axis wind turbines (HAWTs) and vertical axis wind turbines (VAWTs), has been considerably advanced in last several decades and their performance has been significantly increased. Nevertheless, the application of wind turbines is still restricted in urban areas due to their structural limitations. Based on the structural features, HAWTs and VAWTs have their own merits and drawbacks. A comprehensive review on the benefits of available wind turbines to be used in urban areas has been done and the findings are is tabulated and compared in Table 2.1.

Table 2.1: Performance estimation of HAWT and VAWT (Islam et al., 2013; Mittal et al., 2010; Walker, 2011)

	VAWT	HAWT	Requirements of Urban Wind turbine
Tower sway	*No*	*Yes*	*Tower should not be implemented on urban wind turbines to achieve good integration with urban environments.*
Yaw mechanism	*No*	*Yes*	*Yaw mechanism should not be used for urban wind turbines, because the complexity of operation will reduce the widespread.*
Self-starting	*No*	*No*	*It is important for urban wind turbine to have self-starting ability, especially in low wind speed condition.*
Blade structures	*Simple*	*Complex*	*The complex blade structure will increase the manufacture cost, which is not good for wind turbine widespread.*
Generator location	*On ground*	*Not on Ground*	*The generator should be placed on ground level or rooftop for easily maintenance.*
Height from ground	*Small*	*Large*	*The high location will make the maintenance not easily, and increase maintenance cost.*
Blade's operation space	*Small*	*Large*	*The blade's operation space should be as small as possible due to the space limitation in urban area.*
Noise produced	*Low*	*High*	*Due to implement in urban areas, the level of noise should keep low.*
Wind direction	*Independent*	*Dependent*	*The flows in urban areas are frequently changed. The wind turbines should independent on wind directions.*
Safety	*Less*	*Less*	*Due to wind turbines will be implement in The safety is an important issue to be considered*
Theoretical efficiency	*About 59%*	*About 59%*	*The theoretical efficiency shows the potential of wind turbine to do further improvement.*
Actual efficiency	*5% - 25%*	*30% - 50%*	*It is a critical issue to evaluate the performance of wind turbine. High efficiency will lead more power generated in unit area.*

To be able to widely use a wind turbine in urban areas, it should meet six requirements, including low manufacturing and maintenance cost, easy operation, good integration, and high performance and safety. The manufacturing cost is highly dependent on the complexity of tower structure and blade profiles. A design with simple blade profiles and no tower part can significantly shrink the fabrication cost. From Table 2.1, it can be concluded that the VAWTs structure require lower fabrication cost than HAWTs. By considering factors such as the need of yaw mechanism, the self-starting ability and the wind directions, it can be concluded that VAWTs are more suitable than HAWTs to be utilised in urban areas. In order to achieve a wider range of application, the maintenance should be easy and inexpensive.

Therefore, the generator required to be located on the ground for easier access. In terms of noise emission, the noise level generated by VAWTs is lower than HAWTs due to their lower tip speed ratio (λ). Thus, it can be found out that the VAWTs are more suitable than HAWTs in terms of fabrication, operation, maintenance and noise emission. Due to space limitation in urban areas, an efficient wind turbine is required to generate more power per unit area. However, the VAWTs' efficiency is considerably lower than HAWTs- about 50%- and this is one of the main drawbacks of VAWTs. The safety is also an important factor because urban wind turbines are placed in high population density areas. Thus, the wind turbine blades should be protected to reduce the risk of possible damages that can be caused by high speed rotating blades. Unfortunately, the safety factors of both types of conventional wind turbines are not acceptable enough. Therefore, it is concluded that the conventional wind turbines are not suitable for urban areas unless some modifications are done on them.

Over the last decades, extensive attentions have been drawn to wind turbine application in cities. So far, there has been a considerable development in both technologies and design concepts of urban wind turbines. These devices are classified in three groups, simply conventional, retro-fitting and specially designed wind turbines. Various wind turbines are compared in terms of integration, maintenance, safety, manufacture, performance and noise. The results of this comparison are shown in Table 2.2.

Table 2.2: Summary of wind turbine configurations

	Integration	Maintenance	Safety	Manufacture	Performance	Limitation
Micro-HAWT	Bad	High	Low	High	Good	The yaw mechanics are required to achieve best performance
Savonius HAWT	Bad	Low	Low	Low	Bad	Low power coefficient
Diffuser WT	Bad	Medium	Medium	High	Good	The system should be placed high with hub structure
Zephyr VAWT	Bad	Low	High	High	Good	Complex construction and Occupies large area
Ducted WT	Good	Low	High	Low	Good	Limited by wind directions
Crossflex WT	Good	High	Low	High	Good	The best performance achieved at 14m/s of approaching flow
Vertical Resistant WT	Good	Low	High	Low	Good	Only designed in theory

Table 2.2 clearly indicates that despite the achieved improvements, there are still existing limitations in wind turbine application. However, these finding can present some promising ideas for urban wind turbine development. The diffuser and stator vanes improvements highlight the significance of an external structure to enhance a wind turbine performance. The flow can be modified by such structures, prior to approaching turbine blades, not only to increase the flow velocities but also to control the angle of attack. Moreover, an omnidirectional flow can be guided to a unified direction to tackle the issue of frequently changing direction flow in urban areas.

One of the efficient ways to shrink the CO_2 emission and compensate the energy shortage in urban areas is to utilise wind energy. Although, numerous studies are carried to enhance the available wind turbines performance, there is a lack of suitable wind turbines to be utilised in urban areas. Thus, there is still a huge need to design a novel wind turbine with addressing all the requirements. The methods and results of

studies that have been performs previously can be considered and implemented in new urban wind turbines design.

2.6 Summary

In this chapter, available wind turbines were extensively reviewed. It has been shown that due to urban environment complexity, conventional wind turbines cannot be used in urban areas. Therefore, an innovative urban wind turbine is required to be utilised wind energy in such areas. The requirements of an appropriate urban wind turbine have been studied and laid out. In addition, available researches on various types of urban wind turbines have been presented and their pros and cons were analysed. Finally, the requirements were evaluated and applied in order to design a novel wind turbine.

CHAPTER 3: METHODOLOGY

This chapter will conduct a review on experimental apparatus and methodologies used to validate the performance of exhaust air recovery system in this research.

3.1 Experimental

3.1.1 Cooling Tower Model

A scaled model of a cooling tower was built to perform the laboratory test. The model consists of an axial fan, the main body and supportive structure. Figure 3.1 shows the exhaust fan and the enclosure body used in this study. The model is mainly constructed using fibre reinforced material (FRM) in order to keep the similarity to the actual cooling tower models. A 0.75 kW three-phase asynchronous fan motor was installed at the internal centre of the main body. The fan rotational speed can be controlled with a fan driver, which is able to run the fan at the highest rotational speed of 910 rpm.

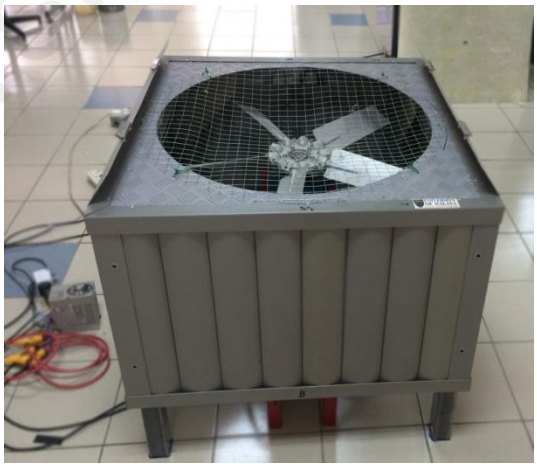

Figure 3.1: Exhaust fan model

3.1.2 Wind Turbine Installation

A commercially available 10 W H-rotor vertical axis wind turbine was installed on the top of the cooling tower model supported by an aluminium frame structure. The wind turbine consists of five FX63-137 airfoil blades with similar length and diameter

of 30 cm and chord length of 4.5 cm. Figure 3.2 shows the cooling tower, supporting frame and the wind turbine installed on top of that.

Figure 3.2: The cooling tower, supporting frame and the wind turbine

3.1.3 Measurement Instruments

Reliable and accurate measurement methods and instruments must be applied to measure several factors such as generated power, fan motor power consumption and intake flow rate as important criteria to evaluate the exhaust air recovery system performance and validate the numerical results. The overall approach is to maintain a set of reliable testing measurements by using appropriate hardware and devices. The devices used in this study will be described in following sections.

3.1.3.1 Dynamometer

The dynamometer comes with a dynamometer controller, which control the generator load by varying the duty cycle of generator's power connection to resistive dump load. It is capable of measuring both mechanical and electrical power of the wind turbine. The speed is measured by the generator AC frequency while the torque is measured by a load cell. For electrical power measurement, a 3-phase AC rectifier is provided. Voltage sensor and current sensor are available to measure the rectified DC voltage and current, which show the generator electrical power.

This system features an integrated sensors and serial communicated Data Acquisition System (DAQ). Sensors available on this system are speed measurement from AC frequency, load cell for torque measurement, 1 channel of current sensor, 1 channel of voltage sensors, 2 channels of 5V analogue measurement and one additional speed channel. All of these sensors can be read by the computer data logging software for display and recording. The dynamometer is provided with a data display and logging program called the Dyno Monitor. It communicates with the controller via a serial port and provides the access to the analogue inputs, the second speed input and other calculated values. Figure 3.3 shows a typical screenshot of the Dyno Monitor software. All data is also saved to a file in the Comma Separated Variables (CSV) format, which can be loaded into any spreadsheet for further analysis. Testing results are stored in a data file located at the selected desire location prompted each time the program is launched.

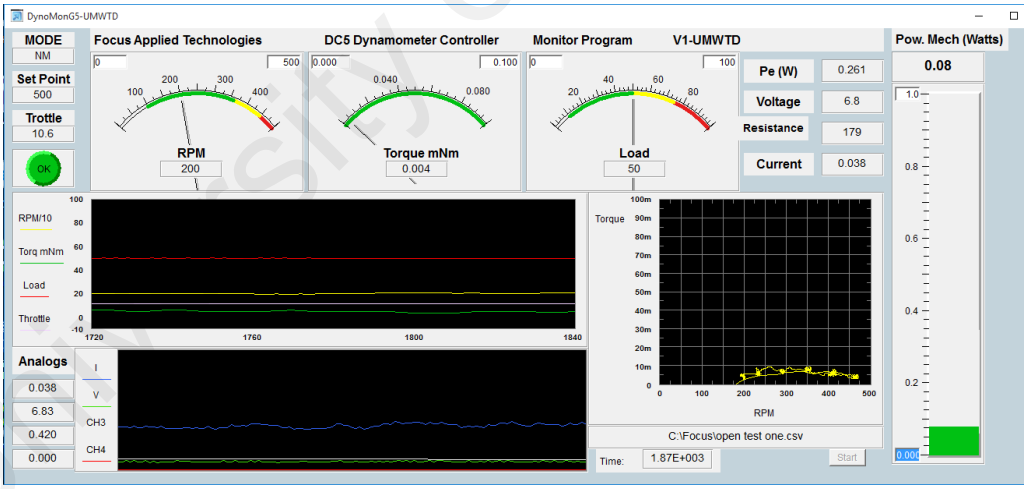

Figure 3.3: Dyno Monitor software interface

3.1.3.2 Anemometer

A commercially available anemometer (Model: AM-4247SD) is used to measure the air velocity and mass flow rate. Two probes are included in this device, Anemometer probe and Humidity/Temperature meter. Since the temperature and humidity are not considered in this study, the anemometer probe is only used to measure the air velocity.

A real-time SD memory card data logger, calendar and a real-time data recorder is built in this tool. This device is capable to measure the air velocity in range of 0.4 to 35.0 m/s with resolution of 0.1 m/s and accuracy of $\pm(2\%+0.2\,m/s)$. This anemometer is used to measure the exhaust fan intake airflow and discharge velocity.

3.1.3.3 Power Quality and Energy Analyser

In order to monitor the exhaust fan power consumption, a Fluke 435 Series II power quality and energy analyser was used. This device is able to capture the voltage and current used by the fan motor by $0.01\ \mathrm{V}$ and $0.1\ \mathrm{A}$ resolutions respectively. Therefore, the fan motor power consumption can be calculated and logged accurately during the experiments. The logged data on an internal memory can be exported as an excel file using Power Log ® software to computers via Universal Serial Bus (USB) ports.

3.2 Numerical Method

Three fundamental principles are used to govern the physical nature of fluid and heat flow. These cornerstones of the modern energy analysis are conservation of mass, conservation of momentum, and the conservation of energy. The conservation of energy is only used if the problem involves heat transfer. Therefore, in this research the conservation of energy will be neglected.

3.2.1 Commercial CFD Software

The software used to carry out the simulation in this study is the commercially available ANSYS FLUENT, version 15. The ANSYS CFD package contains several options to obtain a solution allowing the user to simulate and compare many configurations. As an example, it offers features that make parametric studies a viable option with complex models. This enables users to define several parameters in a case and investigate the effect of them on one or more outcomes in a time-effective way.

This feature is used in study to investigate the effect of various geometry optimization of the VAWT performance.

3.2.2 Governing Equations

As discussed earlier, this research will focus on two conservation equations, mass and momentum, that will model the flow's primary behaviours. In addition, various turbulence equations will be mathematically modelled to provide a way to close the conservation equations in a numerical sense. Finally, we will peer into the aspects of the mathematical discretization models used for these CFD simulations. An in-depth explanation of the governing equations involved with CFD modelling can be found in the work by Ferziger and Peric (2012). However, for the work presented here, the governing equations are as follow:

3.2.2.1 Conservation of Mass

The conservation of mass states that mass cannot be created or destroyed. Another way of stating this would be a visual representation of a control volume (*CV*). The amount of mass that enters a control volume minus the mass that leaves it at any point in time must be equal to zero. Equation 3.1 puts this into a mathematical format as follows:

$$\partial \frac{\partial}{\partial t} \int_{cv} \rho dv + \int_{cs} \rho \vec{U}.\vec{n}.dA = 0 \tag{3.1}$$

where ρ represents the fluid density, dv represents the fluid volume, $\vec{U}$ is the velocity vector, $\vec{n}$ is the outward unit vector normal to the control surface, and finally dA is the defined differential area. Since the results would be valid for all arbitrary control volumes, the sum of the integration over the two integrands must be zero everywhere for the system. The continuity equation in partial differential form can be represented as:

$$\frac{\partial}{\partial t}\rho + \frac{\partial}{\partial x_i}(\rho U_i) = 0 \tag{3.2}$$

In this equation, U_i is the component of the velocity in the x direction, x_i represent the indices indicate the summation from one to three.

3.2.2.2 Conservation of Momentum

Momentum is defined as the mass of an object multiplied by the velocity of the object. This makes momentum a vector having both a magnitude and a direction. Again, the law of conservation states that momentum cannot be created nor destroyed. Thus, the law of conservation of linear momentum states that the sum of the forces acting upon an infinitesimal CV is equal to the momentum change rate. Newton's second law as shown in Equation 3.3 is described as the sum of the forces on the CV is equal to the mass (*m*) multiplied by the acceleration of the CV ($\vec{a}$). Equation 3.4 will expand upon this principle in respect to momentum.

$$\sum \vec{F} = m\vec{a} \tag{3.3}$$

$$\rho\left[\frac{\partial}{\partial t}U_i + U_j\frac{\partial}{\partial x_i}U_i\right] = -\frac{\partial}{\partial x_i}p + \frac{\partial}{\partial x_j}\mu\frac{\partial}{\partial x_j}U_i + \rho g_i \tag{3.4}$$

Where the left side of the above equation represents ($m.\vec{a}$) and the right side of the equation represents the balancing force ($\sum \vec{F}$). The first term on the left side of the equation represents the increase in momentum per unit volume. The second term on the left side of the equation is the rate of increase in momentum due to convection per unit volume through the CV. However, the forces on the right side of the equation must balance the left side. Hence, the first term of the right side represent the pressure forces exerted upon the CV. The second term of the right side represents the viscous forces acting upon the CV. Finally, the third term of the right hand side represents the gravity forces acting upon the envisioned *CV*.

In Equation 3.4, p is the static pressure exerted upon the CV, μ is the dynamic viscosity of the fluid, and g is the gravity force acting upon the CV. However, in this study, gravity force was not considered.

3.2.3 Turbulence Models

While this research will not go into extraordinary depth on the theories behind turbulence modelling, it can be briefly summarized. Turbulent models give numerical programs a way to close the conservation of momentum equations. This can be performed through modelling the life and death of kinetic energy (k) when using two equation models as was primarily used for this research. As it will soon be seen through the explanation of the two-equation family of turbulence models, improvements have been made over time.

3.2.3.1 k-ε Model

The $k-\varepsilon$ model is classified as a two equation model in which model transport equations are solved for the two turbulence quantities (k and ε) (Hansen, 2015). Due to its robustness, this model is the most widely used today. While many developments to the $k-\varepsilon$ model have happened over time, the creation of this model is attributed to Jones and Launder (Hansen, 2015). The k equation models the turbulent kinetic energy as can be seen in Equation 3.5. In addition, the ε equation (Equation 3.6) models the kinetic energy dissipation (k).

$$\frac{\partial}{\partial t}(\rho k)+\frac{\partial}{\partial x_i}(\rho k u_i)=\frac{\partial}{\partial x_j}\left[(\mu+\frac{\mu_t}{\sigma_k})\frac{\partial}{\partial x_j}k\right]+P_k-\rho\varepsilon \tag{3.5}$$

$$\frac{\partial}{\partial t}(\rho \varepsilon)+\frac{\partial}{\partial x_i}(\rho \varepsilon u_i)=\frac{\partial}{\partial x_j}\left[(\mu+\frac{\mu_t}{\sigma_\varepsilon})\frac{\partial}{\partial x_j}\varepsilon\right]+C_{1\varepsilon}\frac{\varepsilon}{k}(P_k)-C_{2\varepsilon}\rho\frac{\varepsilon^2}{k} \tag{3.6}$$

Now that the $k-\varepsilon$ equations have been defined, the terms contained in these two equations must be defined. Equation 3.7 defines the turbulent viscosity model.

Production of k is modelled in Equation 3.8. The modulus of the mean rate-of-strain tensor (S) is modelled in Equation 3.9.

$$\mu_t = \rho C_\mu \frac{k^2}{\varepsilon} \tag{3.7}$$

$$P_k = \mu S^2 \tag{3.8}$$

$$S \equiv \sqrt{2 S_{ij} S_{ij}} \tag{3.9}$$

Once the $k-\varepsilon$ transport equations are properly defined, model constants are then selected. Even though model constants can be changed to provide improved results on different systems, the standard model constants are generally preferred. Model constants used with the standard $k-\varepsilon$ model are listed below.

- $C_{1\varepsilon} = 1.44$
- $C_{2\varepsilon} = 1.92$
- $C\mu = 0.09$
- $\sigma_k = 1.0$
- $\sigma_\varepsilon = 1.3$

It should be noted that this is the most basic form of the $k-\varepsilon$ model and improvements such as implementation of the *RNG* $k-\varepsilon$ model as well as the Realizable $k-\varepsilon$ model have been developed. Both models provide improved results within certain classes of flows.

3.2.3.2 k-ω SST Model

While the $k-\varepsilon$ model has been a reasonable model for non-complex flows, a more accurate turbulence model was needed. Hence, the development of the $k-\omega$ model was done by Wilcox et al. (Hansen, 2015). However, it was not an entirely new model. The $k-\omega$ model is a direct descendant of the $k-\varepsilon$ model. It should be noted that this model has also undergone many modifications as well. One modification that is of particular interest is the *SST* model developed by Mentor (Fluent, 2009). This model

incorporates a damped cross-diffusion term ($D\omega$) in the ω equation and has shown improved results, especially in the near-wall region (Hansen, 2015). For brevity and due to its superiority in this case of flows, the Mentor SST model will be directly shown. The Transport equations for the Mentor SST model are shown in Equations 3.10 and 3.11 below.

$$\frac{\partial}{\partial t}(\rho k)+\frac{\partial}{\partial x_i}(\rho k u_i)=\frac{\partial}{\partial x_j}\left(\Gamma_k \frac{\partial}{\partial x_i}k\right)+\tilde{P}_k-Y_k+S_k \tag{3.10}$$

$$\frac{\partial}{\partial t}(\rho \omega)+\frac{\partial}{\partial x_i}(\rho \omega u_i)=\frac{\partial}{\partial x_j}\left(\Gamma \omega \frac{\partial}{\partial x_i}\omega\right)+P_\omega-Y_\omega+D_\omega+S_\omega \tag{3.11}$$

The terms within the Mentor SST transport equations will now be defined. The diffusivity for the transport equations are modelled in Equations 3.12 and 3.13 where σk and $\sigma\omega$ are the turbulent Prandtl numbers for k and ω. Next, the turbulent viscosity is modelled in Equation 3.14 where S are the strain rate magnitudes σ_k and σ_ω which are defined in Equations 3.15 and 3.16.

$$\Gamma_k=\mu+\frac{\mu_t}{\sigma_k} \tag{3.12}$$

$$\Gamma_\omega=\mu+\frac{\mu_t}{\sigma\omega} \tag{3.13}$$

$$\mu_t=\frac{\rho k}{\omega}\frac{1}{\max\left[\frac{1}{\alpha^*},\frac{SF_2}{\alpha_1\omega}\right]} \tag{3.14}$$

$$\sigma_k=\frac{1}{\frac{F_1}{\sigma_{k,1}}+\frac{(1-F_1)}{\sigma_{k.2}}} \tag{3.15}$$

$$\sigma_\omega=\frac{1}{\frac{F_1}{\sigma_{\omega,1}}+\frac{(1-F_1)}{\sigma_{\omega.2}}} \tag{3.16}$$

The coefficient α^* damps the turbulent viscosity causing a low Reynolds number equation and is given in Equation 3.17. The terms in Equation 3.17 are defined by Equations 3.18, 3.19, 3.20 and 3.21.

$$\alpha^* = \alpha_\infty^* \left(\frac{\alpha_0^* + \frac{\mathrm{Re}_t}{R_k}}{1 + \frac{\mathrm{Re}_t}{R_k}} \right) \tag{3.17}$$

$$\frac{\rho k}{\mu \omega} \tag{3.18}$$

$$R_k = 6 \tag{3.19}$$

$$\alpha_0^* = \frac{\beta_i}{3} \tag{3.20}$$

$$\beta_i = 0.072 \tag{3.21}$$

The Blending functions, $F1$ and $F2$ are defined by Equations 3.22 to 3.26, where y is the distance to the next surface and is the positive portion of the cross-diffusion term, D_ω^+ as defined in Equation 3.25.

$$F_1 = \tan^{-1} \Phi_1^4 \tag{3.22}$$

$$\Phi_1 = \min\left[\max\left(\frac{\sqrt{k}}{0.09\omega y}, \frac{500\mu}{\rho y^2 \omega} \right), \frac{4\rho k}{\sigma_{\omega,2} D_\omega^+ y^2} \right] \tag{3.23}$$

$$D_\omega^+ = \max\left[2\rho \frac{1}{\sigma_{\omega,2}} \frac{1}{\omega} \frac{\partial k}{\partial x_j} \frac{\partial \omega}{\partial x_j}, 10^{-10} \right] \tag{3.24}$$

$$D_\omega = 2\left(1 - F_1\right) \rho \sigma_{\omega,2} \frac{1}{\omega} \frac{\partial k}{\partial x_j} \frac{\partial \omega}{\partial x_j} \tag{3.25}$$

$$F_2 = \tan^{-1} \Phi_2^2 \tag{3.26}$$

$$\Phi_2 = \max\left[2\frac{\sqrt{k}}{0.09\omega y}, \frac{500\mu}{\rho y^2 \omega}\right] \tag{3.27}$$

Now that the diffusion terms have been explained, the turbulence production terms can now be defined. The production of kinetic energy $\tilde{P}_k$ is modelled in Equation 3.29. The standard production of kinetic energy P_k is modelled in the same manner as it was in the $k-\varepsilon$ model as it can be seen in Equation 3.29.

$$\tilde{P}_k = \min(G_k, 10\rho\beta^* k\omega) \tag{3.28}$$

The production of ω (P_ω) is modelled in Equation 3.30 where the coefficient α is given by Equation 3.31. α^* was given by Equation 3.17. α_∞ can be seen in Equation 3.32 where $\alpha_{\infty,1}$ and The term $\alpha_{\infty,2}$ is defined by Equations 3.33 and 3.34. Finally, the Von Karmon Constant (k) is shown in Equation 3.35.

$$P_\omega = \frac{\alpha}{\nu_t} P_k \tag{3.29}$$

$$\alpha = \frac{\alpha_\infty}{\alpha^*}\left(\frac{\alpha_0^* + \frac{\mathrm{Re}_t}{R_\omega}}{1+\frac{\mathrm{Re}_t}{R_\omega}}\right) \tag{3.30}$$

$$\alpha_\infty = F_1\alpha_{\infty,1} + (1-F_1)\alpha_{\infty,2} \tag{3.31}$$

$$\alpha_{\infty,1} = \frac{\beta_{i,1}}{\beta_\infty^*} - \frac{k^2}{\sigma_{\omega,1}\sqrt{\beta_\infty^*}} \tag{3.32}$$

$$\alpha_{\infty,2} = \frac{\beta_{i,2}}{\beta_\infty^*} - \frac{k^2}{\sigma_{\omega,2}\sqrt{\beta_\infty^*}} \tag{3.33}$$

$$k = 0.41 \tag{3.34}$$

Next, the dissipation of k (Y_k) and the dissipation of ω (Y_ω) are defined in Equations 3.36 and 3.37 where β_i is given by Equation 3.38.

$$Y_k = \rho\beta^* k\omega \tag{3.35}$$

$$Y_\omega = \rho\beta^* \omega^2 \tag{3.36}$$

$$\beta_i = F_1\beta_{i,1} + (1-F_1)\beta_{i,2} \tag{3.37}$$

The Mentor SST model can now be finished up with its standard constants as follows:

$\sigma_{k,1}$=1.176, $\sigma_{k,2}$=1.0, $\sigma_{\omega,1}$=2.0, $\sigma_{\omega,2}$=1.168, α_1=0.31,

$\beta_{i,1}$=0.075, $\beta_{i,2}$=0.0828, α_∞=0.52, α_∞^*=1, $\alpha_0 = \frac{1}{9}$,

$\beta_\infty^* = 0.09,\ \mathrm{R}_\beta = 8,\ \mathrm{R}_k = 6,\ \mathrm{R}_\omega = 2.95,\ \xi^* = 1.5,$ and $\mathrm{M}_{t0} = 0.25$

3.2.4 Discretization

3.2.4.1 Control Volume Discretization

CFD solvers do not have the ability to solve equations directly in the general form. Thus, there is the need for discretization. The three dominant discretization techniques that are currently in use are the Finite Element (FE) method, the Finite Difference (FD) method and the Finite Volume (FV) method. FLUENT performs discretization via the FV method. This gives FLUENT the ability to transform the conservation equations into algebraic forms to solicit a numerical and iterative solution. The integral form of the FV general transport equation for the scalar quantity ϕ is shown below in Equation 3.39. The term *dA* represents the CV element area; *dV* is the element CV, Γ is the diffusivity of the quantity ϕ, S_ϕ is the source or sink of ϕ, finally, the value ϕ represents the intensive property of the fluid evaporated per unit mass.

$$\underbrace{\frac{\partial}{\partial t}\int_{cv}\rho\phi dV}_{Unsteady} + \underbrace{\int_{A}\vec{n}.(\rho\phi\vec{u})dA}_{Convection} = \underbrace{\int_{cv}\vec{n}.(\Gamma\nabla\phi)\,\mathrm{dA}}_{Diffusion} + \underbrace{\int_{cv}S_\phi dV}_{Source/\mathrm{sink}} \tag{3.38}$$

Equation 3.39 is then discretized to Equation 3.40, which can then be solved for each cell defined by the mesh that is generated for the solver. This generated equation set is then solved iteratively to produce a solution set for the flow.

$$\frac{(\rho\phi)^{t+\Delta t}-(\rho\phi)^{t}}{\Delta t}\Delta V+\sum_{faces}\rho_f\phi_f V_f A_f=\sum_{faces}\Gamma_f(\nabla\phi)_{\perp,f}A_f+S_\phi\Delta V \tag{3.39}$$

3.2.4.2 Cell Face Value Discretization

Now that a set of discretized transport equations have been developed for each cell, those equations need discretized information from the cell faces for the convection and diffusion terms. Solvers fall into two primary categories, robust methods that lack accuracy, and more accurate methods that require additional computational time. The second order upwind method has been chosen for this research due to its accuracy combined with its speed compared to higher order methods. Equation 3.41 shows the equation used to compute the face value of each cell face and the gradient of each cell, ϕ, is modelled via Equation 3.42 through the use of the divergence theorem where the face values, $\tilde{\phi}_f$, are calculated by averaging φ from the cells adjacent to the face.

$$\phi_f=\phi+\nabla\phi\cdot\Delta\vec{S} \tag{3.40}$$

$$\nabla\phi=\frac{1}{V}\sum_{faces}^{N}\tilde{\phi}_f\vec{A} \tag{3.41}$$

3.2.4.3 Cell Face Pressure Discretization

The final discretization to be discussed is the pressure discretization scheme. Either a pressure based solver or a density-based solver can be used in FLUENT. Due to the high pressure gradients caused by the moving mesh interface, the Pressure Staggering Option (PRESTO) pressure discretization scheme was chosen (Fluent, 2009).

3.2.5 Pressure-Velocity Coupling

Pressure-Velocity coupling refers to the way mass continuity is accounted when using the segregated solver. FLUENT offers three ways to handle this: SIMPLE, SIMPLEC, and the PISO method. Because the flow is incompressible, the coupling between the velocity and the pressure field can be considered strong. Thus, the SIMPLE method was chosen due to its robustness. The SIMPLEC method can be considered insufficient due to the high turbulent nature of the flow (Fluent, 2009). The PISO method would have also been a good choice, especially in the case of unsteady flows. The PISO method is also well suited for meshes with higher than average skew (Fluent, 2009).

3.2.6 Under Relaxation

The relaxation factor can be thought of as a measure of how fast the solvers steps toward the final solution. If the solver steps too fast, the solution may diverge. However, the lower the relaxation factor is set, the slower the solution converges. Thus, the relaxation factor can be considered as a tool to help attain a converged solution, especially when moving boundaries are introduced (Fluent, 2009). Equation 3.42 shows how FLUENT calculates the φ value at the cell centre with the relaxation factor (α):

$$\phi_{new} = \phi_{old} + \alpha(\phi_{calculated} - \phi_{old}) \tag{3.42}$$

3.2.7 Numerical Method Summary

The foundation from which CFD solvers operate is the conservation laws as can be seen in Equations 3.1 and 3.4. However, that is only the beginning of the process of modeling a system. It can be seen that computers need a way to close the conservation equations for turbulent flows. This is performed by various turbulence models. From studying the turbulent equation models in this section, it can be seen how the two-

equation turbulence models have evolved over time. The relatively simple $k-\varepsilon$ equations have evolved into the more complex Mentor SST $k-\omega$ equations. However, it should be noted that there are many other turbulent models can be used. Finally, discretization is used to coax the equations into a form that computational systems can solve algebraically which provides a system solution through pressure-velocity coupling and under-relaxation procedures.

3.3 Optimization

In design optimization, an optimization model is composed principally of three elements: design variables or parameters, an objective function, and constraints. Fundamentally, the optimal design problem is mathematically formulated as below:

For single objective optimization, we optimize $y(X)$ subjected to:

$$h(x) = 0$$

$$g(x) \leq 0$$

$$X' \leq X \leq X''$$

For a multi-objective optimization, a problem is cast as,

Optimize $Y(X)$

Where $y(X)$ is an objective function and $Y(X)$ is a collection of objective functions and is defined as $Y = (y_1, y_2, y_3, ..., y_k)^T$ *and* $X = (x_1, x_2, x_3, ..., x_k)$.

In design and product engineering, the process of design optimization begins by defining input factors, which have influence on the system of interest. In design optimization, the input factors are defined in terms of design variables *(X).* For specific design variables, the system outputs are generated via a design process. Based on the relation between design variables and the system outputs, an objective function, *y(X),* can be constructed and either maximized or minimized (optimized). Concurrently, both equality and inequality constraint functions *h(X)* and *g(X),* respectively, and the

bounding upper and lower limits of design variables, X' and X'', can be specified and imposed on the optimal solution.

3.3.1 Design of Experiment

The theory of Design of Experiment (DOE) involves data exploration and construction of a solution in a design space in order to plan the experiments (called the Classic Design of Experiment, CDOE) and simulations (called Modern Design of Experiment, MDOE). The data distribution corresponds to a systematic set of experiments and computations, which aim at minimizing random consideration in design and thus reducing the number of experiments and simulations. The ultimate goal of DOE in the design optimization process is to maximize the information under a finite set of design parameters and 'run' numbers, while maintaining accuracy via reduction of bias error generated during the process of surrogate-model construction. Various experimental designs have been reviewed by Simpson et al. (1997) and Queipo et al. (2005). Experimental designs for computer simulations have been reported by Simpson et al. (2001) and Chen et al. (2006). These methods are briefly discussed in the following section.

3.3.1.1 Two-level Design

Three types of two-level design methods addressed here are full factorial design, fractional factorial design, and Plackett-Burman Design.

3.3.1.1.1 Full Factorial Design

Full Factorial Design (FFD) is the basic experimental design. Two-level FFD is the most common experimental design by which each design factor is assigned two levels, +1 and -1 which are called low and high levels. The number of experiments is $2k$ where k is the number of design factors. Consequently, the size of a full factorial experiment is directly proportional to the factor number. For example, five input factors each with two

levels require 2^5 (32) runs while 2^{11} (2,048) runs are required for eleven input parameters. Therefore, in practice for *k* greater than five, FFD is considered inefficient. Consider a full factorial experiment of three design factors (*k* =3). The number of full factorial experiments is eight (2^3) which are graphically depicted in Figure 3.4 (a). The number inside the circles is from 1 to 8, which indicates the standard order of experiments while the coordinates define the full factorial level.

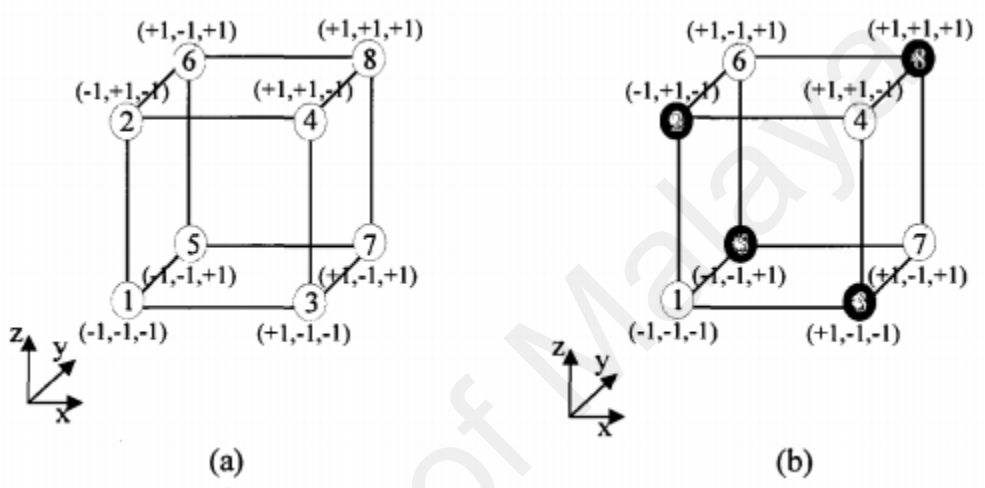

Figure 3.4: Graphical interpretations of (a) full-factorial-based experiment and (b) fractional-factorial-based experiment

3.3.1.1.2 Fractional Factorial Design

In fractional factorial design, the fractional factorial experiment is a fraction of full factorial experiment. The fraction equals to 2^{-q} , where *q* is a positive integer. Therefore, the number of runs for a fractional factorial experiment is equal to 2^{k-q}. Likewise, considering a full factorial experiment of three design factors when *q* is equal to 1, the number of runs for fractional factorial experiment is equal to 4 (2^{3-1}). Thus, this fractional factorial experiment would require one-half the number of runs of a full factorial experiment (2^3). The experimental design is demonstrated by bold-bordered spheres in Figure 3.4 (b).

3.3.1.1.3 Plackett-Burman Design

Both full and fractional factorial designs are sometimes used for identifying significant effects or factors, referred to as Screening Design (SD). Plackett and Burmann (1946) proposed economical designs with a run number and factorization of four. With the run number "n", up to n-1 factors can be investigated. In the case where the main effect is of interest, the Plackett-Burman Design (PBD) is considered an efficient screening design approach.

3.3.1.2 Three-level Design

To assess the influence of curvature (quadratic) effects in design, three-level design of each factor is required. The number of experiments is 3^k for full design and 3^{k-p} for fractional design. As demonstrated in two-level factorial design, the number of experiments quickly becomes larger as the design factors increase. For five input factors, a three-level design requires 243 runs (3^5).

Box-Wilson central composite design: Box-Wilson central composite design (Box and Wilson, 1951) is commonly called Central Composite Design (CCD). CCD is the modification of the full or fractional factorial design by using a central point and an extra group of points (indicated by stars) as shown in Figure 3.5.

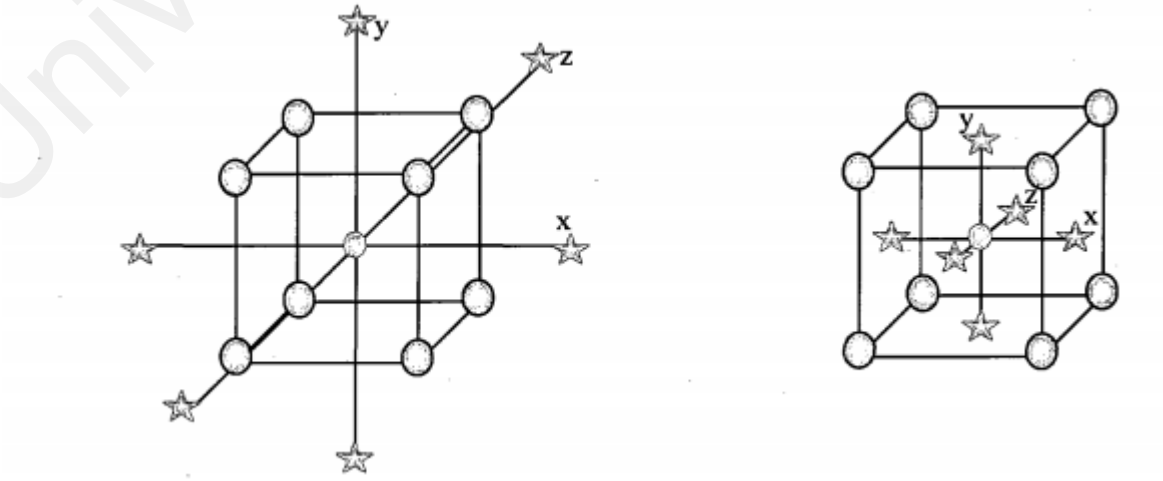

Figure 3.5: Three-dimensional graphical interpretation of extra points in CCD

There are three different patterns of designs, shown in Figure 3.6 (a)-(c). The distances from the centre of design space to the star positions are $\pm\alpha$. The Central Composite Inscribed (CCI) design is scaled of the CCC design by normalizing with α value.

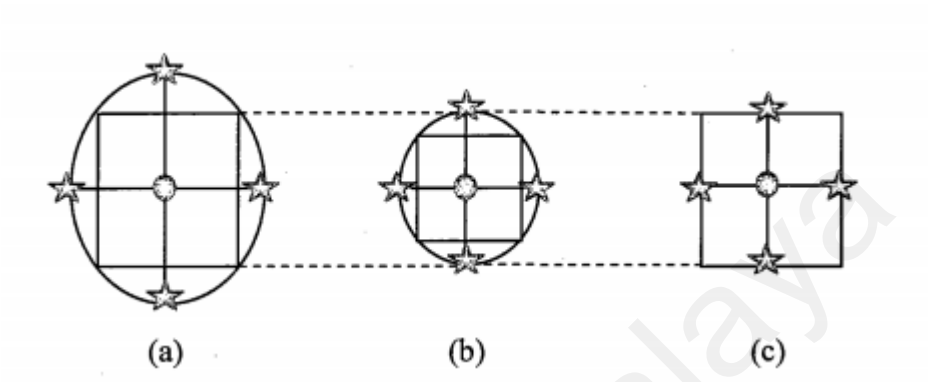

Figure 3.6: Two-dimensional graphical interpretations of the CCD designs (a) CCC design (Circumscribed), (b) CCI design (Inscribed), and (c) CCF design (Face Centred)

Box-Behnken design: Box and Behnken (1960) produced Box-Behnken Design (BBD). Unlike CCD, BBD neither incorporate full nor fractional factorial design. Instead, the design space of BBD is constructed by the middle point of the edge and the centre point, indicated by the sphere positions in Figure 3.7.

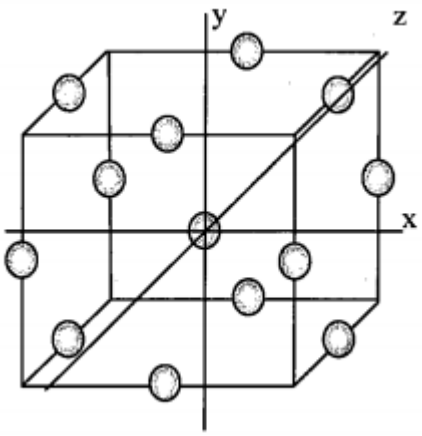

Figure 3.7: Three-dimensional graphical interpretation of treatment positions in BBD

3.3.1.3 Space Filling

The previous sections focused on so-called Classic Design of Experiment (CDOE), usually applied to sample design factors in a physical experiment. As different types of error occur in physical and computational experiments, filling design points in a design space for computational simulation is needed, while placing them at the design space boundary is irrelevant (Sacks et al., 1989). Sampling points inside a design space impacts the accuracy of an approximated model (Myers and Montgomery, 1995).

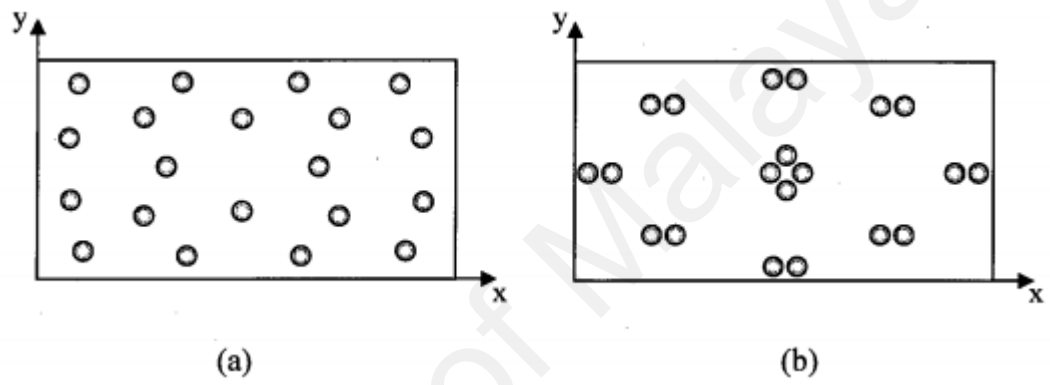

Figure 3.8: Three-dimensional graphical interpretations of (a) Space Filling design and (b) Classic design (Booker, 1998)

The classical and space filling design methods are graphically illustrated in Figure 3.8 (a) and (b), respectively. The Space Filling (SF) design method contains points distributed throughout the design space; the classic design method tends to be clustered. Two types of Space Filling design methods addressed here are orthogonal array and uniform design.

Orthogonal design: One of the SF design methods in modern experimental design that has received attention is Orthogonal Array (OA). OA was first developed by Rao (1947) and the OA definition was later given by Hedayat et al. (1999). It was stated that the array *A* with the dimension of $N \times M$ is an orthogonal array with *s* levels, strength *t*, and index λ (for some *t* in the range of $0 \le t \le k$) if every $N \times M$ subarray of *A* contains each t-tuple based on *S* exactly the index λ times a row, expressed by $N = \lambda s^t$. An orthogonal array is denoted by the notation *OA (N, k, s, t)*, where *N*, *M*, *s*, and *t* are

referred as the OA parameters. For each notation, *N* represents the number of samples, *M* is the dimension of a design space, and *s* and *t* are the level and the strength of an array, respectively. One of the drawbacks of OA is that its parameters cannot be arbitrarily selected. The desirable values of *N*, *k*, *s*, and *t* cannot be specified, thus, the replication of points can occur (Queipo et al., 2005). The OA (4, 3, 2, 2) with $\lambda = 1$ is shown in the Figure 3.9.

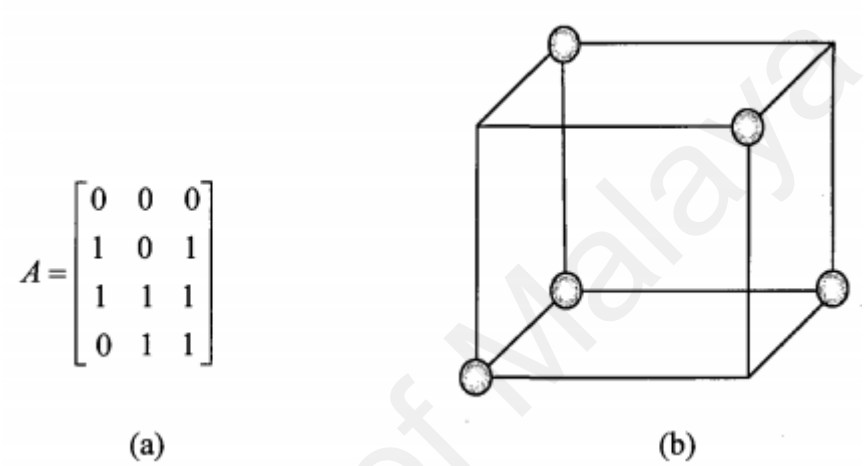

Figure 3.9: The example of OA (8, 3, 2, 2) with $\lambda = 2$ (a) matrix representation and (b) graphical representation

Uniform design: The Uniform Design (UD) was proposed by Professor Fang Kai-Tai and Professor Wang Yuan in 1980. UD is considered an efficient fractional factorial design. Several variations of uniform designs are available at Fang's homepage. The theoretical background was also originally given by Fang et al. (2000). An example of UD (3 factors, 3 levels, and 9 runs) is demonstrated by the following matrix.

$$A = \begin{bmatrix} 1 & 3 & 1 \\ 3 & 1 & 3 \\ 1 & 1 & 2 \\ 3 & 2 & 1 \\ 1 & 2 & 3 \\ 2 & 1 & 1 \\ 2 & 3 & 3 \\ 3 & 3 & 2 \\ 2 & 2 & 2 \end{bmatrix}$$

3.3.2 Response Surface Method

Response surface methodology (RSM) was developed by Box and collaborators in the 50s (Araujo and Brereton, 1996) and (Câmara et al., 2013). This term was originated from the graphical perspective generated after fitness of the mathematical model. RSM is a collection of mathematical and statistical techniques for optimization purposes. Originally, RSM was developed to model experimental responses and then migrated into the modelling of numerical experiments. The difference is in the type of error generated by the responses. In physical experiments, inaccuracy can be due to measurement errors while in computer experiments, numerical noise is a result of incomplete convergence of iterative processes, round-off errors or the discrete representation of continuous physical phenomena.

RSM is used to build a response model by calculation of data-points in conjunction with experimental design theory. The relationship can be written in a general form as follows (Myers et al., 1995):

$$y = F(x_1, x_2, ..., x_{nv}) + \varepsilon \tag{3.43}$$

Where, y is response variable, x_i are design variables, and ε represents the total error which is often assumed to have a normal distribution with zero mean. The response surface model, *F*, is usually assumed as a second-order polynomial that can be written for n_v design variables as follows:

$$\hat{y} = c_0 + \sum_i c_i x_i + \sum_{1 \le i \le j \le n_v} c_{ij} x_i x_j, \; p = 1, ..., n_s \tag{3.44}$$

Where, $\hat{y}$ is dependent variable of the response surface model, c_0, c_i, c_{ij} are regression coefficients, and n_s is the observations number. The above normal equations are expressed in a matrix form, and the least-squares method is typically used to estimate the regression coefficients.

$$\vec{y} = X\vec{c}$$
$$\vec{c} = (X^T X)^{-1} X^T \vec{y} \tag{3.45}$$

Where, $\vec{y}$ is response vector, X is a $n_s \times n_{rc}$ matrix, n_{rc} is number of regression coefficients, and $\vec{c}$ is regression coefficients vector.

The data-points are selected using three-level factorial design conducted under D-optimal condition. The D-optimal criterion states that the data-points that maximize the determinant of $\left|X^T X\right|$ are chosen. The set of data-points that maximizes $\left|X^T X\right|$ is the set of data-points that minimizes the variance of regression coefficients.

3.3.3 Central Composite Design

The central composite design was presented by Box and Wilson (Araujo and Brereton, 1996). This design is the most commonly used response surface designed experiment. Central composite designs are a factorial or fractional factorial design with centre points, augmented with a group of axial points (also called star points) that let you estimate curvature. Central composite design is able to estimate both first- and second-order terms efficiently. Central composite designs are especially useful in sequential experiments because you can often build on previous factorial experiments by adding axial and centre points.

In this Study, the experimental design, generated by the Design Expert 8 software, was a face centred Central Composite Design (CCD) with 3 levels (+1, 0, −1) for 3 numeric factors, including the vertical and horizontal rotor positions and the diffusers modification angle, and one catagoric variable, introducing of separator plates to the design. The central point was replicated six times for 20 trials. ANalysis Of VAriance (ANOVA) was used to evaluate each factor contribution to the model and the potential interaction between them. The model was assessed by RSM in order to identify the exhaust air recovery system optimal design to obtain the highest power. The data was fitted with a regression model, which is described by a quadratic polynomial equation. It

was possible to calculate the coordinates of the maximum point through the first the mathematical function derivate, which described the response surface and equates it to zero (Bezerra, Santelli et al., 2008). The wind turbine generator performance was expressed by power coefficient factor, which indicates the ratio of actual electric power produced by a wind turbine divided by the total wind power flowing into the turbine blades at specific wind speed.

CHAPTER 4: COMPUTATIONAL FLUID DYNAMIC STUDY

Prior to beginning the computational study, few experimental tests are needed to be done. In this chapter, firstly the bare cooling tower will be investigated to study the effect of installing the exhaust air recovery generator on top of that. Then, experimentation will be carried out to provide data for CFD validation. Lastly, the CFD results will be presented and discussed.

4.1 Characteristics of the Bare Exhaust Fan

In order to investigate the effect of installing the wind energy recovery system on the top of the cooling tower, it is required to measure some characteristics of the bare cooling tower. These data will also be used to validate CFD results. There are three main factors, which should be considered in this section; the fan discharge velocity pattern, the fan intake airflow rate and the fan motor power consumption.

4.1.1 The Fan Discharge Velocity

The wind speed will vary from point to point over the cross section of the exhaust air outlet duct (Daly, 1978). A suitable method for circular ducts is to divide the area into several concentric parts of equal area and the wind speed at the outlet, V_{outlet} is calculated by averaging the velocities taken at every quarter the circle (Herrman, 1962). In order to determine the points for the measurement, the area of discharge outlet is divided into five equal concentric areas and the radius to the centre of each area is determined. Each of these concentric areas is named as band where the bands are numbered as shown in Figure 4.1.

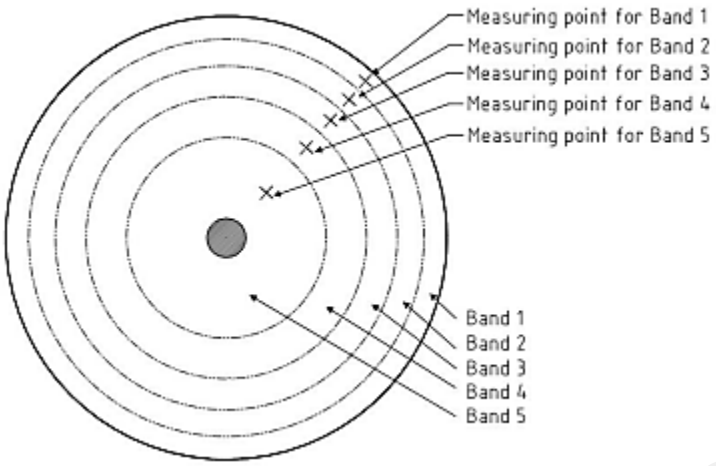

Figure 4.1: Air outlet velocity measurement point on a circular duct (Fazlizan et al., 2015)

For this cooling tower model, the discharge outlet diameter is 730 mm and the round flat plate at the centre of the outlet is 65 mm diameter. Hence, the total outlet area is 0.42 m^2 and the concentric area of each band is 0.083 m^2.

The wind speed is measured by using an anemometer for outdoor testing which is described in previous sections. The discharge airflow rate is calculated by multiplied the average wind velocity from 20 points with the discharge outlet area. The averaged velocities at these points are tabulated in Table when the fan rpm was set to 910.

Table 4.1: Averaged velocities at each measuring points

Band (distance to centre)	346	305	257	197	140	82	0	-82	-140	-197	-257	-305	-346
Wind speed (m/s)	6.92	7.75	8.27	6.47	3.97	1.22	0	1.22	3.97	6.47	8.27	7.75	6.92

Figure 4.2 shows the fan discharge velocity pattern. Highest wind speed was observed between band 3 and band 4. Band 1, where its location is near to the centre of the outlet opening shows the lowest wind speed due to the position of the belting system being located above the cooling tower outlet which resulted in airflow resistance. Wind

speed at band 5 (close to the outer radius) was low as well because there was a clearance between the blade tip and the inner wall duct (causing blade tip loss) when the exhaust air swirled and spread out from the fan. From this figure, it can be concluded that in this design the VAWT rotor position plays a vital role in the system performance.

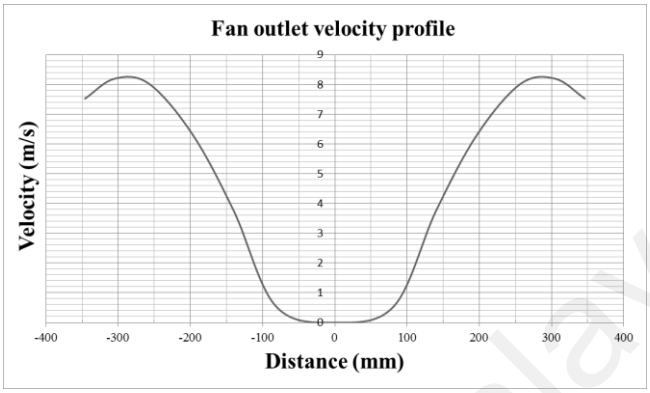

Figure 4.2: Fan discharge velocity pattern

4.1.2 Intake Airflow Rate

The average airflow rate is significant to know in order to ensure that the VAWT does not cause any blockage effect on the cooling tower system. A simple method was used to measure the intake airflow rate. Four bottom sides of the cooling tower model were divided to three equal areas as shown in Figure 4.3. The air velocity of each area was monitored by the anemometer and then averaged during each experiment.

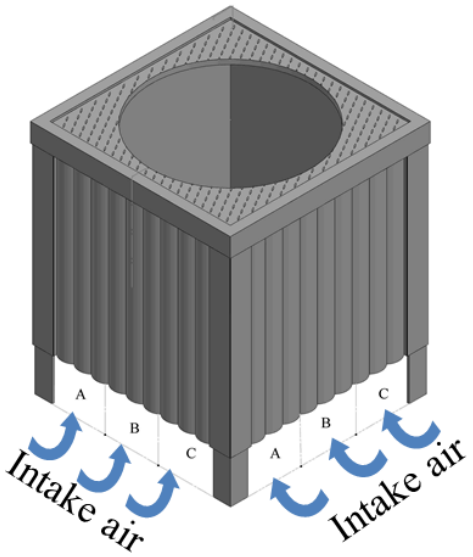

Figure 4.3: Intake air areas

Knowing the intake area, the mass flow rate can be calculated by following equation:

$$\text{Intake air flow rate } (m^3/s) = \text{Area of inlet } (m^2) \times \text{ Air velocity } (m/s) \quad (4.1)$$

The measured velocity of each point is tabulated in Table 4.2. It is also shown that the average intake velocity is 6.10 m/s. By knowing the intake area equal to 0.146 m^2, the intake flow rate is 3.5624 m^3/s.

Table 4.2: Measured intake velocities

Side 1		
A (m/s)	**B (m/s)**	**C (m/s)**
6.1	7.3	6.1
Side 2		
6.0	6.2	6.1
Side 3		
5.8	6.2	6.0
Side 4		
5.1	6.6	5.8
Average	6.1 (m/s)	

4.1.3 Fan Power Consumption

The fan power consumption of the bare cooling tower was measured using the power analyser introduced in section 3.2.3.4. The fan consumption was to be equal to 672.78 W when the rpm was set to 910. This value is used as the baseline data to be compared with the optimized designs.

4.2 Experimental Test

In order to validate the simulation results, they should be compared with experimental data obtained in the laboratory. A single five-blade rotor is installed on the top of an exhaust fan with blade diameter of *730 mm*. All the blades are airfoil FX 63-137 with chord length of 45 mm. In this validation case, the horizontal and vertical distance between the VAWT central point and the fan centre is considered as *X= 250 mm* and *Y= 300 mm*, respectively. The fan was set at the 910 rpm, which resulted in a velocity profile shown in Figure 4.2. This profile was then inserted to the velocity inlet boundary condition by using user-defined functions (UDF).

The methodology of measuring experimental outcomes is described in Chapter 3. The results obtained from the experimental test are tabulated in Table 4.3. These results will be used to validate the computational outcomes.

Table 4.3: Experimental results

Wind turbine position		**Airflow** (m^3/s)	**Fan power consumption** (W)	**Wind turbine power coefficient**
X *(mm)*	**Y *(mm)***			
250	300	3.866	668.8	0.13914

4.3 Computational Parametric Study

The unsteady nature of VAWT has made the CFD analysis of them intensive and expensive. In order to minimize this computational cost, a precisely planned approached is required. By choosing right parameters, such as turbulence model, mesh density and the time step, not only a huge amount of time can be saved but also a greater degree of accuracy can be achieved.

Almohammadi et al. (2012; 2013) have broadly analysed the impact of mesh density in VAWT power output. In their two dimensional study, SST transitional, and $RNG-K-\varepsilon$ turbulence model are tested, and it is concluded that the SST transitional is the better one. Some parametric studies were also done by Qin et al. (2011). They have used $RNG-K-\varepsilon$ similar to one of their earlier works (Howell et al., 2010). Although their work was in three dimensions, they had carried out the parametric studies in two dimensions and they claimed to achieve the mesh independency. While $RNG-K-\varepsilon$ is well-known to predict the vortices formation, and flow separation quite accurate, some researchers advocate the $SST-k-\omega$. In addition to these two models one equation model Spalart–Allmaras is also tested in this study due to the fact that it is a single equation model and computationally less expensive.

The authors have conducted the parametric study in two dimensions. The parametric study has been carried out at Tip Speed Ratio (λ) of 1.2.

4.3.1 Computational Domain and Grid Generation

The geometrical specifications of the computational domain used in validation phase are shown in Figure 4.4. The width and length of the domain are considered to be 12 and 16 times of the rotor diameter respectively to avoid any possible blockage ratio. Velocity inlet boundary condition coupled by an UDF code is assigned to the inlet while the pressure outlet with Turbulence intensity of 5% is considered for the outlet.

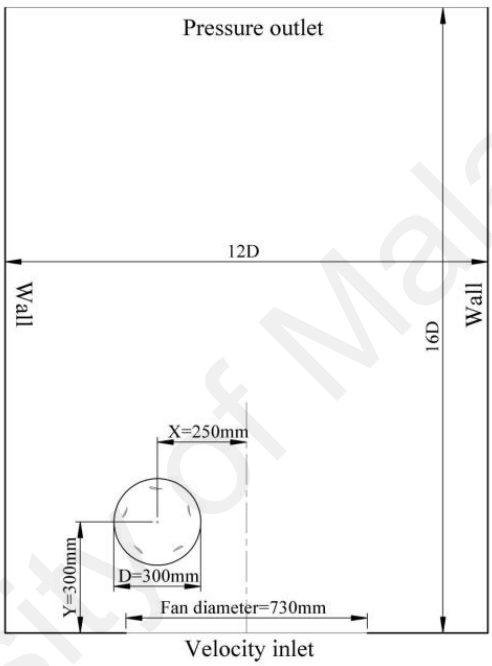

Figure 4.4: Computational domain

For mesh generation, the computational domain was divided into two sub-domains including one rotating and a fixed rectangular-shaped one with a circular aperture. The rotational domain is placed as close as possible to the actual rotor diameter in order to achieve results that are more accurate. As Figure 4.5 shows, the rotating domain is divided into several sub-sections in order to produce a higher quality mesh. The airfoils were also enclosed by ellipses to control the meshing more efficiently.

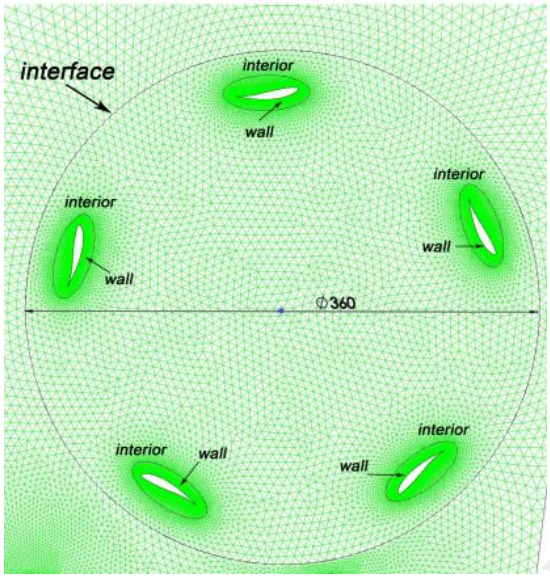

Figure 4.5: Boundary around VAWT

Due to the revolution of the turbine, the moving mesh approach was used for the VAWT. The rotating and fixed domains are separated by interfaces, which are shown by Figure 4.5. The same sized mesh was selected for both sides of the interface. According to the fluent guidebook (Fluent, 2012), the same characteristics in interface cell sizes can obtain a faster convergence. Unstructured mesh was chosen for all the domains. The generation of mesh started from the airfoils; in the grid independency test, various mesh sizes from *0.05* to *0.2 mm* was applied on the airfoils. The mesh was then coarsened as it goes further to the outer domain. In order to capture the flow behaviour precisely around the blade, ten boundary layers of the structural mesh are generated. In this way, the Y_{plus} is also guaranteed to stay as low as 1.

To study the effect of mesh dependency, three different meshes were produced. The meshing is done following particular size functions. The refinement is only done on the blades. Since an enclosure is put around the blade, the refining is limited to the blade surface, and the enclosure. The stationary domain and the other portion of rotating domain remain unchanged. The mesh description is given in Table 4.4. Mesh dependency study is shown in section 4.3.3.

Table 4.4: Different mesh description

Mesh description	**M3**	**M2**	**M1**
Number of cells	260,531	850,054	901,560
Number of nodes on a blade	350	700	900

4.3.2 Turbulence Testing

In this study, $RNG-K-\varepsilon$, Spalart–Allmaras (S–A) and $SST-k-\omega$ turbulence models were investigated. Except S–A, the other two turbulence models use turbulence kinetic energy k and dissipation rate. For, k the value was decided using the following equation:

$$k = \frac{3}{2} \times (UI)^2 \tag{4.2}$$

Here, U and I refer to average velocity, which is 5.28 m/s (inflow) and turbulence intensity respectively. The turbulence intensity was assumed 5%. The value of turbulence kinetic energy is 0.1045 (m^2/s^2). The value of ω is obtained using the following equation:

$$\omega = k^{\frac{1}{2}} \Big/ LC_{\mu}^{\frac{1}{4}} \tag{4.3}$$

Here, L is the turbulent length scale and C_{μ} is constant. The turbulent length scale is assumed 0.01. The turbulence intensity represents incoming vortices, and turbulent length scale is a dimensionless quantity, which depicts the smallest possible diameter of the vortices.

Yahkot et al. (1992) used renormalization to derive $RNG-K-\varepsilon$ model from typical $K-\varepsilon$ model. The main intention is to accurately model the Reynolds stress, and predict the production of dissipation terms. The number of equations has increased, which leads to higher computational time. The value of ε is derived using the following equation:

$$\in = C_{\mu}^{\frac{1}{4}} k^{\frac{3}{2}} \Big/ L \tag{4.4}$$

The Spalart–Allmaras model is a one-equation model, which has been designed with the objective of numerical efficiency. As it is a one-equation model, it is much faster than the $RNG-k-\varepsilon$ model. This model is effective for wall-bounded and adverse pressure gradient flows in the boundary layer. Nevertheless, this model is known to perform poorly in laminar to turbulent transition.

The $SST-k-\omega$ model is an improved version of the standard $k-\omega$ model. It uses the original Wilcox $k-\omega$ formulation near walls. Again, it switches to the $k-\varepsilon$ behaviour while resolving the free stream. The adjustment of eddy viscosity formulation enables this model to deal with the transport effects of the turbulent shear stress accurately. As a result, it will avoid the common problem associated with standard $k-\omega$ model.

Achieving convergence in unsteady case of VAWT is time consuming specially for the convergence criteria of 10^{-5}, which is used in this study. In order to achieve convergence in a reasonable time, under relaxation is put in use. Under-relaxation factor of 0.3 for pressure equation, 0.7 for turbulent kinetic energy k, and 0.8 for velocity equation are used.

The deviation between the torque coefficient obtained from the fourth and fifth revolution is less than 5%. Therefore, it was assumed that the steady periodic output was achieved after 4–5 revolutions. It could be seen from Table 4.5 that the result obtained from $SST-k-\omega$ model is the closest one to the experimental value. In the simulation, the influence of rotating and support arm was ignored. If those entities were included, the outcome would have been different. The value of Power coefficient (C_P) would have reduced.

Table 4.5: Numerical and experimental results

Description	Power coefficient	Computational time for 1s of computational case	Deviation from experimental data
RNG k-epsilon	0.161	45.2 hours	15.7%
SST k-omega	0.1461	48.6 hours	4.61%
S-A	0.114	31.4 hours	18.07%
Experimental	0.1391	-	-

Therefore, $SST-k-\omega$ is selected as the turbulence model in this study. Since the regime of the system (low Reynolds number) is laminar, $k-\varepsilon$ and Spallart–Allmaras model cannot capture and predict the flow development, especially in laminar separation bubbles. Thus, the $SST-k-\omega$ model can be utilized as a low Reynolds turbulence model without any extra damping functions. This model is not only able to provide very good prediction of the turbulence in adverse pressure gradients but also it is capable to capture the separating flow. Furthermore, the shear stress transport (SST) formulation is formed by combining $k-\omega$ and $k-\varepsilon$ models. This structure assists SST method to switch to the $k-\varepsilon$ model in order to avoid $k-\omega$ problem in inlet free-stream turbulence properties and use the $k-\omega$ formulation in the inner parts of the boundary layer.

4.3.3 Mesh Dependency Study

Table 4.4 gives the specifications of meshes used in this study. The power coefficients obtained from each mesh resolution are compared to achieve the best mesh density. Variation of torque coefficient by azimuth angle for different mesh densities are shown in Figure 4.6. It is also apparent from this picture that the difference between M-2 and M-3 is negligible. Hence, the mesh strategy with less number of cells (M-2) is chosen to minimize the computation cost.

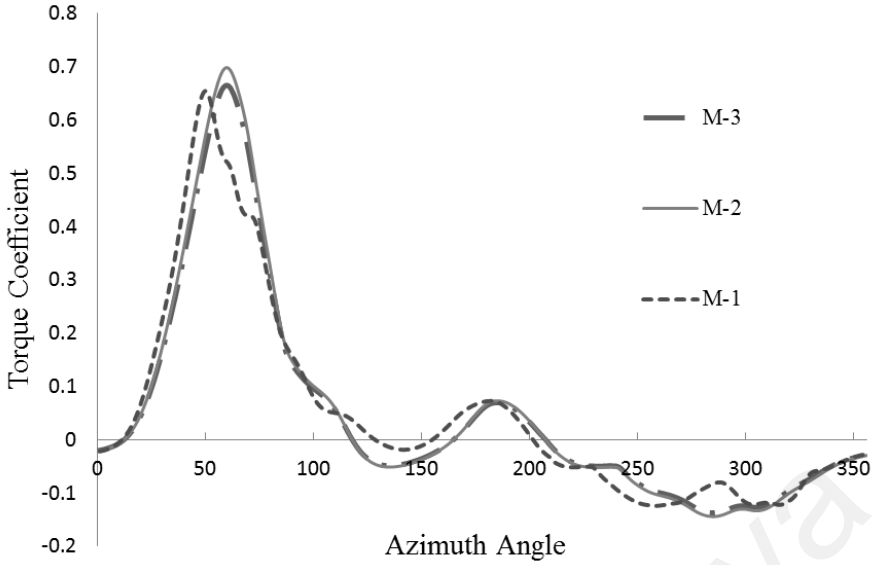

Figure 4.6: Variation of torque coefficient by azimuth angle for different mesh densities

A more accurate method can be utilized to ensure the mesh independency is achieved. Roache et al. (2014) have described the method of using Richardson extrapolation for finding the required mesh resolution and convergence. Almohammadi et al. (2013) also reported the use of this method. The mesh resolution required for accurate result is identified as:

$$Cp_{exact} = \bar{C}p_1 + \frac{Cp_1 - Cp2}{r^P - 1} + \text{Higher order truncation} \tag{4.5}$$

Here the subscripts refer to different mesh resolution levels. The quantity p denotes the order of accuracy. Here the order of accuracy was assumed to be 2. As for catching vortices and resolving dynamic stall, high resolution meshing has been provided near the blade, there is no need to refine other parts of the computational domain. The process of refining is briefly discussed in Section 4.3.1. The apparent convergence study is defined by the following equation:

$$R^* = \frac{Cp_2 - Cp_1}{Cp_3 - Cp_2} \tag{4.6}$$

If,

R* > 1 Monotonic divergence

1 > R* > 0 Monotonic convergence

0 > R*> −1 Oscillatory convergence

R* < −1 Oscillatory divergence

The mesh convergence is found to be -0.641 for this study. Therefore, since it is an oscillatory convergence case, it can successfully be concluded that the mesh dependency is achieved.

4.3.4 Time Increment Dependency

The accuracy and convergence of a CFD study is highly dependent on choosing the right time step (Qin et al., 2011). Four different time steps based on the VAWT rotational speed were considered to achieve a reliable result. The largest d*t* was equal to $3°\omega^{-1}$; equivalent to three-degree rotation and the smallest one was $0.5°\omega^{-1}$; equivalent to half a degree rotation when the tip speed ratio was 1.2.

As Figure 4.7 illustrates, a trivial difference between torque coefficient of $dt = 1°\omega^{-1}$ and $0.5°\omega^{-1}$ existed. Therefore, a time step of $1°\omega^{-1}$ (0.00025 s) was chosen for successive numerical simulations in order to save computational time and cost.

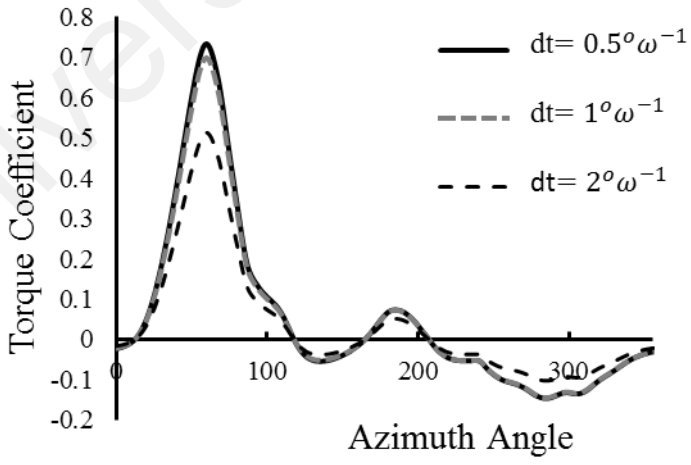

Figure 4.7: Time dependency study

4.3.5 Final Parameters

From the discussion of the turbulence models, it is evident that S–A is not compatible with the present objectives. The performance of $RNG-k-\varepsilon$ and $SST-k-\omega$ is

almost similar. However, $SST-k-\omega$ is believed to capture the wake vortices better than $RNG-k-\varepsilon$. Again, the result obtained from $SST-k-\omega$ is the closest to the experimental value. That is why turbulence model $SST-k-\omega$ has been chosen. As seen from the mesh dependency analysis, the result obtained from the finest mesh M-3 does not differ much with the medium fine mesh M-2. That is why M-2 mesh has been chosen. Finally, the chosen time step is $1°\omega^{-1}$ equals to 0.00025 s.

4.4 CFD Validation

The simulation results are validated using the experimental data from Laboratory test. The specification of the experimental apparatus is described in previous chapter. The simulations are done for seven revolutions and the results are obtained from the last three revolutions average.

Figure 4.8 shows the comparison of power coefficient between CFD simulation and experimental result for TSR in range of 0.45 to 1.5. It is apparent that the simulation result is in good agreement with the experimental values. Considering the fact that in 2D simulations the effect of supporting arms and rotor shaft are neglected, the obtained higher power coefficient comparing to actual ones is justifiable. The discrepancies may also occur due to insufficient mesh resolution, and turbulence modelling. According to the popular definition of Reynolds number of wind turbine, the characteristic length should be the diameter of the rotor disc. The Reynolds number in this study is 1.58×10^5. However, the blades experience relative velocity with the change of TSR, and the Reynolds number varies from 1.38×10^5 to 1.90×10^6. In this range, the turbulent flow is expected around the blade. The deviations of the present study are in a satisfactory range in comparison to some existing papers (Howell et al., 2010; Qin et al., 2011).

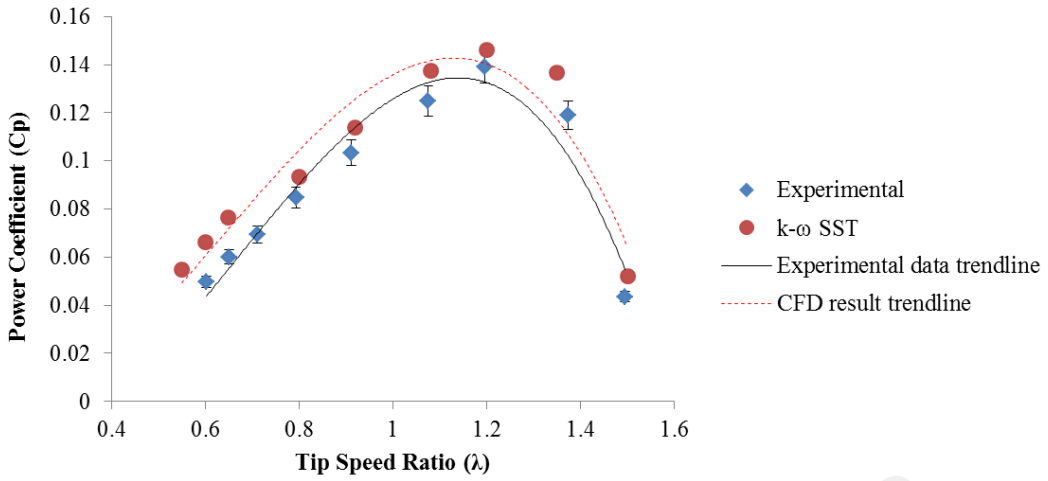

Figure 4.8: Power coefficients obtained by CFD simulation and experimental result.

4.5 Computational Fluid Dynamic (CFD) results

In order to improve the exhaust air recovery system design, two diffuser plates and four guide vanes were introduced to it. A detailed two-dimensional model of the proposed design is illustrated in Figure 4.9. The effect of added features of the VAWT performance is discussed in the following sections.

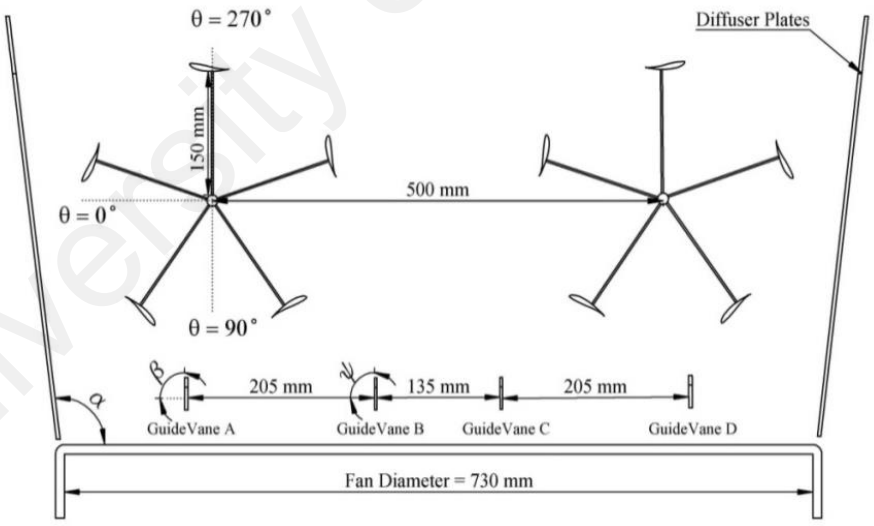

Figure 4.9: Two-dimensional (2D) model of the exhaust air energy recovery turbine

4.5.1 The Effect of the Diffuser Angle

As it is understood, the generated power is correlative to the cubed wind speed. Therefore, by even a minor increment in the wind velocity, a considerable increase in

power output can be obtained. Enhancement of the wind velocity around a wind turbine by using the fluid dynamic nature, especially by concentrating the wind energy locally, has always been considered an effective way to boost the wind turbine's output power.

Wind-concentrating devices known as diffusers have been widely employed in wind turbines in order to enhance the power generation. According to the basic laws of conservation of mass and energy—called Bernoulli's law—the mass flow is proportional to the area ratio (A_{exit} / A_{inflow}). Therefore, more mass flow can be increased if the exit area of the fluid is larger than its inflow area. Unfortunately, nature is not that generous. To be more precise, opening angles less than 10° have to be used to avoid what is called flow separation (Schaffarczyk, 2014). Therefore, in this study, 5°, 7°, and 9° were selected for the diffuser plates' angle (α). The engineering task then is to find a reasonable area ratio. Serious work started in 1956 by Liley and Rainbird (1956) and efforts up to 2007 were summarized by Van Bussel (2007).

At the first step, two diffuser plates with three different angles were introduced while guide vanes A and B were kept at 90°. The TSR in all cases, the same as the parametric study section, was assumed 2.2. The comparison of the torque coefficients obtained from a single blade in each arrangement is shown in Figure 4.10. As is clear, the diffuser with 7° has the higher peak as well as a more positive torque area. Figure 4.11 illustrates the power output for the four different designs. While the diffuser with 5° and 9° degree shows almost the same amount, the 7° diffuser improves the power by almost 5% compared to the design without diffusers. It is thus concluded that the optimum angle for the diffuser plates is 7°. This result is in good agreement with the experimental data achieved by Chong et al. (2014) and previous research done by Abe et al. (2005).

This improvement is justified by considering the fact that the diffuser-plates are causing a flow augmentation effect, which leads to a discharged airflow increment based on Bernoulli's principle. Ultimately, this increased volumetric flow rate interacts with

the VAWT blades, resulting in a higher energy output. According to a previous research on exhaust air energy recovery wind turbine by Fazlizan et al. (2015), utilizing the diffuser plates can also improve the fan airflow rate by 6.70% compared to bare cooling tower.

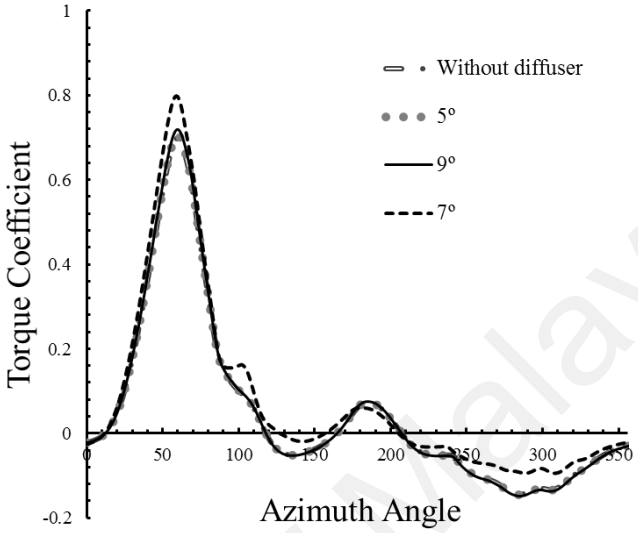

Figure 4.10: Effect of angle of diffusers on torque coefficient

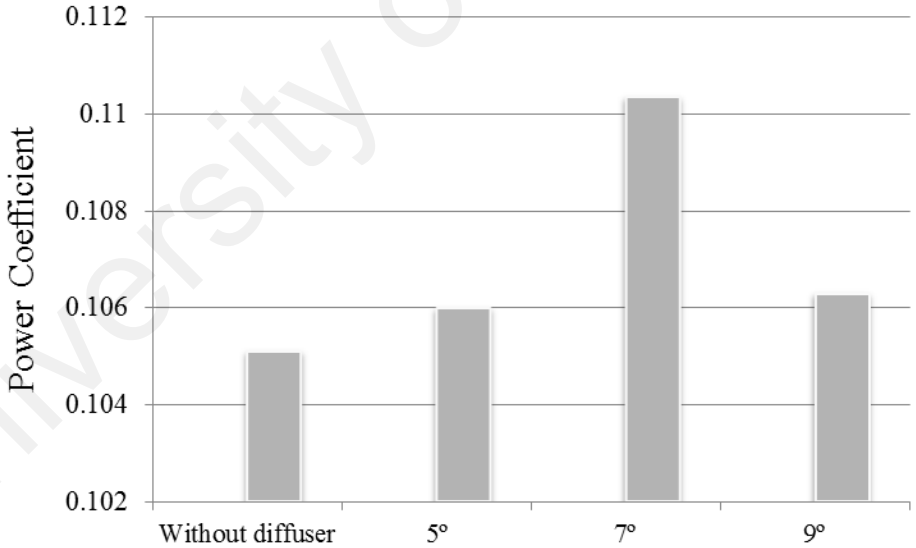

Figure 4.11: Power coefficient of different diffuser plate arrangements

4.5.2 The Effect of Guide Vanes

Considering the optimum angle of the diffuser plates to be 7°, the next step is to change the angles of the guide vanes. This step was done in two stages by rotating a single guide vane at each stage.

4.5.2.1 Guide Vane A

The effects of eleven different angles in the range of 30° to 130° with intervals of 10 are studied in this stage. The principle behind the guide vanes are the same as the diffuser. They are capable of creating low-pressure zones and consequently increasing the airflow speed. As is clear from Figure 4.12, the guide vane with an angle of 70° provides the highest output power among all the other arrangements. One of the reasons that the 30° and 130° guide vanes provide the lowest power coefficient is that they mostly acted as a blockage for inlet wind by creating a large wake behind themselves.

The results and other specifications of the tests are tabulated in Table 3. The numbers after the letters A and B indicate the guide vane angles of β and ψ (see Figure 4.9). The torque (T) and power coefficient (C_p) were calculated using Equations (4) and (5), respectively. This table also indicates that β = 70° results in the highest power output. The relative deviations of the output power compared to the baseline design when both β and ψ are equal to 90°, are also tabulated in Table 4.6.

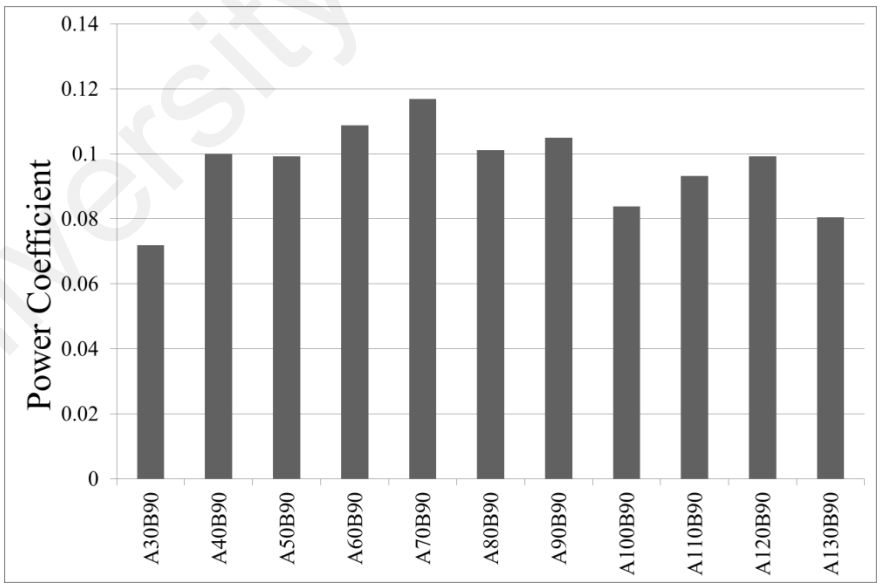

Figure 4.12: Effect of guide vane "A" angle on power coefficient

Table 4.6: The results and other specifications of the various cases

	C_m	T	TSR	C_p	P	Deviation from Baseline Design (%)
A30B90	0.032	0.024	2.2	0.071	1.86	−31.6176
A40B90	0.045	0.033	2.2	0.099	2.59	−4.77941
A50B90	0.045	0.033	2.2	0.098	2.57	−5.51471
A60B90	0.049	0.036	2.2	0.108	2.82	3.676471
A70B90	0.053	0.039	2.2	0.116	3.03	11.39706
A80B90	0.046	0.033	2.2	0.101	2.63	−3.30882
A90B90	0.047	0.035	2.2	0.105	2.72	0
A100B90	0.038	0.028	2.2	0.083	2.18	−19.8529
A110B90	0.042	0.031	2.2	0.093	2.42	−11.0294
A120B90	0.045	0.033	2.2	0.099	2.57	−5.51471
A130B90	0.036	0.027	2.2	0.08	2.09	−23.1618

C_m, Coefficient of momentum; T, Torque; TSR, Tip Speed Ratio; C_p , Coefficient of power; P, Generated power

Figure 4.13 compares the variation in the torque coefficient of the two different arrangements for a complete revolution. As clear, although before the azimuth angle of 90° the figures are almost identical, the 70° guide vane provides a higher torque coefficient afterwards, which leads to a higher average power coefficient. This increase can be more clearly observed in Figure 4.14, where the total torque coefficient of all five blades is shown. As is apparent utilization of the 70° guide vane provided a considerable enhancement in produced torque. Even though it is out of this study scope, it is noteworthy that this modification in design decreased the fluctuation rate in the torque diagram, which can result in less fatigue in the VAWT.

According to Figure 4.14, the most significant difference in torque coefficient for the two cases of $\beta = 90°$ and 70° occurs when $90° < \theta < 180°$. Therefore, the contour of the pressure coefficient at $\theta = 120°$ was plotted in Figure 4.15 to investigate the possible reason for this increment. It can be observed in this figure that when the 70° guide vane

is used the distribution of the low-pressure zone on the top of the blade is significantly improved. This phenomenon caused more pressure difference between the low and top of the blade leading to a higher torque.

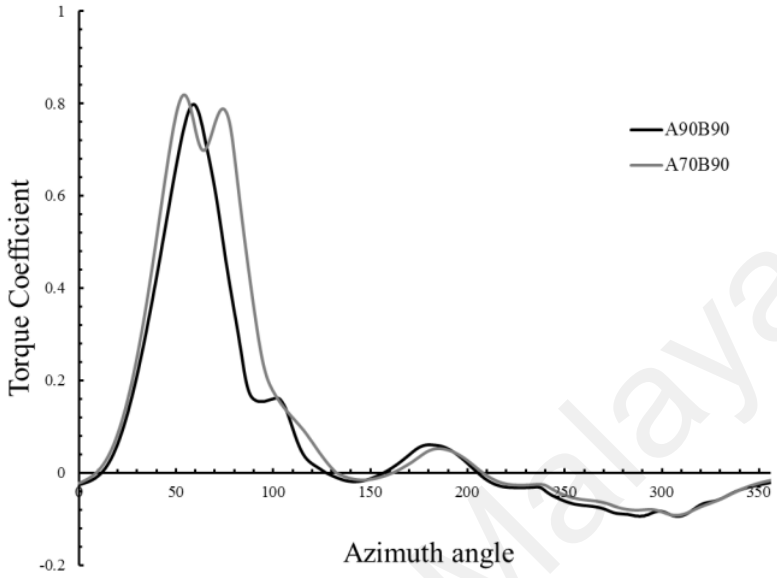

Figure 4.13: Torque coefficient of a single blade

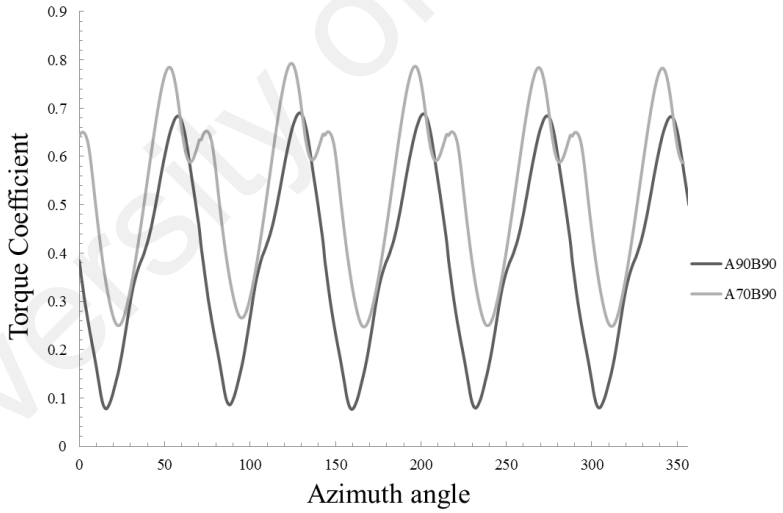

Figure 4.14 Total torque coefficient of five blades

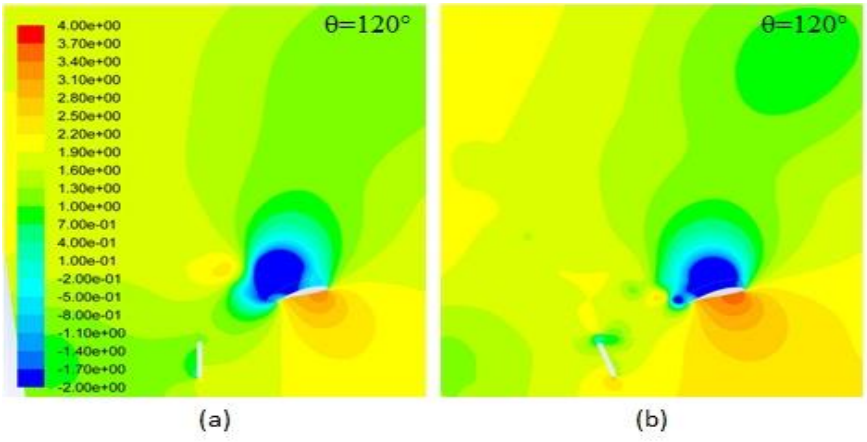

Figure 4.15: Pressure coefficient contour; (a) β = 90° and (b) β = 70°

4.5.2.2 Guide Vane B

The next stage proceeded by fixing the guide vane at β = 70°. Seven different arrangements in the range of ψ = 30° to 90° with 10 intervals were considered for guide vane B. Due to the position of this guide vane, angles greater than 90° were ignored. As is obvious in Figure 4.16, the greatest power coefficient belongs to the arrangement with ψ = 60° when it is equal to 0.134.

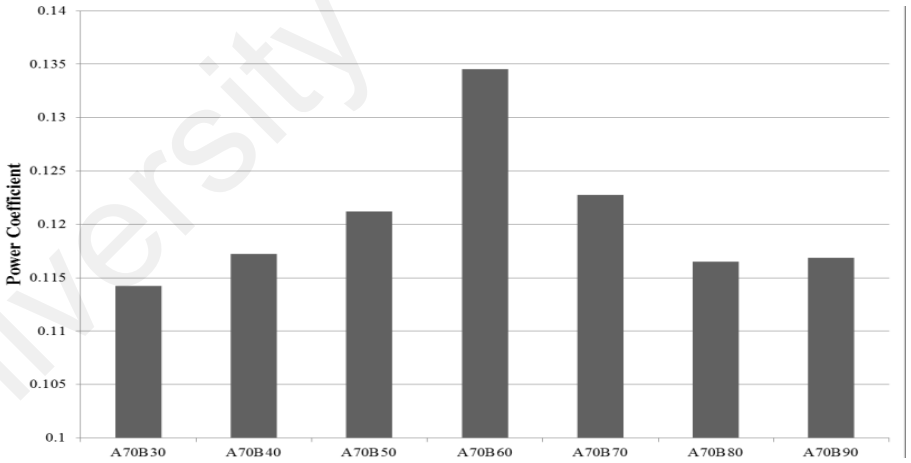

Figure 4.16: Effect of guide vane B angle on power coefficient

The results and other specifications of the tests are shown in Table 4.7. From this table it is indicated that ψ = 60° results in the highest power output with 3.49 W. The first column from the right shows the relative deviations of the output power from the baseline design, when both β and ψ are equal to 90°.

Table 4.7: The results and other specifications of the various cases

	C_m	T	TSR	C_p	P	Deviation from Baseline Design (%)
A70B30	0.051	0.038	2.2	0.114	2.96	8.823529
A70B40	0.053	0.039	2.2	0.117	3.04	11.76471
A70B50	0.055	0.04	2.2	0.121	3.15	15.80882
A70B60	0.061	0.045	2.2	0.134	3.49	28.30882
A70B70	0.055	0.041	2.2	0.122	3.19	17.27941
A70B80	0.052	0.039	2.2	0.1165	3.02	11.02941
A70B90	0.053	0.0392	2.2	0.1168	3.03	11.39706

C_m, Coefficient of momentum; T, Torque; TSR, Tip Speed Ratio; C_p , Coefficient of power; P, Generated power

The torque coefficient variation in two different arrangements for a complete revolution is compared in Figure 4.17. As it is clear, from θ = 0° to θ = 160°, both diagrams are relatively congruent; however, after this point the torque coefficient related to ψ = 60° is considerably higher until the end of the cycle, leading to a 15% higher average torque coefficient.

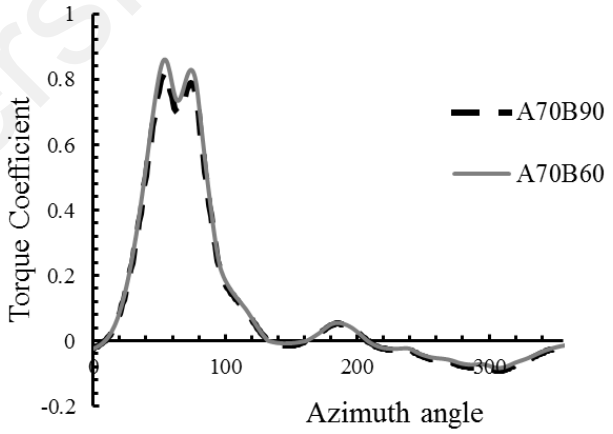

Figure 4.17: Torque coefficient of a single blade

4.6 Summary

A two-dimensional CFD study was carried out on a novel wind turbine design. The effects of different diffuser plate angles and guide vane angles were investigated. It was derived from the results that by introducing diffusers and then guide vanes, the overall

power output of the wind turbine was improved by approximately 5% and 34%, respectively, compared to using a VAWT alone. In the case of the diffusers, the optimum angle was found to be 7°, while for guide vanes A and B; it was 70° and 60°, respectively. These results are in good agreement with experimental results obtained in the laboratory. Overall, it can be concluded that exhaust air recovery turbines offer a promising opportunity in green technology.

CHAPTER 5: OPTIMIZATION

In order to achieve highest power output from the exhaust air energy recovery wind turbine generator, a precise design optimization study is carried out. The effects of the rotor position and wind-concentrating devices on the wind turbine generator performance are studied simultaneously.

5.1 Design Parameters

5.1.1 The Position of the Rotor

Since the exhaust fan air velocity profile is not uniform (see Figure 5.1), the position of the rotor on the top of it can have great influence on the output power. According to the diffuser plates position and the exhaust fan diameter the horizontal and vertical position of the rotors can be varied in range of 150-250 mm and 400-500 mm respectively. Therefore, by taking the mid-point into account, three various horizontal locations of X = 150, 200, 250 mm and vertical positions of Y = 400, 450, 500 mm were considered in the optimization study. These positions are illustrated in Figure 5.1 for better understanding.

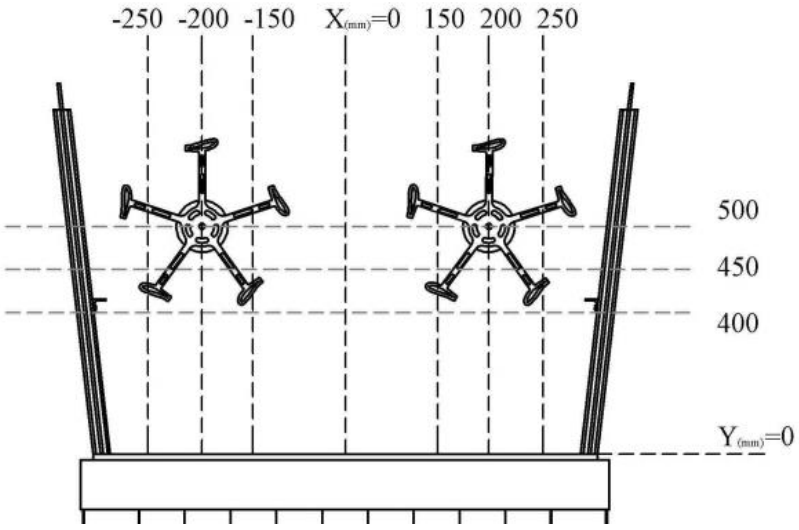

Figure 5.1: Various positions of the VAWTs

5.1.2 Diffuser Plates

Wind-concentrating devices known as diffusers have been widely employed in wind turbines in order to enhance the power generation. In the previous chapter, it was shown that the optimum angle for diffuser plates in this system is 7º. Therefore, two diffuser plates with 7º inclination were introduced to the design. However, in this study three various modified diffuser plates were taken into account to enhance the air velocity as much as possible. The modification was done by adjoining a semi-circular shape to the diffuser plate to improve the wind concentration. The angle of the semi-circular against the diffuser plate (α) is then varied from 0º to 45º by 22.5º iteration. The schematic designs of the modified diffuser plates are shown in Figure 5.2.

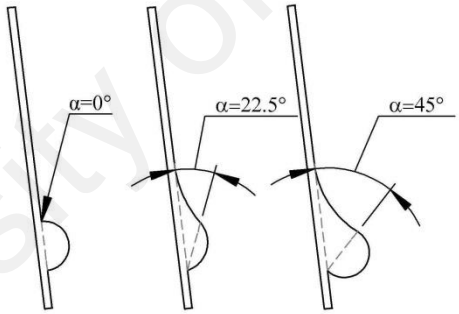

Figure 5.2: Three various diffuser shapes

5.1.3 Separator Plate

The main design consists of two contra-rotating five blades rotors mounted on top of a cooling system exhaust fan. After doing some initial studies, it was perceived that the rotors are likely to have a negative interaction due to the wakes resulted by rotors rotation. Therefore, a separator plate was introduced between two rotors. In order to investigate the effect of this separator plate a categorical factor was introduced to optimization study. This categorical factor consists of three states, without the separator

plate, plain separator plate, and modified separator plate. The summary of all optimization factors are schematically shown in Figure 5.3.

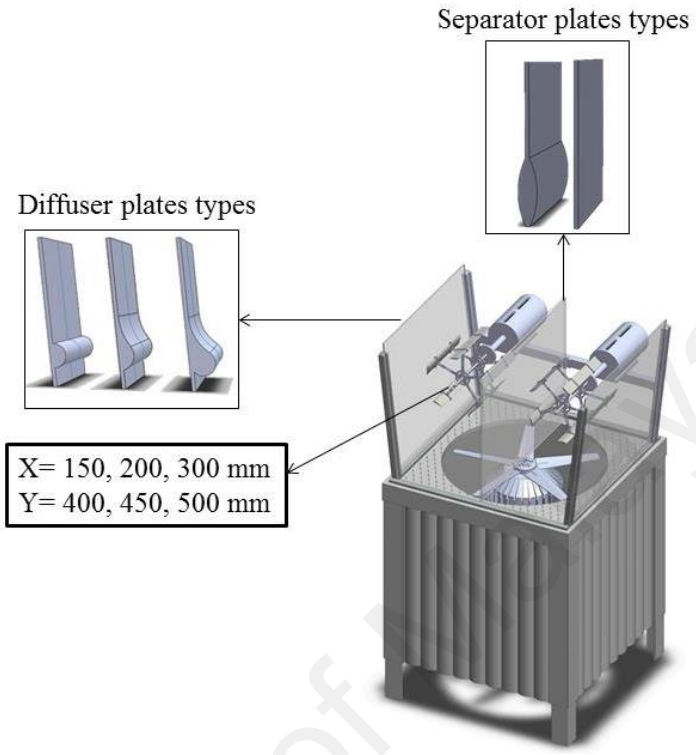

Figure 5.3: Optimization factors

5.2 Optimization

After inserting the optimization factors into the DOE software, 60 cases were defined to be done in order to be able to do the optimization. These 60 cases are done using CFD with parameters described in previous sections. The obtained results are then analysed using Design-Expert v.8 software. The achieved results will be discussed in following sections.

5.3 Computational Fluid Dynamic (CFD) Study

ANSYS Fluent 15.0 is used to simulate different 60 design points. The CFD parameters are the same as ones obtained from parametric study in Chapter 4. Therefore, $SST-k-\omega$ is used as the turbulence model, the chosen time step is $1°\omega^{-1}$ equals to 0.00025 s and the meshing strategy is also identical to the one used in validation case. Figure 5.4 shows geometry models and meshes of different cases.

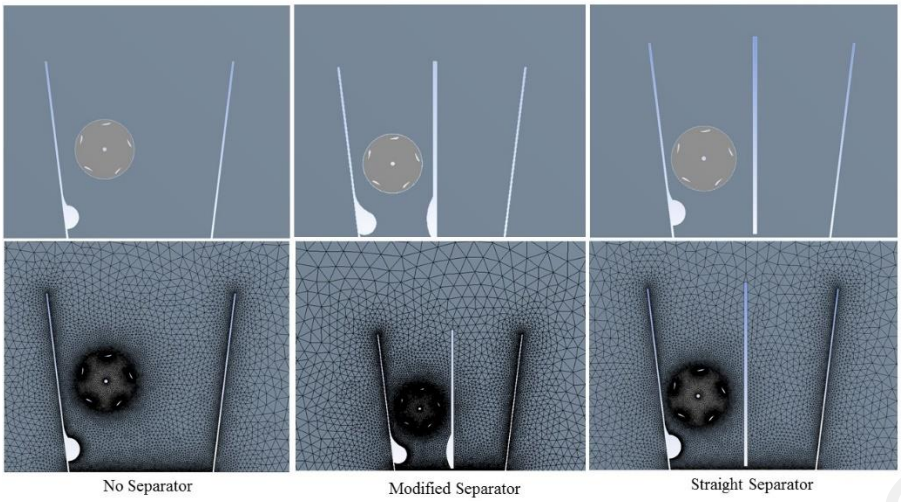

Figure 5.4: Geometry models and meshes

The table of design points inserted in ANSYS Fluent are presented in Appendix D.

5.4 Optimization Results

The data obtained from CFD cases are then inserted to the Design Expert ® software to carry out the optimization. In following sections, the accuracy of the results will firstly be analysed then the results will be presented.

5.4.1 Fitting the Model

In this section, further statistical analysis is accomplished to make conclusions more confidently. The mathematical model found after fitting the function to the data can sometimes not satisfactorily describe the experimental domain studied. The more reliable way to evaluate the quality of the model fitted is by the application of analysis of variance (ANOVA). The central idea of ANOVA is to compare the variation due to the treatment (change in the combination of variable levels) with the variation due to random errors inherent to the measurements of the generated responses (Bezerra et al., 2008). This comparison makes the evaluation of the regression significance possible to be used in order to predict responses according to the experimental variance sources.

Design-Expert v.8 software is utilized to provide ANOVA analysis based on numerical and experimental dataset. In general, this software provides a statistical test to

verify the role of various parameters in achievement of higher accuracy in a certain problem. For instance, in this work, it is desirable to identify how changing various parameters, such as rotor position, diffuser angle and separator plate shape can contribute to better VAWT performance. As it is indicated so far, different parameters are varying to achieve the best numerical prediction. For instance, three different turbulent models are tested. In addition, three various mesh densities have been compared. Based on ANOVA results, it is defined that variation of rotor position has the most impact on predictions.

If a model shows a significant regression and a non-significant lack of fit, it will be considered as a well-fitted model to the experimental data. It means that the equation of regression should describe the majority of variation, and the remainder of the variation will definitely exist due to the residuals. It should be considered that the pure error (random fluctuation of measurements), not the lack of fit, is the main cause of the most residuals-related variations. The pure error is directly related to the model quality. The result of the ANOVA analysis is tabulated in Table 5.1. Since the value of R^2 is close to 1 (0.983), the regression model properly fits the experimental data, and the lack of fit is not significant relative to the pure error. Thus, this model is suitable to generate the response surface.

Table 5.1: ANOVA for Response Surface Quadratic

Analysis of variance table					
Source	Sum of Squares	Mean Square	F Value	p-value Prob>F	
Model	0.11	5.724E-003	63.70	< 0.0001	significant
A-X	0.060	0.060	666.57	< 0.0001	
B-Y	7.177E-003	7.177E-003	79.87	< 0.0001	
C-Alpha	2.028E-003	2.028E-003	22.56	< 0.0001	
D-Separator Plate	0.015	7.561E-003	84.14	< 0.0001	
AB	1.810E-003	1.810E-003	20.14	< 0.0001	
AC	3.639E-003	3.639E-003	40.50	< 0.0001	
AD	1.371E-003	6.855E-004	7.63	0.0016	
BC	2.096E-004	2.096E-004	2.33	0.1348	
BD	1.966E-003	9.831E-004	10.94	0.0002	
A^2	2.352E-004	2.352E-004	2.62	0.1138	
B^2	2.071E-003	2.071E-003	23.04	< 0.0001	
C^2	7.733E-003	7.733E-003	86.05	< 0.0001	
A^2D	1.491E-003	7.453E-004	8.29	0.0010	
AB^2	8.357E-004	8.357E-004	9.30	0.0041	
B^2D	2.336E-003	1.168E-003	13.00	< 0.0001	
R^2					0.9830
Lack of Fit	3.402E-003	1.417E-004	3.70	< 0.0001	not significant

Figure 5.5 shows the comparison between the predicted and actual results. The model accuracy is higher if the data points are closer to the diagonal line. It is apparent from the figure that, for this case, the model is acceptably predicted the results. Therefore, this model is suitable to generate the response surface plots.

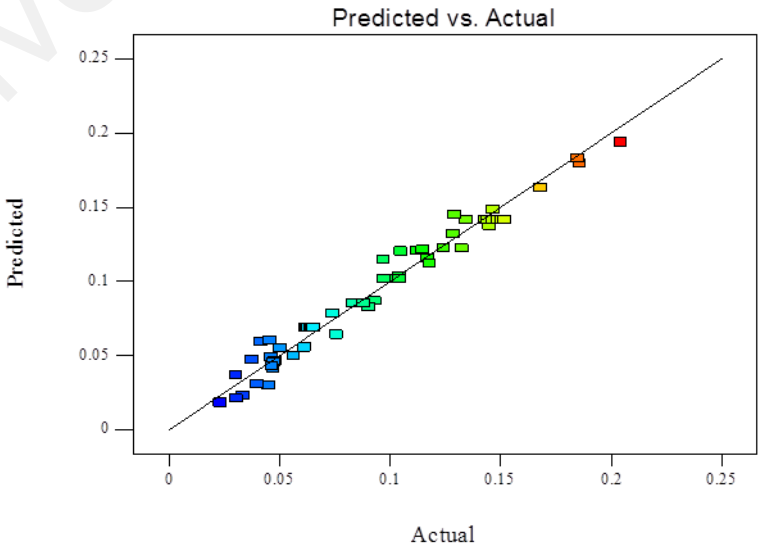

Figure 5.5: Predicted vs. Actual results

5.4.2 Effect of Rotor Position

The surface response plots can be used to visualise the predicted model equations. This graphical presentation is an *n*-dimensional surface in the (*n*+1)-dimensional space. Conventionally, it is drawn as a two-dimensional presentation of a three-dimensional plot. Therefore, in case of having three or more variables, it is possible only to visualise the graph if one or more variables are assumed constant. Figure 5.6 depicts Surface response profile showing the effect of rotor position on power coefficient in various designs. It is apparent from Figure 5.6 that the effect of rotor position in more significant in presence of the modified separator. The maximum power output is achieved when the VAWT rotor is installed at X = 250 mm and Y = 400 mm. It can also be seen from the figure that at X = 150 mm (nearer to the exhaust fan centre), the vertical position (Y) does not own any significant impact on output power.

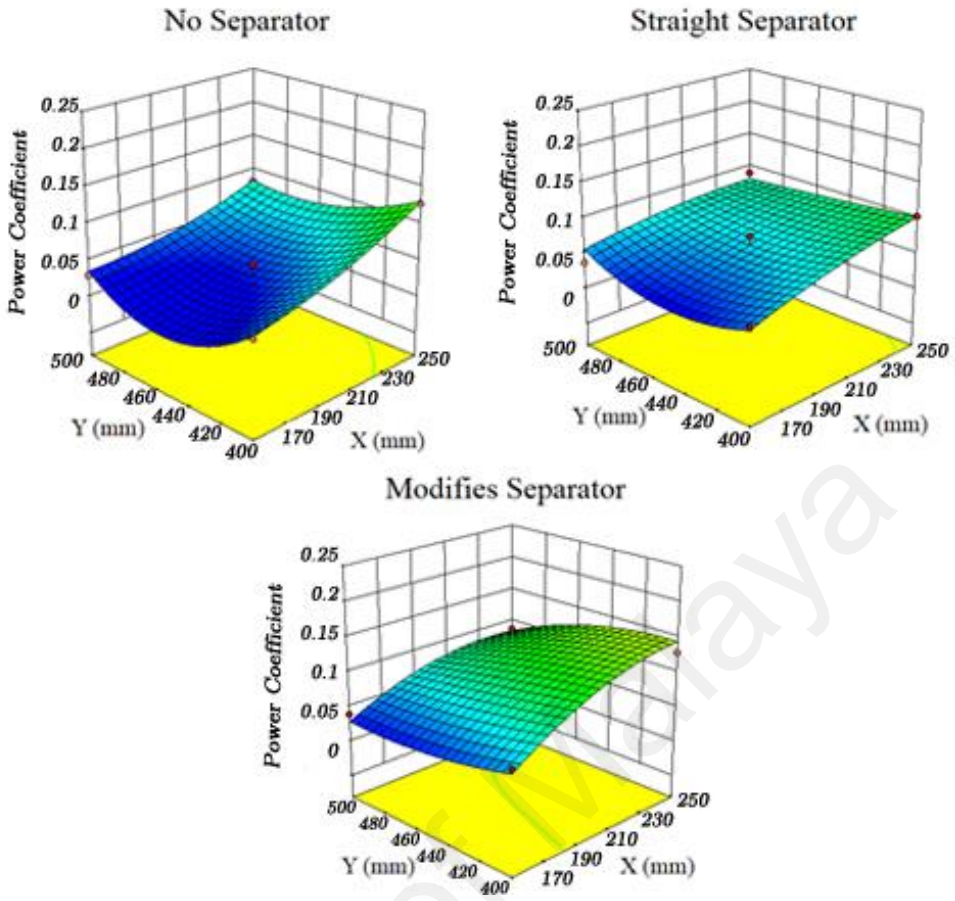

Figure 5.6: Surface response profile showing the effect of rotor position on power coefficient in various designs

To achieve a better understanding of the rotor position effect on the VAWT output, velocity contours of three different horizontal positions are illustrated in Figure 5.7. The exhaust fan velocity follows the pattern shown in Figure 5.7. When the rotor is installed at X = 150 mm, nearly half of the rotor swept area is located in the low-velocity zone created by exhaust fan central shaft. The comparison between X = 200 mm and X = 250 mm shows that the latter provides a better position for the rotor by directing the high-velocity zone to the upwind section of the VAWT. Therefore, the results shown by the surface response plot are justifiable.

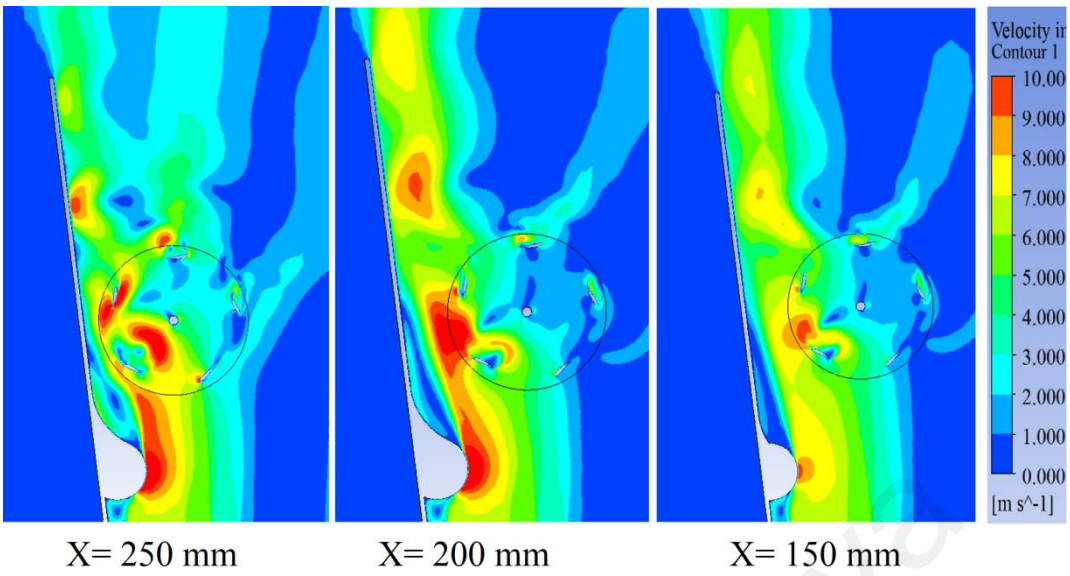

Figure 5.7: Velocity contour for different horizontal positions

5.4.3 Effect of Diffuser Plates Modification

The surface plots in Figure 5.8 show the effect of diffuser modifying curvature angle (α) on the power coefficient in different positions. Figure 5.8 (a) depicts the variation of C_p against X and α when Y= 400 mm. When looking at this figure, it is apparent that the influence of α is greater when X is higher and the C_p is peaked when α is in the range of 25º to 35º. The effect of Y and α at X = 250 mm is illustrated in Figure 5.8 (b). On the contrary to the previous figure, α affects the C_p more significantly at lower Y values. Similarly, the highest C_p is achieved when $25^o \leq \alpha \leq 35^o$.

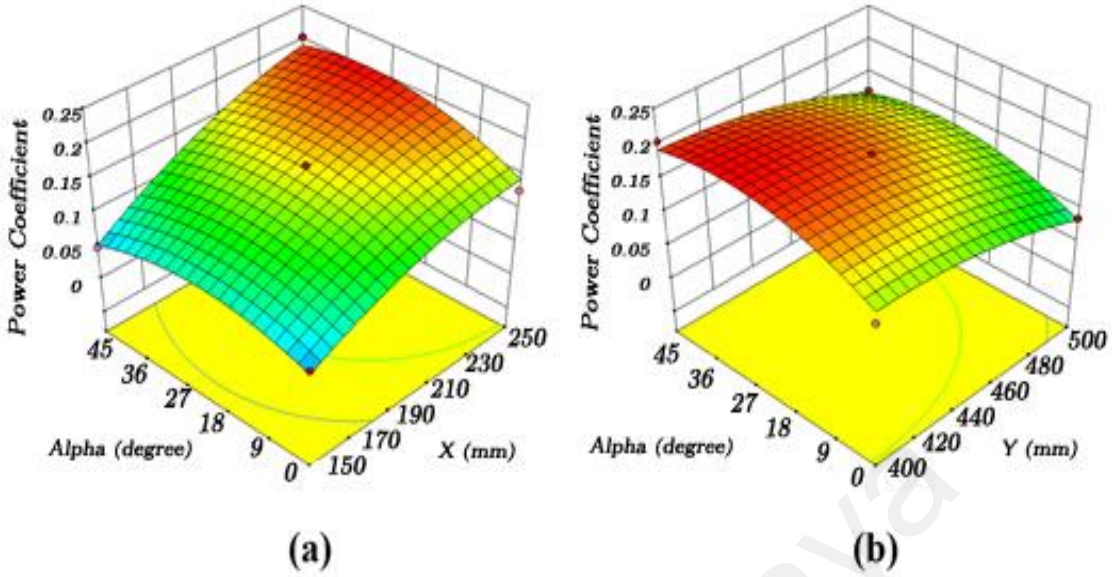

Figure 5.8: Surface response profile of effect of α on power coefficient

Overall, α demonstrate a significant influence on the wind turbine performance. Form post processing of the optimization results it was found out that the highest C_p is achieved when $\alpha = 32.09°$. At this point, a 39.81% improvement in C_p can be observed.

Three lines were considered in the computational domain to compare the velocity magnitude obtained from various diffuser angles. The locations of the lines are illustrated in Figure 5.9. Line 1, 2 and 3 are assumed to be 15, 20 and 25 cm above the inlet boundary respectively.

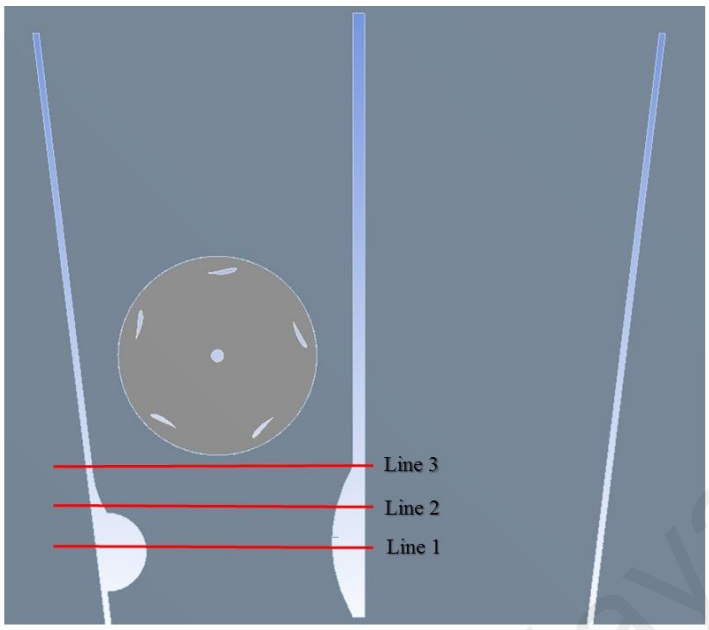

Figure 5.9: The location of the probe lines

Velocity magnitude for α=0º, 22.5º and 45º along the lines is depicted in Figure 5.10. It is apparent that in all lines, the modified diffuser plate with α=22.5º has created the highest velocity. Therefore, utilizing this design is able to improve the power output significantly.

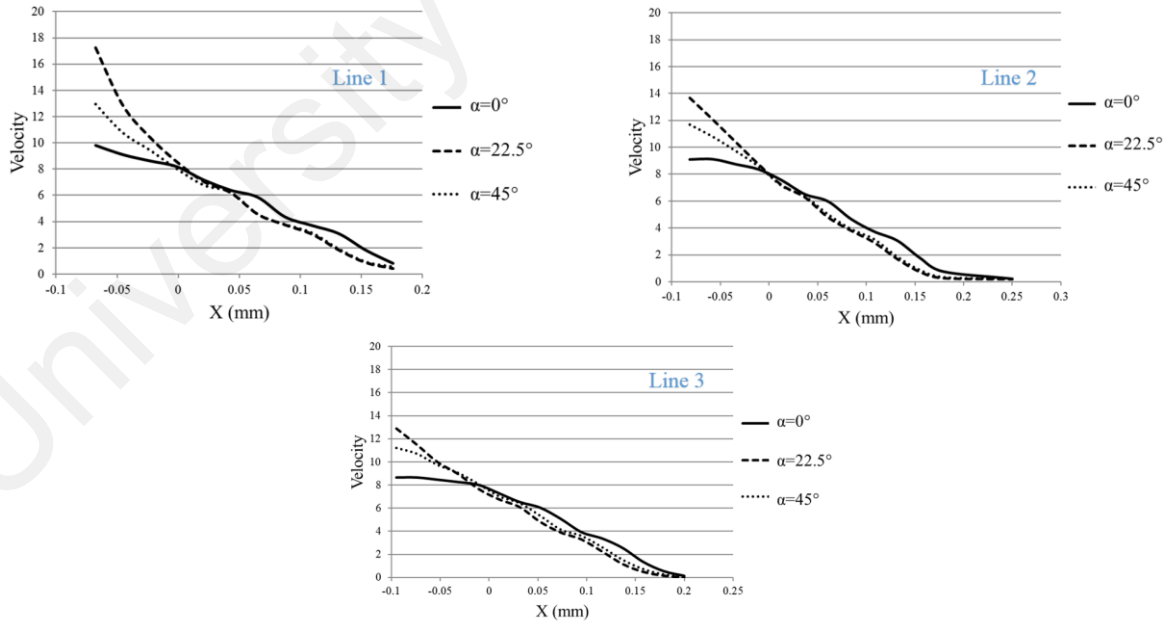

Figure 5.10: Comparison of velocity magnitude along Lines 1-3 for various diffuser setup

The total pressure contour of cased with different α value is shown in Figure 5.11. Comparing the flow behaviour in cases of α=0º and α=22.5º shows that the latter has

successfully concentrated the wind flow and increased the local total pressure by 26% (from 86 pa to 109 pa). It cannot also be unseen that the low-pressure zone above the airfoil is much higher when α=22.5º which results in a higher-pressure difference on turbine blades and increase the lift force. When α=45º, an unwilling disturbance is created in the flow pattern. It is also apparent that this design might cause some blockage effect on the exhaust fan caused by the higher-pressure zone below it.

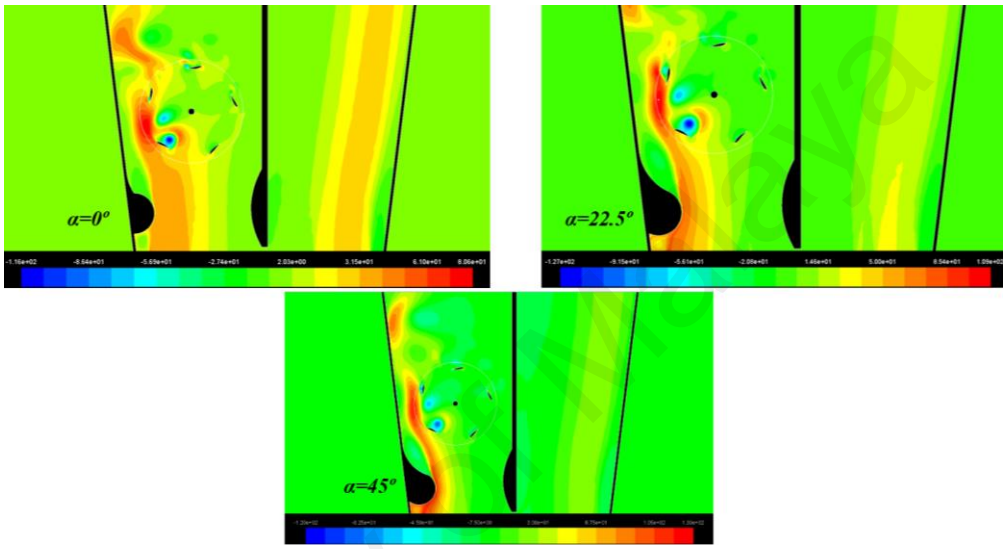

Figure 5.11: Total pressure contour of cases with various diffuser optimization

5.4.4 Effect of Separator Plates

The effect of the separator plates on power coefficient is shown as line graphs in Figure 5.12. It can clearly be seen that while installing the straight separator plate creates a noticeable improvement, modifying its shape can even have greater positive influence on the power generation. The maximum improvement can be achieved by installing a modified separator plate comparing to design without it is around 34%. The reason behind this improvement is described in section 5.1.3.

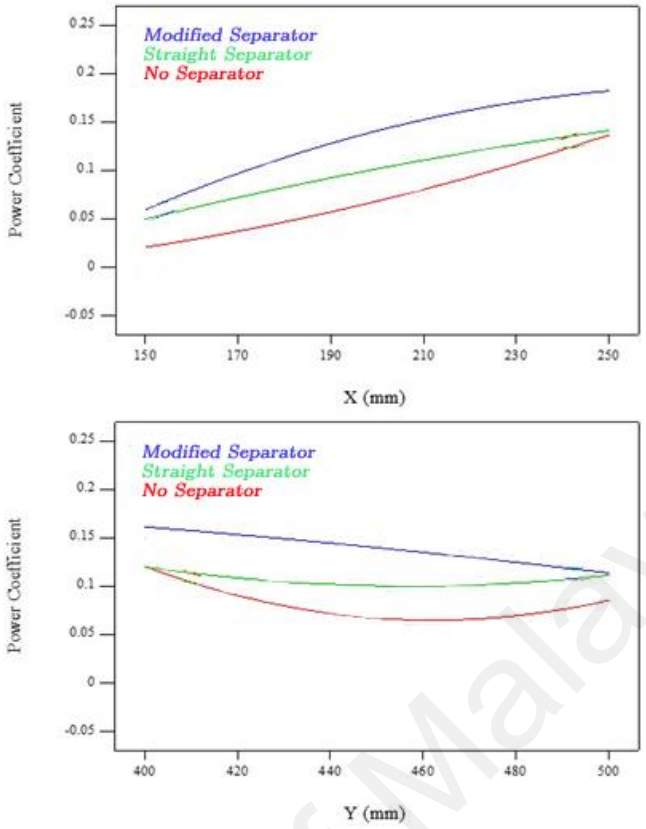

Figure 5.12: Effect of various separator plates on power coefficient

The torque coefficients obtained from a single blade during a complete revolution are depicted in Figure 5.13. It can be seen in this figure that using a separator plate can improve the torque coefficient significantly. Although, the effect of straight and modified separators is the same from 0° to 180°, higher torque coefficient is achieved by using the modified one. Any increase in torque coefficient will cause relative increment in wind turbine generated power. Thus, the modified separator is proven as an effective way to achieve higher performance.

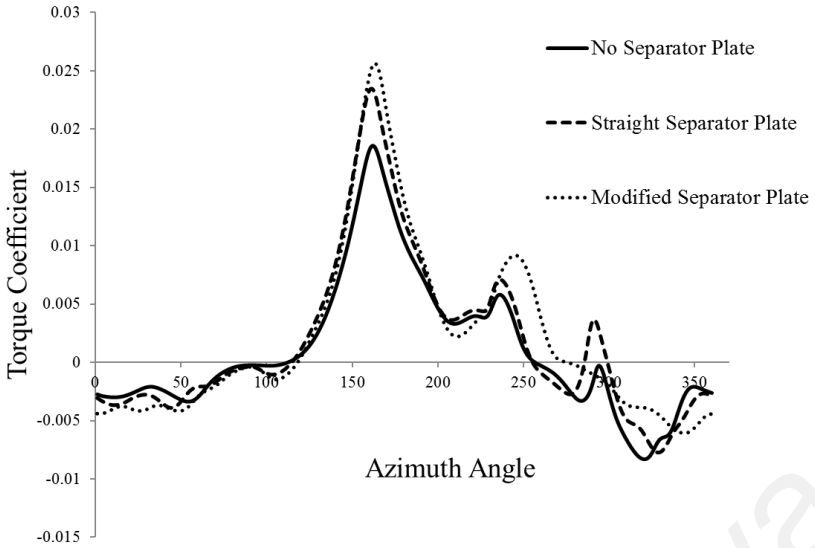

Figure 5.13: Effect of separator setups on torque coefficient

5.5 Prediction Equations

One of the main outputs of the optimization process is the prediction equations, which can be used in future studies and design with no need to carry out experimentations. Therefore, these equations are able to save a considerable amount of cost and time. The accuracy of these equations is analysed in ANOVA by monitoring 'Lack of Fit' parameter. Since catagoric factors cannot be considered in numerical equations, different equations were introduced for each catagoric factor. The prediction equations are shown in following equations.

Without separator plates:

$$\begin{aligned} C_p = {} & (6.98032) - (2.055\times10^{-2}X) - (3.137\times10^{-2}Y) + (2.079\times10^{-3}\alpha) + \\ & (9.152\times10^{-5}XY) + (1.094\times10^{-5}X\alpha) - (2.626\times10^{-6}Y\alpha) \\ & +(4.140\times10^{-6}X^2) + (3.529\times10^{-5}Y^2) - (6.047\times10^{-5}\alpha^2) - (1.055\times10^{-5}XY^2) \end{aligned} \quad (5.1)$$

Straight separator plates:

$$\begin{aligned} C_p = {} & (5.00191) - (1.814\times10^{-2}X) - (2.365\times10^{-2}Y) + (2.079\times10^{-3}\alpha) + \\ & (9.152\times10^{-5}XY) + (1.094\times10^{-5}X\alpha) - (2.626\times10^{-6}\alpha) - (2.494\times10^{-6}X^2) \\ & +(2.701\times10^{-5}Y^2) - (6.047\times10^{-5}\alpha^2) - (1.055\times10^{-7}XY^2) \end{aligned} \quad (5.2)$$

Modified separator plates:

$$C_p = (3.517) - (1.56\times10^{-2} X) - (1.775\times10^{-2} Y) + (2.079\times10^{-3} \alpha) + (9.152\times10^{-5} XY) + (1.094\times10^{-5} X\alpha) - (2.626\times10^{-6} Y\alpha) - (8.053\times10^{-6} X^2) + (2.003\times10^{-5} Y^2) - (6.047\times10^{-5} \alpha^2) - (1.055\times10^{-7} XY^2) \quad (5.3)$$

In these equations, X and Y are the horizontal and vertical positions of the VAWT rotor respectively and α is modified diffuser plate curvature angle. Validation of these equations by computational and experimental methods will be presented in section 5.7.

5.6 Optimized Design

The most optimized design parameters suggestion is one of the Design-Expert® outcomes. Based on the equations presented in the previous section, the top 10 designs with highest performance are introduced. Figure 5.14 shows the most optimum design suggested based on the optimization. It is clear that the maximum power coefficient achieved by this study is equal to 0.204284, which have 46.8% improvement comparing to the baseline design considered in Section 4.2. This improvement can be obtained when X=249.516 mm, Y= 401.57mm, α=30.219º and the modified separator is used.

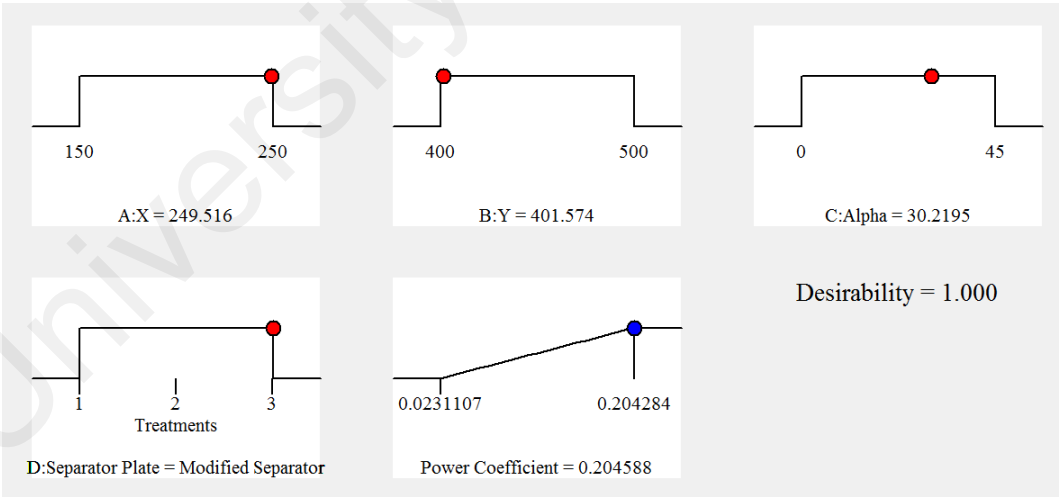

Figure 5.14: The optimum design suggested based on the optimization

5.7 Validation of the Optimization Results

All the optimization results are based on the obtained equations 5.1, 5.2 and 5.3. Although the ANOVA approved the accuracy of the prediction results in terms of R^2 and "Lack of fit", some computational and experimental studies are done to ensure the

results validity. Nine different designs, three for each catagoric factor, were considered in this part of study. The characteristic of each design as well as predicted, experimental and computational results of each case is tabulated in Table 5.2.

In computational study, the same meshing strategy and simulation parameter discussed in previous sections are used. An acceptable deviation can be seen between the predicted, computational and experimental study. Therefore, it can be concluded that this optimization is valid to be considered in further cases.

Table 5.2: Comparison of the predicted, experimental and computational results.

Design No.	X (mm)	Y (mm)	α (degree)	Separator plate	Predicted C_p	Experimental C_p	Computational C_p
1	250	400	30	No Separator	0.1909	0.2065	0.1966
2	200	400	25	No Separator	0.1232	0.1345	0.1281
3	250	450	30	No Separator	0.1411	0.1530	0.1458
4	250	400	30	Straight Separator	0.1606	0.1737	0.1654
5	200	400	25	Straight Separator	0.1222	0.1336	0.1272
6	250	400	30	Straight Separator	0.1447	0.1576	0.1501
7	250	400	30	Modified Separator	0.2045	0.2210	0.2104
8	200	400	25	Modified Separator	0.2042	0.2176	0.2073
9	250	450	30	Modified Separator	0.187	0.2054	0.1956

CHAPTER 6: TECHNICAL AND ECONOMIC FEASIBILITY OF THE EXHAUST AIR ENERGY RECOVERY TURBINE

In order to justify the feasibility of the exhaust air energy recovery system, some technical and economic factors should be investigated. In terms of technical critique, the fan motor power consumption will be monitored to ensure that the design does not create any blockage effect and extra load on the fan. Furthermore, the fan air intake will also be measured to check the effect of the energy recovery system on whole cooling tower performance. Finally, an economic assessment will be presented.

6.1 Effect of the Exhaust Air Energy Recovery Turbine Generator on Fan Motor Power Consumption and Airflow Rate

Investigating the effect of the energy recovery system on the fan power consumption is vital because in case of imposing any extra load or blockage on the cooling system the fan need to consume more power to keep the same performance. The fan power consumption is measured using the Fluke power analyser and the airflow rate is measure by the anemometer. The techniques to measure both are described in chapter 3. The study on the bare cooling tower showed that the bare fan consumes 672.78 W and provides 3.5624 m^3/s airflow rate. The cases, which were used to validate optimization results, will be considered in this part of study as well. The summary of the results obtained from experimental tests and the comparison with bare cooling tower fan are tabulated in Table 6.1. It is apparent from the table that installing the exhaust air recovery wind turbine on the top of a cooling tower has trivial but positive impact on the fan power consumption. Furthermore, the fan airflow rate is also increased. This increment is possibly happened due to the low-pressure zone created by the VAWT

rotation on the top of the exhaust fan. Overall, it can be concluded that the idea of using this energy recovery system is technically justifiable.

6.2 **Economic Assessment**

Initial capital, operating cost and payback time for any system is very important for investors. Although, renewable energy systems are generally characterized by high capital cost, their low operation costs make them cost-effective in a long span of time (Hafez and Bhattacharya, 2012). In this study, the initial capital of the investment includes the purchase of the wind turbine system, supporting structure and the first year of operation and maintenance. The exhaust air recovery wind turbine system consists of two units of VAWT, an inverter, a controller and a set of batteries. It is required to replace the battery set every 5 years and the inverter and controller need to be changed every 10 years (Fazlizan, 2016). The supporting structure design is inclusive of the diffusers. The estimated costs for the economic analysis are tabulated in

Table 6.1.These estimations are made based on information available in Appendix F.

Table 6.1: Comparative performance of cooling tower and wind turbine compared to bare cooling tower

Design Specification					Power Consumption			Airflow Rate		
Design No.	X (mm)	Y (mm)	α (°)	Separator plate	Bare fan (W)	Experimental cases (W)	% of difference compared to bare fan	Bare fan (m^3/s)	Experimental cases (m^3/s)	% of difference compared to bare fan
1	250	400	30	No Separator	672.8	668.4325	-0.64916	3.5624	3.7666	5.734
2	200	400	25	No Separator	672.8	662.4871	-1.53284	3.5624	3.6103	1.34567
3	250	450	30	No Separator	672.8	666.5874	-0.92339	3.5624	3.8805	8.932
4	250	400	30	Straight Separator	672.8	670.5697	-0.33149	3.5624	3.7167	4.332597
5	200	400	25	Straight Separator	672.8	670.4766	-0.34533	3.5624	3.8283	7.465267
6	250	400	30	Straight Separator	672.8	669.7162	-0.45835	3.5624	3.7620	5.604567
7	250	400	30	Modified Separator	672.8	671.375	-0.2118	3.5624	3.7286	4.666667
8	200	400	25	Modified Separator	672.8	667.8322	-0.73837	3.5624	3.7001	3.866667
9	250	450	30	Modified Separator	672.8	670.8658	-0.28749	3.5624	3.8220	7.288317

Table 6.1: **Estimated system components price and operating cost**

Description	Cost (RM)
Initial costs	
Turbine generator (2 unites including inverter and controller)	11,000.00
Batteries	2,000.00
Diffuser, separator plates and supporting structure	3,000.00
Total capital price	**16,000.00**
Operation costs	
Batteries (every 5 years)	1,000.00
Inverter (every 10 years)	2,000.00
Controller (every 10 years)	1,500.00
Estimated annual operation and maintenance cost	1,000.00

The cooling towers for commercial buildings commonly operate for long-hours per day. For the economic assessment, the cooling towers are assumed to be installed at commercial areas (i.e. shopping malls, hospitals, etc.) in Peninsular Malaysia using low voltage commercial tariff operating for 20 h daily and 30 days in a month. The commercial tariff of electricity provided by the utility provider is 43.5 sen/kWh ("Low Voltage Commercial Tarrif," 2015). According to the electricity price trend, tariff rate is predicted to rise by 10% annually (Chong et al., 2011). Apart from that, inflation rate for components replacement cost and operation and maintenance cost is taken into account which will increase by of 3.75% yearly as reported by the Department of Statistics Malaysia ("Malaysia Inflation Rate," 2016). To determine the present value *(PV)* of income for N^{th} period (usually year) in the future, the following equation is used,

$$PV = \frac{1}{(1+i)^N} \tag{6.1}$$

where i represents the estimated annual inflation rate. *PV* is used to return the value of the future payments or incomes on a given period to present value (Newnan et al., 2004). Then, the net present value (*NPV*) is calculated to obtain the sum of the present values of the individual cash flow. The economic parameters for the exhaust air energy recovery turbine generator system assessment are tabulated in Table 6.2.

Table 6.2: Economic Parameter

Economic Parameter	Value	Reference
Electricity price (per kWh)	RM 0.435	("Low Voltage Commercial Tarrif," 2015)
Annual electricity price increment	10%	(Chong et al., 2011)
Inflation rate of inverter price	3.75%	("Malaysia Inflation Rate," 2016)
Inflation rate of battery price	3.75%	
Inflation rate of controller price	3.75%	
Inflation rate of operation and maintenance cost	3.75%	

As mentioned in the design description section, an exhaust air energy recovery wind turbine generator system can consist of more than one wind turbine. Based on the outlet area of the cooling tower and the size of the turbine used in this experiment, it is possible to place two turbines. Considering the best turbine position as suggested in the previous chapters (Y = 400 mm and X = 250 mm), and the cooling tower performance remains the same as in this configuration, if two wind turbines are in place, the system doubles the energy recovery percentage. Measurement on an actual cooling tower with 2.4 m diameter and powered by a 7.5 kW fan motor revealed that the discharge wind velocity is about 13 m/s. Matching to the size of the cooling tower outlet, two units of 500 W VAWT can be placed to recover the energy. Since the discharge speed is approximately the same as the turbine's rated speed, 1 kW power is expected to be generated by both turbines, which is equivalent to 13% of energy recovery (Fazlizan et al., 2015).

The economic analysis is done with the consideration of operation cost and energy generated by the system based on a 20-year life cycle analysis. This is because according to ASHRAE (2013), the life expectancy of a cooling tower to work in acceptable efficiency is 20 years. An optimized exhaust air energy recovery turbine generator is considered to generate 13% of discharged energy. The initial capital required for the entire system is RM 16,000, which consists of two units of wind

turbines, inverter, diffuser plates and supporting structure. The life cycle analysis is illustrated in Figure 6.1. It is observed that the designed system has a payback period of 8 years with net present value of RM 2,126. Even though some components need to be replaced every 5 years the earnings from the energy savings will be able to compensate the replacement cost of the breakeven year. The net present value of the system at the end of the life cycle of the analysis is RM 30,347. The cumulative recovered energy value at the end of the life cycle of the system is RM 178,709 (Figure 6.2).

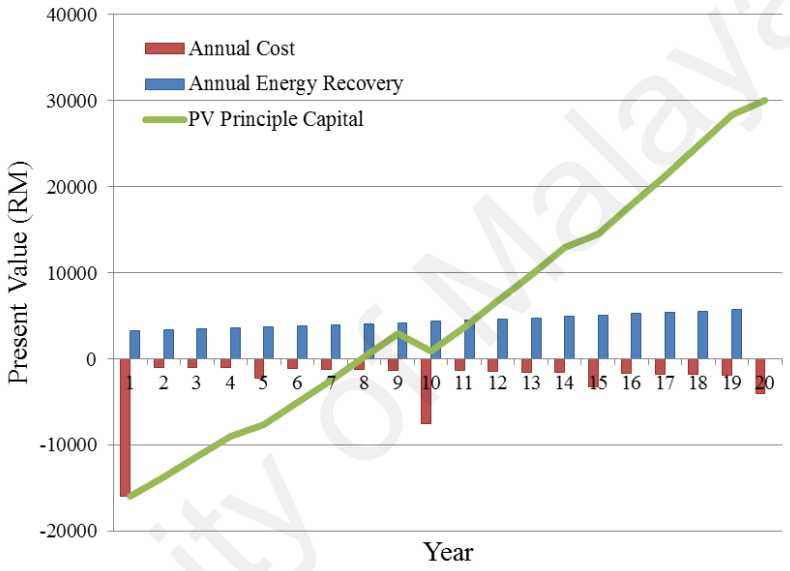

Figure 6.1 Cost analysis of the exhaust air energy recovery (20 years life cycle)

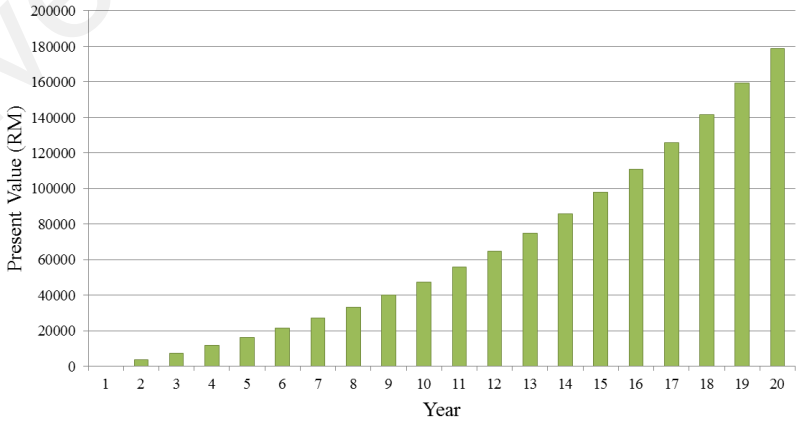

Figure 6.2 Cumulative value of recovered energy

6.3 Summary

In this chapter, a techno-economic analysis has been carried out on the novel exhaust air energy recovery wind turbine generator installed on a cooling tower commonly used

in Malaysia. For the cooling tower with a 7.5 kW rated fan motor, 13% of the discharged energy is expected to be recovered. For a year of operation of the cooling tower with this system, approximately 7,300 kWh is estimated to be recovered. Economic analysis shows that capital, components replacement, and operation and maintenance costs of the system are covered in the lifetime of the system. For this project, the NPV is RM 30,347 for the 20-years lifetime.

CHAPTER 7: CONCLUSION AND RECOMMENDATIONS FOR FURTHER STUDIES

7.1 Findings and Contribution

This research has focused on an exhaust air energy recovery wind turbine and analysed the aerodynamic performance of this wind turbine. In this research, a novel wind turbine has been specifically designed to harvest the energy from cooling tower exhaust airflow. The performance of the novel wind turbine has been analysed using CFD simulation and experimentation. The findings of this thesis can be drawn as follows:

The diffuser plates are critical part of the novel wind turbine. They are not only designed to achieve higher integration with urban environments and better safety, but also to concentrate wind energy. The wind energy is proportional to the flow area and cube of the flow velocity. Thus, increasing flow area or accelerating flow can improve the concentration of wind energy. In this thesis, introducing two diffuser plates and guide vanes to the base design showed a promising result in terms of power output improvement. The optimum angles for the diffusers plats, guide vanes A and B were found to be 7º, 70º and 60º respectively. The results of computational and experimental studies showed that adding the wind concentrating devices could enhance the wind turbine power coefficient by 34%.

The geometry of the diffuser plates was then optimised in order to improve the wind energy concentration. Different geometries of the diffusers were created and investigated in CFD simulations. Then the results were analysed using Design of Experiment method. The flow area has been modified and flow acceleration factor has been improved. The energy concentration of the diffusers has been significantly improved.

Since the wind from the discharge outlet generated by fan is not uniform in profile. Thus, the VAWT behaviour is different depending on its position in the non-uniform wind stream. From the computational studies, it was found out that the highest power can be obtained from the wind turbine when the rotor is installed at *X=250 mm* and *Y=400 mm*.

A separator plate was inserted at the mid-plane between two rotors to not only halt the interaction between two VAWTs but also to assist the wind concentration. A comprehensive computational study was carried out to investigate the effect of the diffuser plates and then the results were optimized using Design Expert software. Although, a better performance was achieved in presence of the separator plate, a higher power was obtained when the separator shape was modified. A comprehensive computational study was carried out to investigate the effect of the diffuser plates and then the results were optimized using Design Expert software.

Accurate prediction equations were presented and validated using computational and experimental cases. These equations are able to save considerable amount of time and cost for further studies.

The technical feasibility of the proposed design was assessed. It was shown that installing the exhaust air recovery system on the top of the cooling tower has neither negative impact on the fan motor consumption nor on the fan intake airflow.

In terms of economic feasibility, it was estimated that 13% of the energy from a common cooling tower with the outlet size of 2.4 m and rated motor consumption of 7.5 kW can be recovered. For the cooling tower that operates for 20 hours per day, every day throughout the year, a sum of 7,300 kWh/year is expected to be recovered. Life cycle assessment for 20-year life span, which takes into account full range of costs, showed that the payback period for the system of this size is 8 years. The net present value of the system at the end of the life cycle of the analysis is RM 25,347. The

cumulative recovered energy value at the end of the life cycle of the system is RM 179,786.

7.2 Recommendations

The methodology and results presented in this thesis could be used to address several other aspects in future works. Some of the recommendations are listed below:

- Another type of VAWTs can be used to maximise the exhaust air recovery. Based on the literatures, double-axis wind turbines are a suitable alternative.
- The effect of different airfoil profiles on the wind turbine performance can be investigated.
- Instead of using simple rectangular guide vanes, curved or airfoil profiles can be used.
- The interaction of the cooling tower and the exhaust air recovery system can be studied by performing a three-dimensional simulation.

REFERENCES

Abe, K., Nishida, M., Sakurai, A., Ohya, Y., Kihara, H., Wada, E., & Sato, K. (2005). Experimental and numerical investigations of flow fields behind a small wind turbine with a flanged diffuser. *Journal of Wind Engineering and Industrial Aerodynamics, 93*(12), 951-970.

Abohela, I., Hamza, N., & Dudek, S. (2013). Effect of roof shape, wind direction, building height and urban configuration on the energy yield and positioning of roof mounted wind turbines. *Renewable Energy, 50*, 1106-1118.

Akwa, J. V., Vielmo, H. A., & Petry, A. P. (2012). A review on the performance of Savonius wind turbines. *Renewable and Sustainable Energy Reviews, 16*(5), 3054-3064.

Almohammadi, K., Ingham, D., Ma, L., & Pourkashanian, M. (2012). CFD sensitivity analysis of a straight-blade vertical axis wind turbine. *Wind Engineering, 36*(5), 571-588.

Almohammadi, K. M., Ingham, D. B., Ma, L., & Pourkashan, M. (2013). Computational fluid dynamics (CFD) mesh independency techniques for a straight blade vertical axis wind turbine. *Energy, 58*(0), 483-493.

Anderson, D., Whale, J., Livingston, P., & Chan, D. (2008). *Rooftop wind resource assessment using a Three-Dimension Ultrasonic Anemometer*.

Araujo, P. W., & Brereton, R. G. (1996). Experimental design II. Optimization. *TrAC - Trends in Analytical Chemistry, 15*(2), 63-70.

ASHRAE. (2013). *ASHRAE Equipment Life Expectancy chart: American Society of Heating*: Refrigerating and Air Conditioning Engineers, Atlanta.

Baik, J.-J., Park, R.-S., Chun, H.-Y., & Kim, J.-J. (2000). A laboratory model of urban street-canyon flows. *Journal of applied meteorology, 39*(9), 1592-1600.

Berenda, R. M., & Ferenci, J. (1996). U.S. Patent No. 5,512,788. Washington, DC: U.S. Patent and Trademark Office.

Bet, F., & Grassmann, H. (2003). Upgrading conventional wind turbines. *Renewable Energy, 28*(1), 71-78.

Bezerra, M. A., Santelli, R. E., Oliveira, E. P., Villar, L. S., & Escaleira, L. A. (2008). Response surface methodology (RSM) as a tool for optimization in analytical chemistry. *Talanta*, *76*(5), 965-977.

Booker, A. J. (1998). Design and analysis of computer experiments. *AIAA paper*(1998-4757).

Box, G. E., & Behnken, D. W. (1960). Some new three level designs for the study of quantitative variables. *Technometrics*, *2*(4), 455-475.

Box, G. E., & Wilson, K. (1951). On the experimental attainment of optimum conditions. *Journal of the Royal Statistical Society. Series B (Methodological)*, *13*(1), 1-45.

Câmara, C. A. P., Bortoloti, J., Scarminio, I. S., Ballus, C. A., Meinhart, A. D., Godoy, H. T., & Bruns, R. E. (2013). Optimization of electrophoretic separations of thirteen phenolic compounds using single peak responses and an interactive computer technique. *Journal of the Brazilian Chemical Society*, *24*, 1744-1753.

Campbell, N., Stankovic, S., Graham, M., Parkin, P., van Duijvendijk, M., de Gruiter, T., Behling, S., Hieber, J. & Blanch, M. (2001). *Wind energy for the built environment (Project WEB)*. Paper presented at the European Wind Energy Conference & Exhibition, Copenhagen.

Carlin, P. W., Laxson, A. S., & Muljadi, E. (2003). The history and state of the art of variable-speed wind turbine technology. *Wind Energy*, *6*(2), 129-159.

Chen, V. C., Tsui, K.-L., Barton, R. R., & Meckesheimer, M. (2006). A review on design, modeling and applications of computer experiments. *IIE transactions*, *38*(4), 273-291.

Chong, W., Naghavi, M., Poh, S., Mahlia, T., & Pan, K. (2011). Techno-economic analysis of a wind–solar hybrid renewable energy system with rainwater collection feature for urban high-rise application. *Applied Energy*, *88*(11), 4067-4077.

Chong, W. T., Chew, P. S., Fazlizan, A., Sean, O. C., & Ching, T. C. (2011). *Exhaust air and wind energy recovery system for clean energy generation.* Paper presented at the International conference on environment and industrial innovation. Kuala Lumpur: IACSIT Press.

Chong, W. T., Fazlizan, A., Poh, S. C., Pan, K. C., Hew, W. P., & Hsiao, F. B. (2013). The design, simulation and testing of an urban vertical axis wind turbine with the omni-direction-guide-vane. *Applied Energy*, *112*(0), 601-609.

Chong, W. T., Hew, W. P., Yip, S. Y., Fazlizan, A., Poh, S. C., Tan, C. J., & Ong, H. C. (2014). The experimental study on the wind turbine's guide-vanes and diffuser of an exhaust air energy recovery system integrated with the cooling tower. *Energy Conversion and Management, 87*, 145-155.

Chong, W. T., Kong, Y. Y., & Fazlizan, A. (2013). Wind and Exhaust Air Energy Recovery System. WO2013073930 A1, 16.

Chong, W. T., Pan, K. C., Poh, S. C., Fazlizan, A., Oon, C. S., Badarudin, A., & Nik-Ghazali, N. (2013). Performance investigation of a power augmented vertical axis wind turbine for urban high-rise application. *Renewable Energy, 51*(0), 388-397.

Chowdhury, A. M., Akimoto, H., & Hara, Y. (2016). Comparative CFD analysis of vertical axis wind turbine in upright and tilted configuration. *Renewable Energy, 85*, 327-337.

Cohen, L. J. (2002). U.S. Patent No. 6,365,985. Washington, DC: U.S. Patent and Trademark Office.

Commission, E. (2014). Malaysia energy statistics handbook 2014.

Daly, B. (1978). *Woods practical guide to fan engineering*: Woods of Colchester Limited.

Dannecker, R. K., & Grant, A. D. (2002). Investigations of a building-integrated ducted wind turbine module. *Wind Energy, 5*(1), 53-71.

Dayan, E. (2006). Wind energy in buildings: Power generation from wind in the urban environment - where it is needed most. *Refocus, 7*(2), 33-38.

de Carmoy, G. (1978). The USA faces the energy challenge. *Energy Policy, 6*(1), 36-52.

Eriksson, S., Bernhoff, H., & Leijon, M. (2008). Evaluation of different turbine concepts for wind power. *Renewable and Sustainable Energy Reviews, 12*(5), 1419-1434.

Fang, K.-T., Lin, D. K., Winker, P., & Zhang, Y. (2000). Uniform design: theory and application. *Technometrics, 42*(3), 237-248.

Fazlizan, A. (2016). *Design and testing of a novel exhaust air energy recovery wind turbIine generator*. (Doctoral dissertation, University of Malaysia).

Fazlizan, A., Chong, W., Yip, S., Hew, W., & Poh, S. (2015). Design and Experimental Analysis of an Exhaust Air Energy Recovery Wind Turbine Generator. *Energies, 8*(7), 6566.

Ferziger, J. H., & Peric, M. (2012). *Computational methods for fluid dynamics*: Springer Science & Business Media.

Fleming, P. D., & Probert, S. D. (1984). The evolution of wind-turbines: An historical review. *Applied Energy, 18*(3), 163-177.

Fluent, A. (2009). 12.0 Theory Guide. *Ansys Inc, 5*.

Fluent, A. (2012). 14.5 User's Guide. *Fluent Inc.*

Foreman, K. (1981). Preliminary design and economic investigations of Diffuser-Augmented Wind Turbines (DAWT): Grumman Aerospace Corp., Bethpage, NY (USA). Research Dept.

Foreman, K., & Gilbert, B. (1979). Technical development of the Diffuser Augmented Wind Turbine/DAWT/concept. *Wind Engineering, 3*, 153-166.

Foreman, K., Gilbert, B., & Oman, R. (1978). Diffuser augmentation of wind turbines. *Solar Energy, 20*(4), 305-311.

Fujisawa, N. (1992). On the torque mechanism of Savonius rotors. *Journal of Wind Engineering and Industrial Aerodynamics, 40*(3), 277-292.

Ghosh, T. K., & Prelas, M. A. (2011) *Energy Resources and Systems: Volume 2: Renewable Resources (Vol. 2)* (pp. 1-77). Dordrecht: Springer Netherlands.

Gilbert, B., Oman, R., & Foreman, K. (1978). Fluid dynamics of diffuser-augmented wind turbines. *Journal of Energy, 2*(6), 368-374.

Göçmen, T., & Özerdem, B. (2012). Airfoil optimization for noise emission problem and aerodynamic performance criterion on small scale wind turbines. *Energy, 46*(1), 62-71.

Gorelov, D. N., & Krivospitsky, V. P. (2008). Prospects for development of wind turbines with orthogonal rotor. *Thermophysics and Aeromechanics, 15*(1), 153-157.

Grant, A., Johnstone, C., & Kelly, N. (2008). Urban wind energy conversion: The potential of ducted turbines. *Renewable Energy, 33*(6), 1157-1163.

Grant, A., & Kelly, N. (2003). Development of a ducted wind energy converter. *Wind Engineering, 18*(6), 297-304.

Grimmond, C. S. B., & Oke, T. R. (1999). Aerodynamic Properties of Urban Areas Derived from Analysis of Surface Form. *Journal of applied meteorology, 38*(9), 1262-1292.

Gunnell, D., Platt, S., & Hawton, K. (2009). The economic crisis and suicide. *BMJ, 338*.

Hafez, O., & Bhattacharya, K. (2012). Optimal planning and design of a renewable energy based supply system for microgrids. *Renewable Energy, 45*, 7-15.

Hansen, M. O. (2015). *Aerodynamics of wind turbines*: Routledge.

Hau, E. (2013). *Wind turbines: fundamentals, technologies, application, economics.*

Hedayat, A. S., Sloane, N. J. A., & Stufken, J. (1999). *Orthogonal arrays: theory and applications*. Springer Science & Business Media.

Herrman, D. (1962). *Field tests of fan performance on induced draft cooling towers*: Cooling Tower Inst., CTI.

Howell, R., Qin, N., Edwards, J., & Durrani, N. (2010). Wind tunnel and numerical study of a small vertical axis wind turbine. *Renewable Energy, 35*(2), 412-422.

Igra, O. (1981). Research and development for shrouded wind turbines. *Energy Conversion and Management, 21*(1), 13-48.

Islam, M., Mekhilef, S., & Saidur, R. (2013). Progress and recent trends of wind energy technology. *Renewable and Sustainable Energy Reviews, 21*, 456-468.

Islam, M., Ting, D. S. K., & Fartaj, A. (2008). Aerodynamic models for Darrieus-type straight-bladed vertical axis wind turbines. *Renewable and Sustainable Energy Reviews, 12*(4), 1087-1109.

Khan, S. (2011). U.S. Patent Application No. 12/584,038.

Kirke, B. K. (1998). *Evaluation of self-starting vertical axis wind turbines for stand-alone applications.* (Doctoral dissertation, Griffith University Gold Coast).

Kota, S., Bayne, S. B., & Nimmagadda, S. (2015). Offshore wind energy: A comparative analysis of UK, USA and India. *Renewable and Sustainable Energy Reviews, 41*, 685-694.

Kyozuka, Y. (2008). An experimental study on the Darrieus-Savonius turbine for the tidal current power generation. *Journal of Fluid Science and Technology, 3*(3), 439-449.

Laratro, A., Arjomandi, M., Cazzolato, B., & Kelso, R. (2016). A Comparison of NACA 0012 and NACA 0021 Self-noise at Low Reynolds Number *Fluid-Structure-Sound Interactions and Control* (pp. 21-25): Springer.

Ledo, L., Kosasih, P. B., & Cooper, P. (2011). Roof mounting site analysis for micro-wind turbines. *Renewable Energy, 36*(5), 1379-1391.

Lilley, G., & Rainbird, W. (1956). A preliminary report on the design and performance of ducted windmills. College of Aeronautics Cranfield.

Low Voltage Commercial Tarrif. (2015). Retrieved August, 2015, from https://www.tnb.com.my/commercial-industrial/pricing-tariffs1

Makkawi, A., Celik, A., & Muneer, T. (2009). Evaluation of micro-wind turbine aerodynamics, wind speed sampling interval and its spatial variation. *Building Services Engineering Research and Technology, 30*(1), 7-14.

Malaysia Inflation Rate. (2016). Retrieved January, 2016, from http://www.tradingeconomics.com/malaysia/inflation-cpi

Manwell, J. F., McGowan, J. G., & Rogers, A. L. (2010). *Wind energy explained: theory, design and application.* John Wiley & Sons.

McTavish, S., Feszty, D., & Sankar, T. (2012). Steady and rotating computational fluid dynamics simulations of a novel vertical axis wind turbine for small-scale power generation. *Renewable Energy, 41*, 171-179.

Menet, J. L. (2004). A double-step Savonius rotor for local production of electricity: a design study. *Renewable Energy, 29*(11), 1843-1862.

Mertens, S. (2002). Wind energy in urban areas: Concentrator effects for wind turbines close to buildings. *Refocus, 3*(2), 22-24.

Mertens, S., van Kuik, G., & van Bussel, G. (2003). Performance of an H-Darrieus in the skewed flow on a roof. *Journal of Solar Energy Engineering, 125*(4), 433-440.

Miller, R. L. (1988). Islamic technology: an illustrated history. *Medical History, 32*(4), 466-467.

Millward-Hopkins, J., Tomlin, A., Ma, L., Ingham, D., & Pourkashanian, M. (2013). Assessing the potential of urban wind energy in a major UK city using an analytical model. *Renewable Energy, 60*, 701-710.

Mittal, R., Sandhu, K., & Jain, D. (2010). An overview of some important issues related to wind energy conversion system (WECS). *International Journal of Environmental Science and Development, 1*(4), 351.

Moeller, M., & Visser, K. (2010). *Experimental and Numerical Studies of a High Solidity, Low Tip Speed Ratio DAWT*, In Proceedings of the 48th AIAA Aerospace Sciences Meeting and Exhibit, Orlando, FL, USA (pp. 4-7).

Müller, G., Jentsch, M. F., & Stoddart, E. (2009). Vertical axis resistance type wind turbines for use in buildings. *Renewable Energy, 34*(5), 1407-1412.

Murakami, S., & Mochida, A. (1988). 3-D numerical simulation of airflow around a cubic model by means of the k-ϵ model. *Journal of Wind Engineering and Industrial Aerodynamics, 31*(2), 283-303.

Myers, R. H., & Montgomery, D. (1995). *Response surface methodology: process and product optimization using designed experiments*: John Wiley & Sons.

Myers, R. H., Montgomery, D. C., & Anderson-Cook, C. M. (1995). *Response surface methodology: process and product optimization using designed experiments*: John Wiley & Sons.

Narayanan, S., Chaitanya, P., Haeri, S., Joseph, P., Kim, J., & Polacsek, C. (2015). Airfoil noise reductions through leading edge serrations. *Physics of Fluids (1994-present), 27*(2), 025109.

Newnan, D. G., Eschenbach, T., & Lavelle, J. P. (2004). *Engineering economic analysis* (Vol. 2). Oxford University Press.

Ohya, Y., & Karasudani, T. (2010). A shrouded wind turbine generating high output power with wind-lens technology. *Energies, 3*(4), 634-649.

Ohya, Y., Karasudani, T., Sakurai, A., Abe, K.-i., & Inoue, M. (2008). Development of a shrouded wind turbine with a flanged diffuser. *Journal of Wind Engineering and Industrial Aerodynamics, 96*(5), 524-539.

Paraschivoiu, I. (2002). *Wind turbine design: with emphasis on Darrieus concept*. Presses inter Polytechnique.

Plackett, R. L., & Burman, J. P. (1946). The design of optimum multifactorial experiments. *Biometrika, 33*(4), 305-325.

Pope, K., Rodrigues, V., Doyle, R., Tsopelas, A., Gravelsins, R., Naterer, G. F., & Tsang, E. (2010). Effects of stator vanes on power coefficients of a zephyr vertical axis wind turbine. *Renewable Energy, 35*(5), 1043-1051.

Qin, N., Howell, R., Durrani, N., Hamada, K., & Smith, T. (2011). Unsteady flow simulation and dynamic stall behaviour of vertical axis wind turbine blades. *Wind Engineering, 35*(4), 511-528.

Queipo, N. V., Haftka, R. T., Shyy, W., Goel, T., Vaidyanathan, R., & Tucker, P. K. (2005). Surrogate-based analysis and optimization. *Progress in aerospace sciences, 41*(1), 1-28.

Rao, C. R. (1947). Factorial experiments derivable from combinatorial arrangements of arrays. *Supplement to the Journal of the Royal Statistical Society, 9*(1), 128-139.

Rocha, P. A. C., Rocha, H. H. B., Carneiro, F. O. M., Vieira da Silva, M. E., & Bueno, A. V. (2014). k–ω SST (shear stress transport) turbulence model calibration: A case study on a small scale horizontal axis wind turbine. *Energy, 65*(0), 412-418.

Sacks, J., Welch, W. J., Mitchell, T. J., & Wynn, H. P. (1989). Design and analysis of computer experiments. *Statistical science*, 409-423.

Schaffarczyk, A. P. (2014). *Introduction to wind turbine aerodynamics*. Springer.

Shahizare, B., Nazri Bin Nik Ghazali, N., Chong, W. T., Tabatabaeikia, S., & Izadyar, N. (2016a). Investigation of the Optimal Omni-Direction-Guide-Vane Design for Vertical Axis Wind Turbines Based on Unsteady Flow CFD Simulation. *Energies, 9*(3), 146.

Shahizare, B., Nazri Bin Nik Ghazali, N., Chong, W. T., Tabatabaeikia, S., Izadyar, N., & Esmaeilzadeh, A. (2016b). Novel investigation of the different Omni-direction-guide-vane angles effects on the urban vertical axis wind turbine

output power via three-dimensional numerical simulation. *Energy Conversion and Management, 117*, 206-217.

Sharpe, T., & Proven, G. (2010). Crossflex: Concept and early development of a true building integrated wind turbine. *Energy and Buildings, 42*(12), 2365-2375.

Simms, D. A., Schreck, S., Hand, M., & Fingersh, L. (2001). *NREL unsteady aerodynamics experiment in the NASA-Ames wind tunnel: a comparison of predictions to measurements*. National Renewable Energy Laboratory, Golden, CO, Report No. NREL/TP-500-29494.

Simpson, T. W., Lin, D. K., & Chen, W. (2001). Sampling strategies for computer experiments: design and analysis. *International Journal of Reliability and Applications, 2*(3), 209-240.

Simpson, T. W., Peplinski, J., Koch, P. N., & Allen, J. K. (1997). On the use of statistics in design and the implications for deterministic computer experiments. *Design Theory and Methodology-DTM'97*, 14-17.

Spera, D. A. (2009). *Wind turbine technology: fundamental concepts of wind turbine technology*.

Sung, C. (2013). Possibility of electricity from wind energy in Malaysia: some rough calculations.

Syngellakis, K., Carroll, S., & Robinson, P. (2006). Small wind power: Introduction to urban small scale wind in the UK. *Refocus, 7*(2), 40-45.

Tan, C. J., Chong, W. T., & Hassan, M. A. (2013). End formation of a round tube into a square section having small corner radii. *Journal of Materials Processing Technology, 213*(9), 1465-1474.

Thomas, R. L., & Robbins, W. H. (1980). Wind Energy Conversion SystemsLarge wind-turbine projects in the United States wind energy program. *Journal of Wind Engineering and Industrial Aerodynamics, 5*(3), 323-335.

Van Bussel, G., & Mertens, S. (2005). *Small wind turbines for the built environment*. In Proceedings of the 4th European and African conference on wind engineering.

Van Bussel, G. J. (2007). *The science of making more torque from wind: Diffuser experiments and theory revisited*, In Journal of Physics: Conference Series (Vol. 75, No. 1, p. 012010). IOP Publishing.

Vries, O. D. (1983). On the Theory of the Horizontal-Axis Wind Turbine. *Annual Review of Fluid Mechanics, 15*(1), 77-96.

Walker, S. L. (2011). Building mounted wind turbines and their suitability for the urban scale—A review of methods of estimating urban wind resource. *Energy and Buildings, 43*(8), 1852-1862.

Webster, G. W. (1979). U.S. Patent No. 4,154,556. Washington, DC: U.S. Patent and Trademark Office.

Williams, M. C., Strakey, J. P., & Surdoval, W. A. (2005). The U.S. Department of Energy, Office of Fossil Energy Stationary Fuel Cell Program. *Journal of Power Sources, 143*(1–2), 191-196.

Wood. (2004). Dual Purpose Design of Small Wind Turbine Blades. *Wind Engineering, 28*(5), 511-527.

Yakhot, V., Orszag, S., Thangam, S., Gatski, T., & Speziale, C. (1992). Development of turbulence models for shear flows by a double expansion technique. *Physics of Fluids A: Fluid Dynamics (1989-1993), 4*(7), 1510-1520.

Yang, A.-S., Su, Y.-M., Wen, C.-Y., Juan, Y.-H., Wang, W.-S., & Cheng, C.-H. (2016). Estimation of wind power generation in dense urban area. *Applied Energy, 171*, 213-230.

Zhang, X. (2014). *Analysis and optimisation of a novel wind turbine.* (Doctoral dissertation, University of Hertfordshire).

LIST OF PUBLICATIONS: JOURNAL PAPERS

1. Tabatabaeikia, S., Bin Nik-Ghazali, N. N., Chong, W. T., Shahizare, B., Fazlizan, A., Esmaeilzadeh, A., & Izadyar, N. (2016). A Comparative Computational Fluid Dynamics Study on an Innovative Exhaust Air Energy Recovery Wind Turbine Generator. *Energies, 9*(5), 346.

2. Seyedsaeed Tabatabaeikia, Nik Nazri Bin Nik Ghazali, Chong Wen Tong, Behzad Shahizare, Nima Izadyar, Alireza Esmaeilzadeh and Ahmad Fazlizan (2016). Computational and Experimental Optimization of a Novel Exhaust Air Energy Recovery Wind Turbine Generator. *Eenergy conservation and management*

APPENDIX A

Appendix A: Sample of data collected by the dynamometer Data at 40% load from X = 150 mm, Y = 450 mm.

Time	RPM	Torque (Nm)	% Load	Current	Voltage	Electrical Power	Mechanical Power
666.791	148.3179	0.004259	40	0.024414	12.09677	0.118134	0.672771
667.793	146.659	0.004211	40	0.024738	12.5	0.12369	0.704416
668.789	144.3295	0.004178	40	0.022651	12.23118	0.11082	0.631118
669.79	142.6647	0.004154	40	0.02411	12.76882	0.12314	0.701282
670.782	140.3324	0.004138	40	0.024103	11.69355	0.112741	0.64206
671.782	138.1662	0.004127	40	0.02488	11.82796	0.117713	0.670376
672.783	136.5831	0.004119	40	0.024329	11.15591	0.108564	0.618273
673.767	135.7915	0.004113	40	0.023497	11.55914	0.108641	0.618708
674.769	133.8958	0.004109	40	0.023222	11.82796	0.109867	0.625695
675.77	132.4479	0.004106	40	0.024957	12.5	0.124786	0.710658
676.763	131.2239	0.004104	40	0.025954	10.75269	0.111632	0.635745
677.765	130.612	0.004103	40	0.025188	11.96237	0.120524	0.686385
678.765	131.306	0.004102	40	0.025748	11.55914	0.119051	0.677995
679.757	132.153	0.004102	40	0.025023	10.61828	0.106281	0.605272
680.758	131.5765	0.004101	40	0.022488	11.15591	0.10035	0.571496
681.743	130.7882	0.004101	40	0.022415	11.42473	0.102435	0.583367
682.744	130.3941	0.004101	40	0.022357	9.946237	0.088946	0.506549
683.744	130.1971	0.0041	40	0.022701	10.75269	0.097639	0.556054
684.747	128.5985	0.0041	40	0.023367	11.29032	0.105531	0.600997
685.732	127.2993	0.0041	40	0.023119	10.8871	0.100678	0.573361
686.733	127.6496	0.0041	40	0.022138	11.96237	0.105927	0.603253
687.733	128.3248	0.0041	40	0.022526	11.02151	0.099307	0.565551
688.734	127.6624	0.0041	40	0.021272	10.48387	0.089206	0.508027
689.719	126.8312	0.0041	40	0.021442	11.55914	0.099142	0.564614
690.72	125.9156	0.0041	40	0.021188	10.34946	0.087712	0.499518
691.72	125.4578	0.0041	40	0.021375	10.8871	0.093083	0.530108
692.713	126.2289	0.0041	40	0.021524	10.8871	0.093735	0.533821
693.713	127.1145	0.0041	40	0.021644	11.15591	0.096584	0.550045
694.714	126.5572	0.0041	40	0.022522	10.75269	0.096869	0.551666
695.714	125.7786	0.0041	40	0.022051	11.02151	0.097215	0.553639
696.705	123.8893	0.0041	40	0.022848	11.42473	0.104411	0.594621
697.705	122.4447	0.0041	40	0.023485	9.677419	0.090909	0.517724
698.7	122.7223	0.0041	40	0.022821	10.8871	0.099384	0.565989
699.688	123.3612	0.0041	40	0.022682	10.48387	0.095117	0.541691
700.687	122.6806	0.0041	40	0.022961	9.811828	0.090116	0.51321
701.692	121.8403	0.0041	40	0.02162	11.15591	0.096478	0.549444
702.692	122.4201	0.0041	40	0.022112	11.02151	0.097483	0.555166
703.677	123.2101	0.0041	40	0.022505	10.75269	0.096797	0.551257
704.677	123.605	0.0041	40	0.021647	10.48387	0.090777	0.516975

705.677	123.8025	0.0041	40	0.022133	11.42473	0.101146	0.576026
706.677	123.9013	0.0041	40	0.023304	11.55914	0.10775	0.613638
707.677	123.9506	0.0041	40	0.022677	11.29032	0.102412	0.583236
708.662	123.9753	0.0041	40	0.022175	10.75269	0.095377	0.543172
709.663	123.9877	0.0041	40	0.022556	10.8871	0.098227	0.559401
710.671	122.9938	0.0041	40	0.022078	11.55914	0.102082	0.581358
711.658	121.9969	0.0041	40	0.021696	10.34946	0.089818	0.511512
712.66	122.4985	0.0041	40	0.022564	10.21505	0.092195	0.525053
713.661	123.2492	0.0041	40	0.022476	11.55914	0.103919	0.591819
714.648	122.6246	0.0041	40	0.022014	9.811828	0.086399	0.492044
715.649	121.8123	0.0041	40	0.022818	9.946237	0.090781	0.516997
716.649	122.4062	0.0041	40	0.021897	11.82796	0.103598	0.589993
717.649	123.2031	0.0041	40	0.023115	11.29032	0.104391	0.594508
718.639	123.6015	0.0041	40	0.023699	10.75269	0.10193	0.580493
719.64	123.8008	0.0041	40	0.023384	10.8871	0.101832	0.579934
720.642	122.9004	0.0041	40	0.022741	10.34946	0.094141	0.536133
721.627	121.9502	0.0041	40	0.023008	10.75269	0.09896	0.563575
722.627	122.4751	0.0041	40	0.022049	11.82796	0.104318	0.594093
723.628	123.2375	0.0041	40	0.022455	10.75269	0.09658	0.550025
724.63	123.6188	0.0041	40	0.022389	10.21505	0.09148	0.52098
725.63	123.8094	0.0041	40	0.021553	11.55914	0.099656	0.56754
726.615	122.9047	0.0041	40	0.022058	10.75269	0.094875	0.540313
727.616	121.9523	0.0041	40	0.022853	10.48387	0.095837	0.54579
728.616	120.9762	0.0041	40	0.021925	10.34946	0.090766	0.516913
729.609	120.4881	0.0041	40	0.022356	9.677419	0.086539	0.492839
730.609	120.244	0.0041	40	0.021918	8.467742	0.07424	0.422794
731.608	120.122	0.0041	40	0.021959	9.811828	0.086184	0.49082
732.61	120.061	0.0041	40	0.022774	9.946237	0.090607	0.516005
733.594	120.0305	0.0041	40	0.023817	9.811828	0.093475	0.53234
734.594	118.5153	0.0041	40	0.023087	11.02151	0.101782	0.579649
735.594	117.2576	0.0041	40	0.022894	9.543011	0.087392	0.4977
736.597	117.6288	0.0041	40	0.023131	9.677419	0.08954	0.50993
737.597	118.3144	0.0041	40	0.022539	11.02151	0.099363	0.565875
738.583	118.6572	0.0041	40	0.022846	9.543011	0.08721	0.496659
739.583	118.8286	0.0041	40	0.022311	10.08065	0.089963	0.512339
740.583	118.9143	0.0041	40	0.022273	11.55914	0.102984	0.586494
741.583	118.9572	0.0041	40	0.022634	9.408602	0.085183	0.485115
742.569	118.9786	0.0041	40	0.021359	9.543011	0.081532	0.464323
743.575	118.9893	0.0041	40	0.021512	10.48387	0.090211	0.513752
744.576	120.4946	0.0041	40	0.022025	10.48387	0.092363	0.52601
745.561	121.7473	0.0041	40	0.022436	9.274194	0.083229	0.473991
746.562	121.3737	0.0041	40	0.021982	10.48387	0.092183	0.524985
747.562	120.6868	0.0041	40	0.021619	10.21505	0.088337	0.503081
748.562	120.3434	0.0041	40	0.022502	10.8871	0.097993	0.558072

APPENDIX B

Appendix B: Experimental apparatus and setup pictures

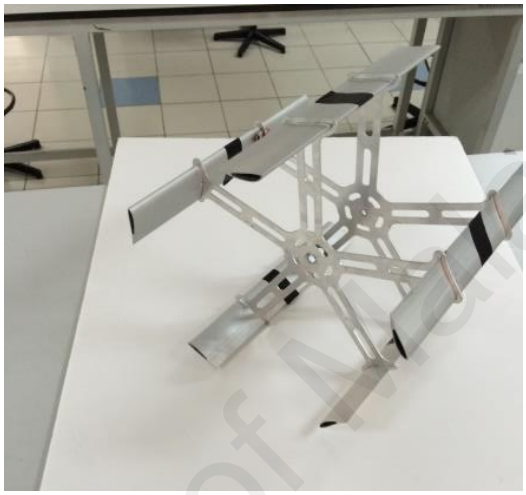

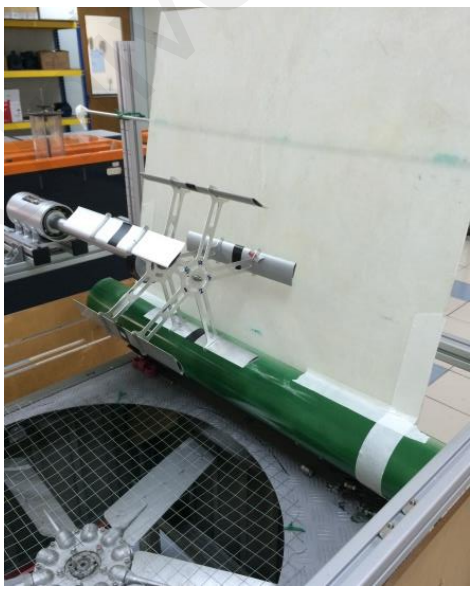

APPENDIX C

Appendix C: Design of Experiment cases.

		Factor 1	Factor 2	Factor 3	Factor 4
Std	Run	A:X mm	B:Y mm	C:Alpha degree	D:Separator Plate
1	53	150	400	0	No Separator
2	32	250	400	0	No Separator
3	12	150	500	0	No Separator
4	3	250	500	0	No Separator
5	24	150	400	45	No Separator
6	16	250	400	45	No Separator
7	34	150	500	45	No Separator
8	35	250	500	45	No Separator
9	31	150	450	22.5	No Separator
10	45	250	450	22.5	No Separator
11	51	200	400	22.5	No Separator
12	44	200	500	22.5	No Separator
13	29	200	450	0	No Separator
14	55	200	450	45	No Separator
15	21	200	450	22.5	No Separator
16	56	200	450	22.5	No Separator
17	48	200	450	22.5	No Separator
18	17	200	450	22.5	No Separator
19	42	200	450	22.5	No Separator
20	26	200	450	22.5	No Separator
21	28	150	400	0	Straight Separator
22	43	250	400	0	Straight Separator
23	30	150	500	0	Straight Separator
24	54	250	500	0	Straight Separator
25	25	150	400	45	Straight Separator
26	22	250	400	45	Straight Separator
27	27	150	500	45	Straight Separator
28	58	250	500	45	Straight Separator
29	18	150	450	22.5	Straight Separator
30	57	250	450	22.5	Straight Separator
31	14	200	400	22.5	Straight Separator

32	23	200	500	22.5	Straight Separator
33	41	200	450	0	Straight Separator
34	40	200	450	45	Straight Separator
35	50	200	450	22.5	Straight Separator
36	7	200	450	22.5	Straight Separator
37	59	200	450	22.5	Straight Separator
38	52	200	450	22.5	Straight Separator
39	8	200	450	22.5	Straight Separator
40	47	200	450	22.5	Straight Separator
41	39	150	400	0	Modified Separator
42	60	250	400	0	Modified Separator
43	1	150	500	0	Modified Separator
44	19	250	500	0	Modified Separator
45	6	150	400	45	Modified Separator
46	13	250	400	45	Modified Separator
47	36	150	500	45	Modified Separator
48	46	250	500	45	Modified Separator
49	49	150	450	22.5	Modified Separator
50	20	250	450	22.5	Modified Separator
51	15	200	400	22.5	Modified Separator
52	4	200	500	22.5	Modified Separator
53	33	200	450	0	Modified Separator
54	9	200	450	45	Modified Separator
55	38	200	450	22.5	Modified Separator
56	11	200	450	22.5	Modified Separator
57	2	200	450	22.5	Modified Separator
58	37	200	450	22.5	Modified Separator
59	5	200	450	22.5	Modified Separator
60	10	200	450	22.5	Modified Separator

APPENDIX D

Appendix D: Fluent parametric study table.

	A	B	C	D	E	F	G	H	I	J
1	Name	P5 - RPM	P6 - time step	P7 - GV1	P8 - Y	P9 - X	P4 - cm	Retain	Retained Data	Note
2	Units	radian s^-1	s	mm	mm	mm				
3	DP 0 (Current)	-27.359	0.00063793	66	450	229	0.002956	☑	✓	7
4	DP 1	-35.491	0.00049177	90	400	198	0.0070013	☑	✓	13
5	DP 2	-31.63	0.0005518	12.4	500	198	0.0060584	☑	✓	14
6	DP 3	-25.388	0.00068746	90	450	229	0.0026254	☑	✓	22
7	DP 4	-34.367	0.00050785	66	450	198	0.0066433	☑	✓	25
8	DP 5	-24.955	0.00069939	90	500	198	0.0030377	☑	✓	29
9	DP 6	-17.924	0.00097374	90	400	260	0.001079	☑	✓	30
10	DP 7	-19.46	0.00089688	66	500	229	0.0020297	☑	✓	33
11	DP 8	-33.921	0.00051453	12.4	400	198	0.0066842	☑	✓	37
12	DP 9	-16.005	0.0010905	12.4	500	260	0.0011279	☑	✓	41
13	DP 10	-20.227	0.00086288	12.4	400	260	0.0017962	☑	✓	48
14	DP 11	-15.054	0.0011593	66	450	260	0.00091739	☑	✓	52
15	DP 12	-27.41	0.00063675	12.4	450	229	0.0040735	☑	✓	54
16	DP 13	-26.818	0.00065082	66	400	229	0.0031744	☑	✓	55
17	DP 14	-15.687	0.0011126	90	500	260	0.00090602	☑	✓	57
*								☐		

	A	B	C	D	E	F	G	H	I	J
1	Name	P1 - GV1	P2 - X	P3 - Y	P5 - RPM	P6 - time step	P4 - cm	Retain	Retained Data	Note
2	Units	mm	mm	mm	radian s^-1	s				
3	DP 0 (Current)	12.4	198	400	-32.62	0.00053506	0.0065391	☑	✓	2
4	DP 1	66	229	450	-17.066	0.0010227	0.0018631	☑	✓	3
5	DP 2	12.4	198	500	-25.353	0.00068841	0.0052983	☑	✓	6
6	DP 3	12.4	260	400	-13.259	0.0013164	0.0012989	☑	✓	9
7	DP 5	12.4	260	500	-11.692	0.0014928	0.0014172	☑	✓	15
8	DP 6	66	229	400	-27.951	0.00062443	0.0032825	☑	✓	19
9	DP 9	90	229	450	-18.369	0.00095014	0.0015758	☑	✓	23
10	DP 10	12.4	229	450	-16.624	0.0010499	0.0018857	☑	✓	24
11	DP 11	90	198	400	-34.035	0.0005128	0.0070463	☑	✓	27
12	DP 12	90	198	500	-20.553	0.00084919	0.0026522	☑	✓	35
13	DP 13	66	198	450	-31.56	0.00055302	0.0053099	☑	✓	40
14	DP 14	66	229	500	-20.576	0.00084823	0.0020787	☑	✓	42
15	DP 15	66	260	450	-12.599	0.0013853	0.0015498	☑	✓	47
16	DP 16	90	260	500	-10.779	0.0016192	0.0011405	☑	✓	50
17	DP 17	90	260	400	-19.537	0.00089336	0.001594	☑	✓	51
*								☐		

	A	B	C	D	E	F	G	H
1	Name	P1 - GV1	P2 - X	P3 - Y	P4 - cm	Retain	Retained Data	Note
2	Units	mm	mm	mm				
3	DP 0 (Current)	12.4	198	400	0.006117	☑	✓	2
4	DP 1	66	229	450	0.0027752	☑	✓	3
5	DP 2	12.4	198	500	0.004986	☑	✓	6
6	DP 3	12.4	260	400	0.0029166	☑	✓	9
7	DP 5	12.4	260	500	0.0030012	☑	✓	15
8	DP 6	66	229	400	0.0028526	☑	✓	19
9	DP 9	90	229	450	0.0024306	☑	✓	23
10	DP 10	12.4	229	450	0.0042313	☑	✓	24
11	DP 11	90	198	400	0.0061604	☑	✓	27
12	DP 12	90	198	500	0.0029505	☑	✓	35
13	DP 13	66	198	450	0.0036846	☑	✓	40
14	DP 14	66	229	500	0.0029098	☑	✓	42
15	DP 15	66	260	450	0.0027252	☑	✓	47
16	DP 16	90	260	500	0.0024388	☑	✓	50
17	DP 17	90	260	400	0.0024975	☑	✓	51
*						☐		

APPENDIX E

Appendix E1: Torque coefficient vs azimuth angle obtained from CFD simulation for cases of "*Without Separator plate*"

X (mm)	200
Y (mm)	550
α (°)	45

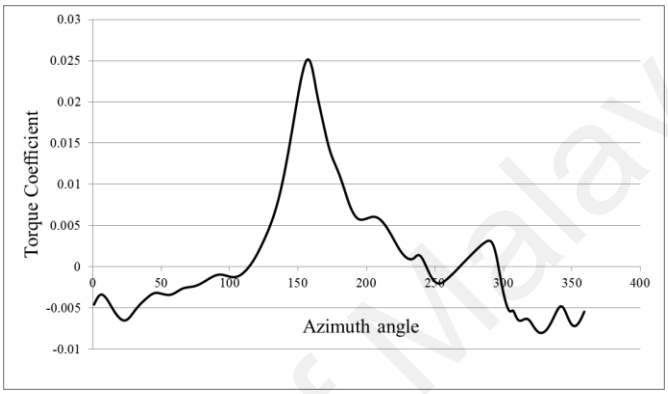

X (mm)	250
Y (mm)	500
α (°)	22.5

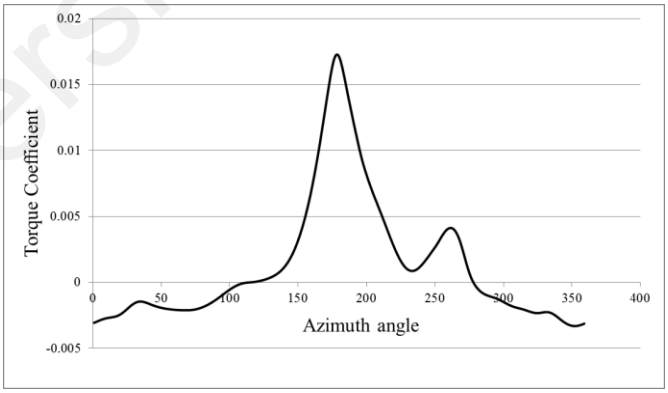

X (mm)	200
Y (mm)	500
α (°)	22.5

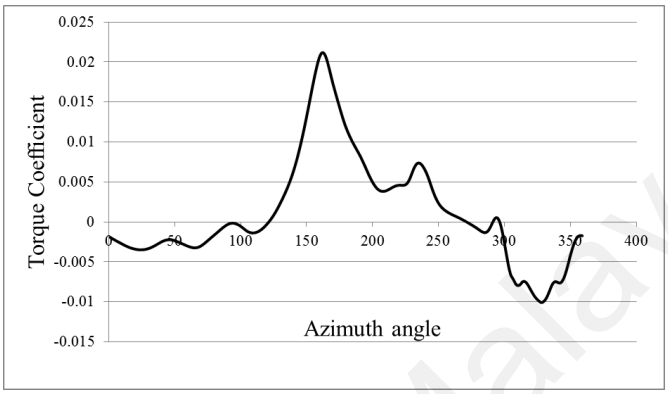

X (mm)	150
Y (mm)	550
α (°)	0

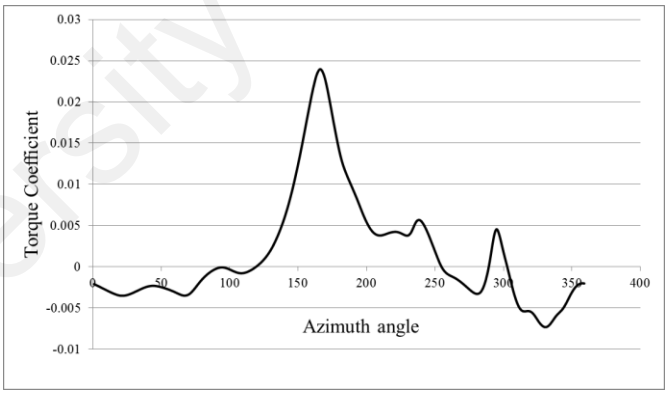

X (mm)	200
Y (mm)	450
α (°)	22.5

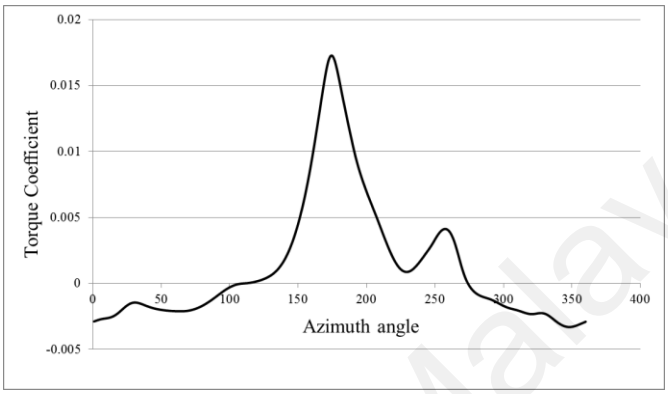

X (mm)	250
Y (mm)	450
α (°)	0

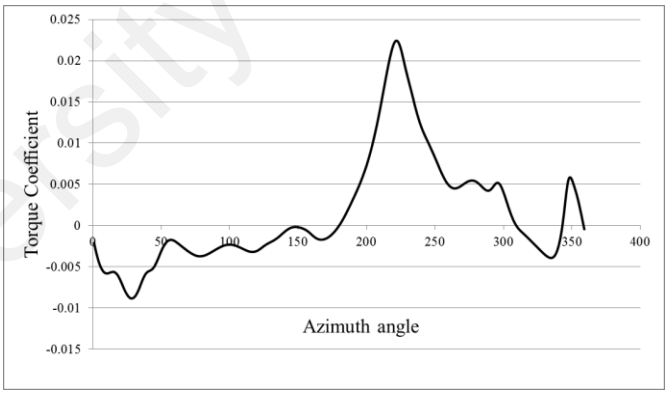

X (mm)	200
Y (mm)	500
α (°)	22.5

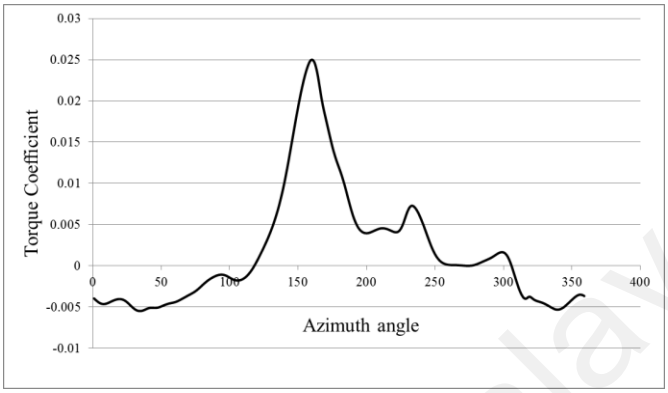

X (mm)	150
Y (mm)	550
α (°)	45

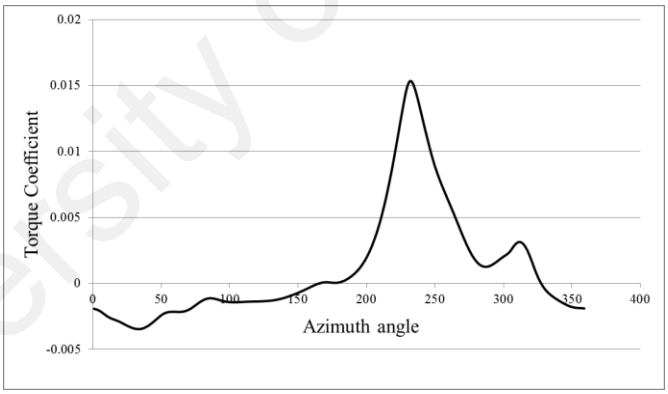

X (mm)	200
Y (mm)	500
α (°)	45

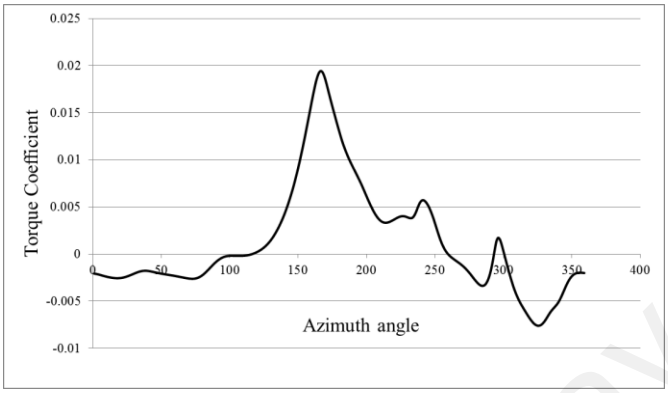

X (mm)	150
Y (mm)	500
α (°)	0

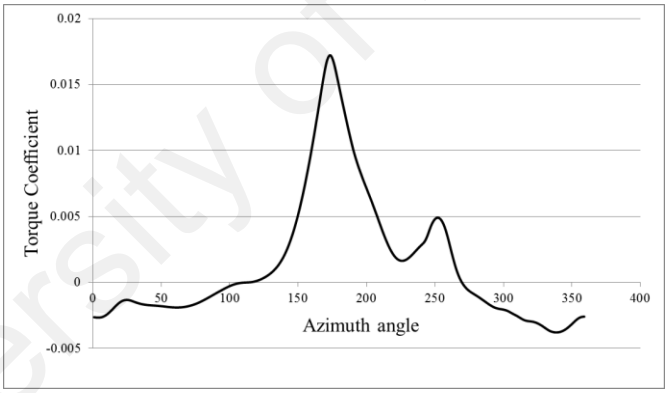

X (mm)	150
Y (mm)	450
α (°)	45

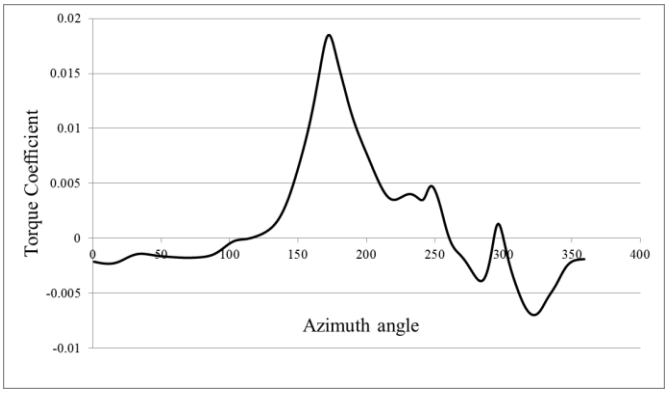

X (mm)	200
Y (mm)	500
α (°)	22.5

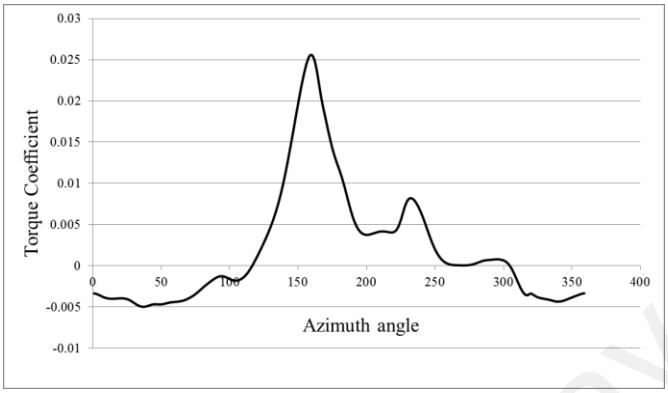

X (mm)	250
Y (mm)	550
α (°)	0

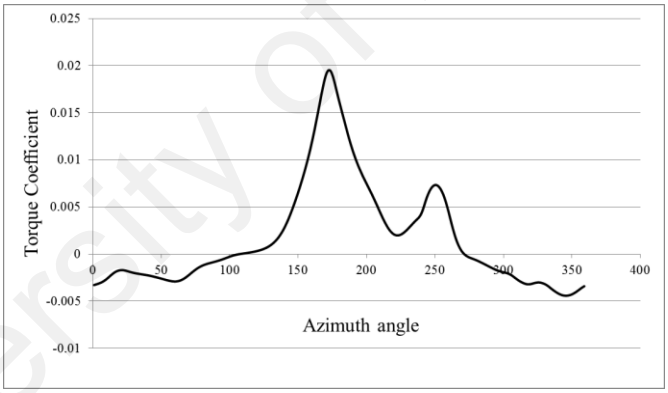

X (mm)	150
Y (mm)	500
α (°)	22.5

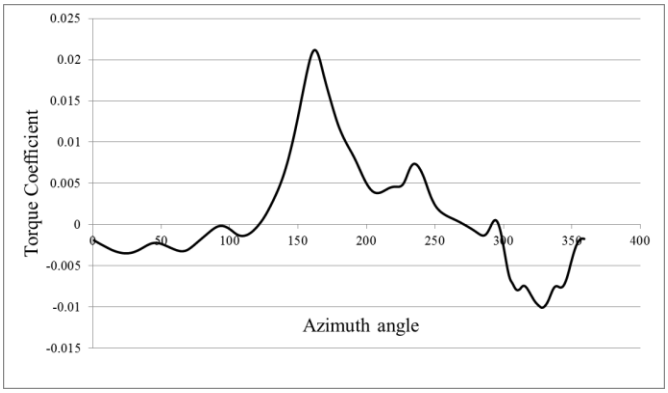

X (mm)	150
Y (mm)	450
α (°)	45

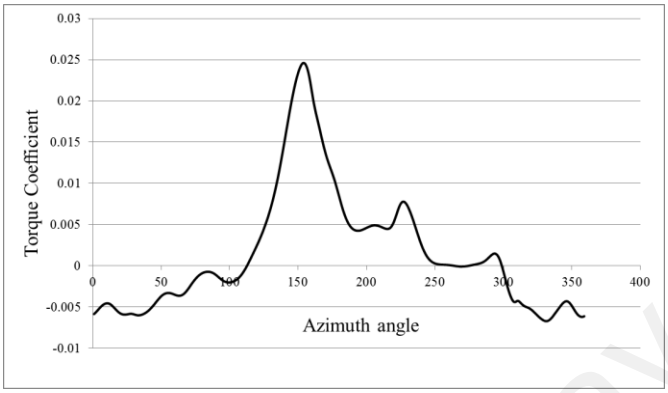

X (mm)	200
Y (mm)	500
α (°)	22.5

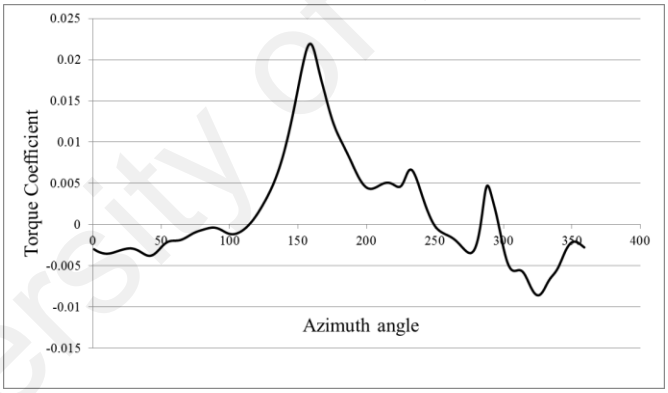

X (mm)	250
Y (mm)	550
α (°)	45

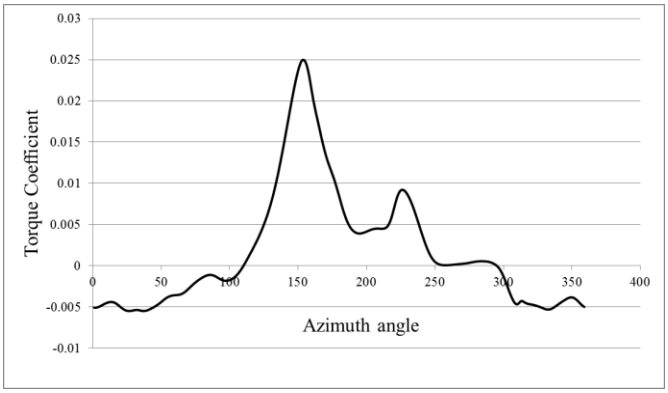

Appendix E2: Torque coefficient vs azimuth angle obtained from CFD simulation for cases of "*Straight Separator plate*"

X (mm)	200
Y (mm)	550
α (°)	45

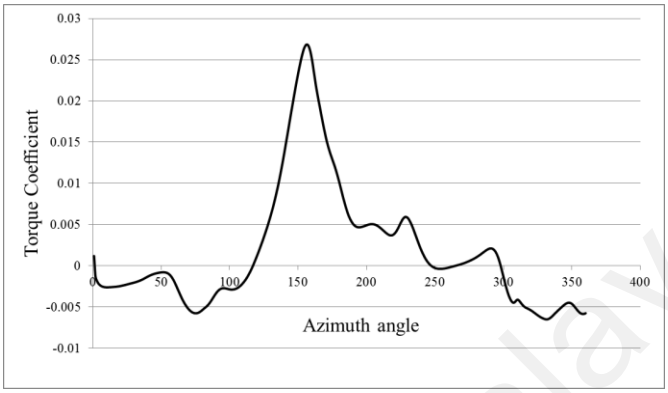

X (mm)	250
Y (mm)	500
α (°)	22.5

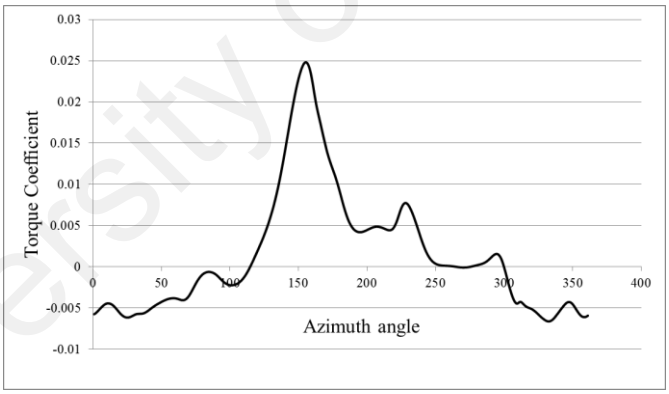

X (mm)	200
Y (mm)	500
α (°)	22.5

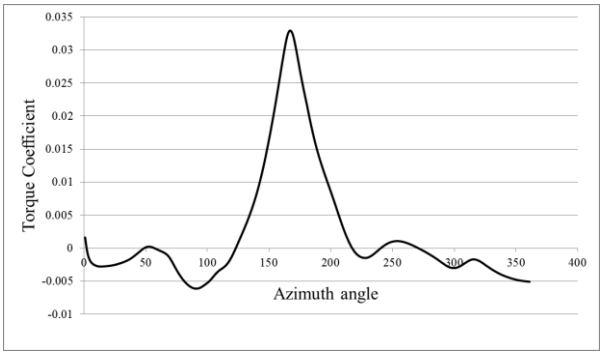

X (mm)	150
Y (mm)	550
α (°)	0

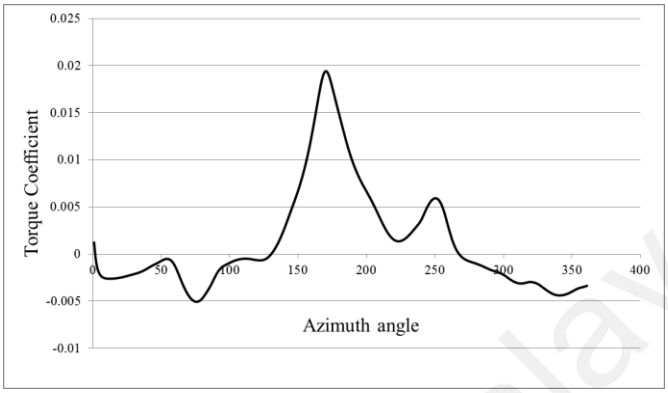

X (mm)	200
Y (mm)	450
α (°)	22.5

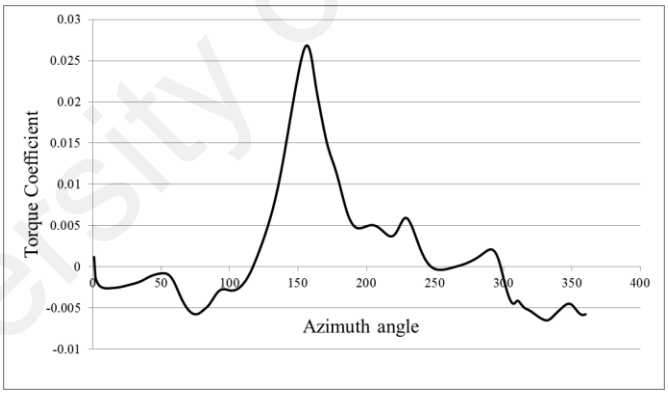

X (mm)	250
Y (mm)	450
α (°)	0

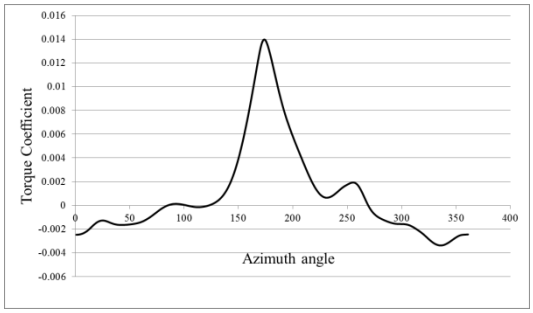

X (mm)	200
Y (mm)	500
α (°)	22.5

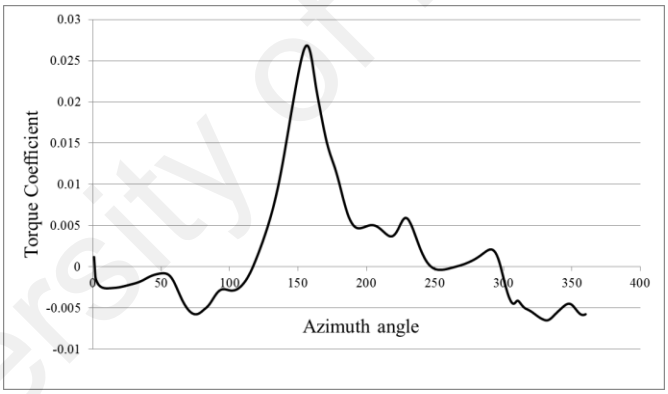

X (mm)	150
Y (mm)	550
α (°)	45

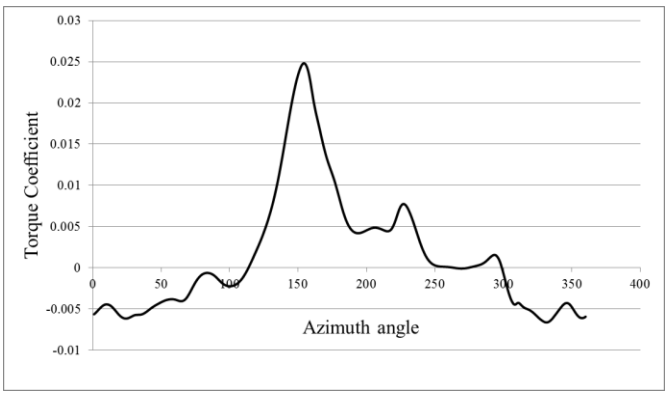

X (mm)	200
Y (mm)	500
α (°)	45

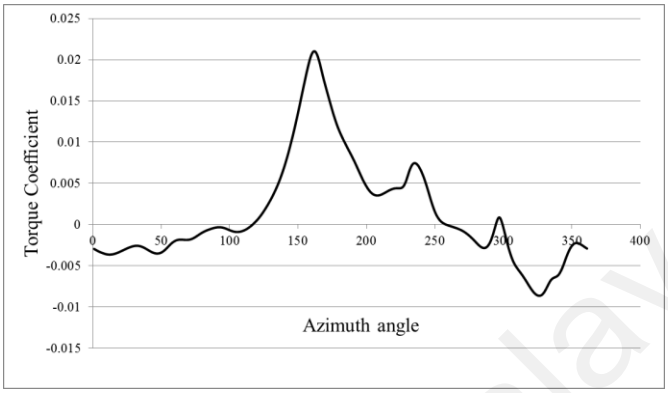

X (mm)	150
Y (mm)	500
α (°)	0

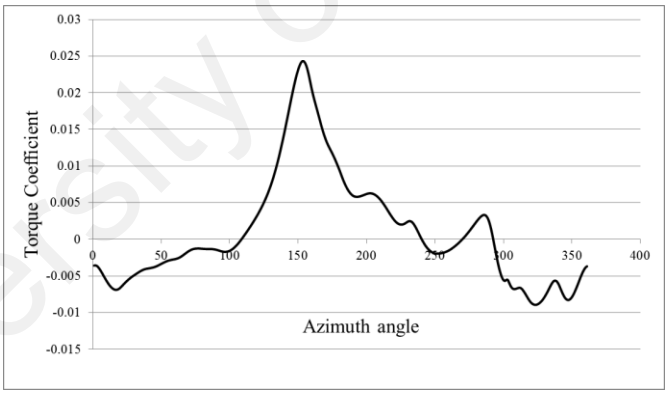

X (mm)	150
Y (mm)	450
α (°)	45

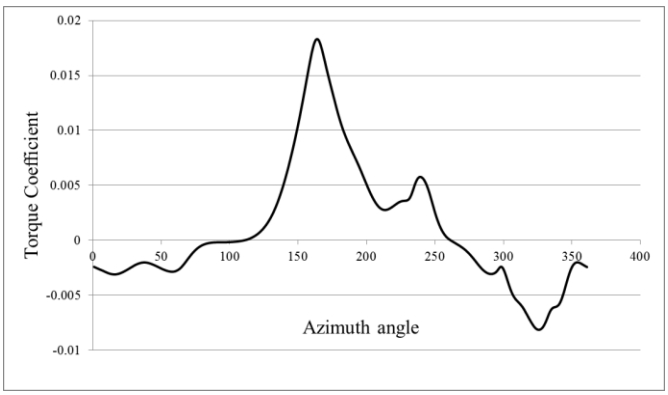

X (mm)	200
Y (mm)	500
α (°)	22.5

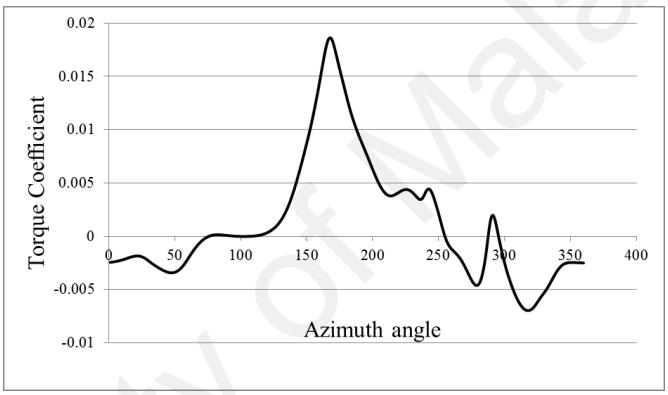

Appendix E3: Torque coefficient vs azimuth angle obtained from CFD simulation for cases of "*Modified Separator plate*"

X (mm)	200
Y (mm)	550
α (°)	45

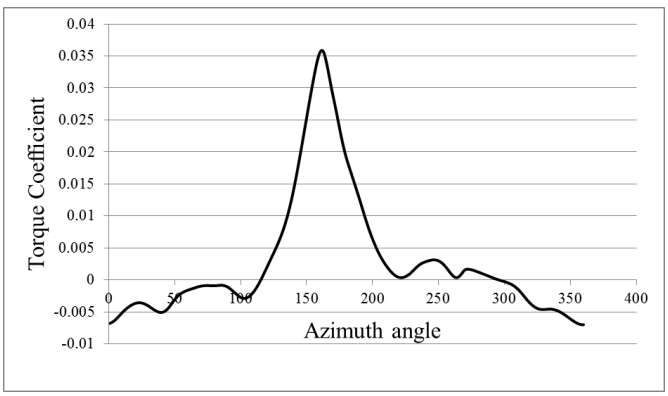

X (mm)	250
Y (mm)	500
α (°)	22.5

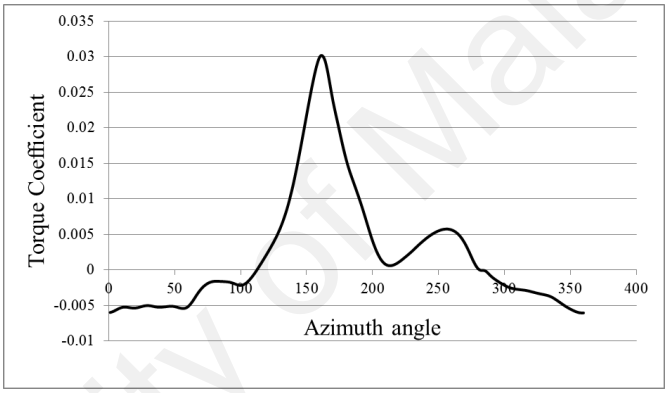

X (mm)	200
Y (mm)	500
α (°)	22.5

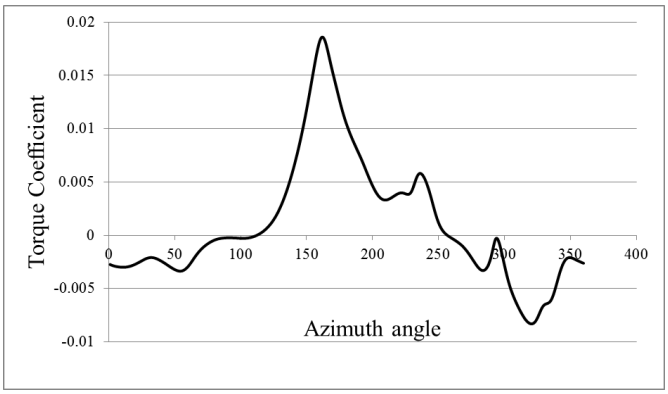

X (mm)	150
Y (mm)	550
α (°)	0

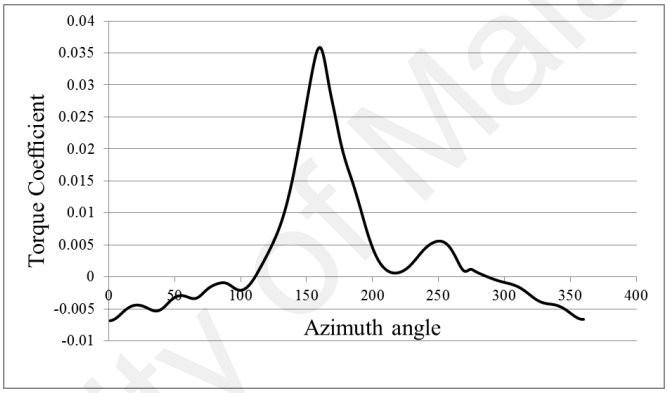

X (mm)	200
Y (mm)	450
α (°)	22.5

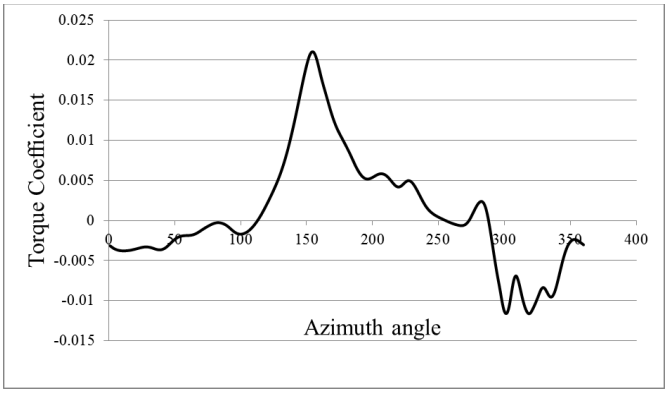

X (mm)	250
Y (mm)	450
α (°)	0

X (mm)	200
Y (mm)	500
α (°)	22.5

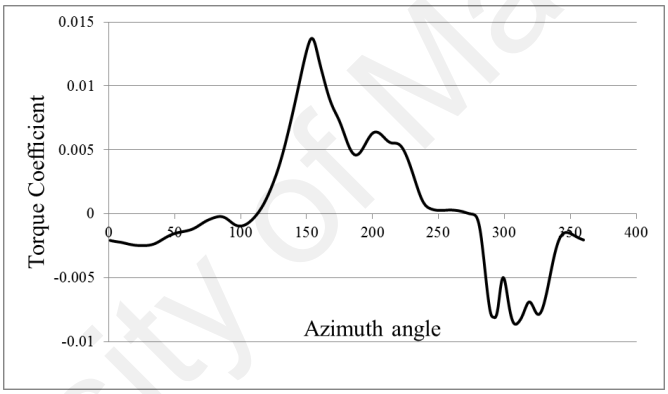

X (mm)	150
Y (mm)	550
α (°)	45

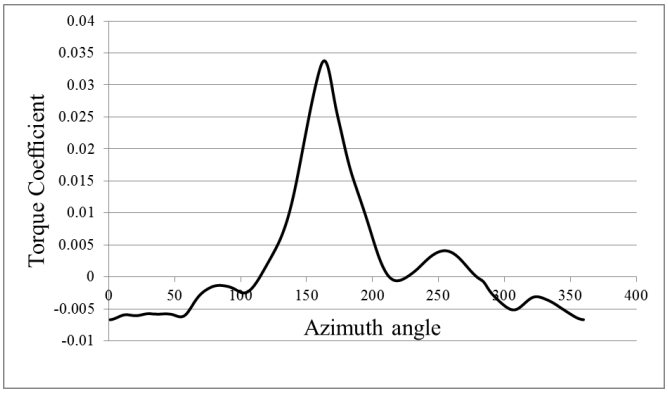

X (mm)	200
Y (mm)	500

α (°)	45

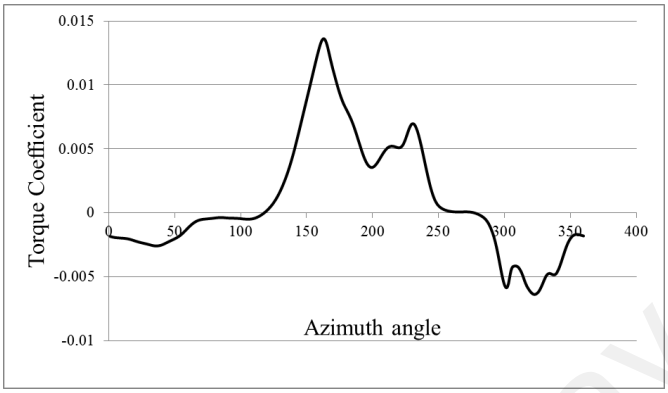

X (mm)	150
Y (mm)	500
α (°)	0

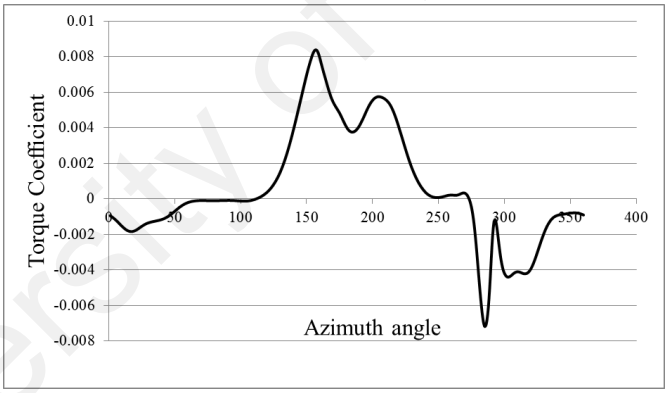

APPENDIX F

Appendix F1: Wind turbine manufacturer's price
(Source: www.hi-vawt.com.tw, sales@hi-vawt.com.tw, October 2015)

HIVAWT Technology Co. Ltd.

No.168, Jhulin 1st Rd., Linkou Township, Taipei County, 244 Taiwan
Tel: +886-2-86014373 Fax: +886-2-86011263
Website: http://www.hi-vawt.com.tw

DISTRIBUTOR PRICE LIST

* * * * * * * * * * * * * * * * * * * *

Part No.	Description of Goods	Order Q'TY (SET)	Package	Unit Price (USD/ SET)
DS-300	Hi Energy VASWT at rated power 300W including wind rotor, generator and controller, but excluding battery nor pole	1 set	Standard	1,800
		10 sets		1,500
		Container base		1,200
DS-700	Hi Energy VASWT at rated power 700W including wind rotor, generator and controller, but excluding battery nor pole	1 set	Standard	4,200
		10 sets		3,700
		Container base		3,200
DS-1500	Hi Energy VASWT at rated power 1.5KW including wind rotor, generator and controller, but excluding battery nor pole	1 set	Standard	11,000
		4 sets		10,000
		Container base	Container	8,500
DS-3000	Hi Energy VASWT at rated power 3KW including wind rotor, generator and controller, but excluding battery nor pole	1 sets	Standard	15,000
		4 sets		13,000
		Container base	Container	11,000
SL04-13024C-00-5	Hybrid street lamp <Fashion design>	1 sets	Standard	5,500
		10 sets		5,000
		Container base		4,500
SL03-2P13060D-00-1	Hybrid street lamp <Economic design>	1 sets	Standard	5,500
		10 sets		5,000
		Container base		4,500

REMARKS:

1. Payment term: 30% downpayment and the balanced 70% by T/T before shipment.
2. Delivery term: FOB Taiwan or Shanghai.
3. Lead time: 30~45 days after receiving the downpayment
4. Validity: 30 days

Appendix F2: Maintenance free battery price from supplier
(Source: ProdigyIntegration, September 2015)

Prodigy Integration (002104272-A)

No.129, Jalan BK 5/6, Bandar Kinrara, 47180 Puchong, Selangor. Tel/Fax: 03-80766809
Email: prodigyintegration@gmail.com

Attention: Jabatan Kejuruteraan Mekanik
Fakulti Kejuruteraan
Universiti Malaya
50603 Kuala Lumpur
Attn: Dr Chong Wen Tong

Date: 29, Sept ,2015

Tel: 03-79577351
Fax:

Re: 290920150001

Quotation

With reference to the above, we are pleased to quote you as follows:-

Item	Product Description	Qty	Price/Unit(RM)	Total Price(RM)
1	YUASA NP65-12 Maintenance-Free Lead-Acid Battery (65AH Capacity)	3	962.00	2,886.00
	GST	1	0.00	0.00
	Grand Total			2,886.00

TERMS AND CONDITIONS:
Price: Quoted in Ringgit Malaysia
Validity: 30 days
Delivery: 2-6 weeks subject to Manufacturer's final confirmation
Payment: 30 days

Prodigy Integration

Fu Chee Ket (Marketing Manager)
Mobile: 019-2108646

Appendix F3: Controller price from supplier
(Source: Prodigy Integration,January 2016)

Prodigy Integration (002104272-A)

No.129, Jalan BK 5/6, Bandar Kinrara, 47180 Puchong, Selangor. Tel/Fax: 03-80766809
Email: prodigyintegration@gmail.com

Attention: Jabatan Kejuruteraan Mekanik
Fakulti Kejuruteraan
Universiti Malaya
50603 Kuala Lumpur
Attn: Dr Chong Wen Tong

Date: 7, Jan ,2016

Tel: 03-79577351
Fax:

Re: 070120160001

Quotation

With reference to the above, we are pleased to quote you as follows:-

Item	Product Description	Qty	Price/Unit(RM)	Total Price(RM)
1	Fabrication of Custom made size Wind & Solar Hybrid Controller Case size : Length 125/175* width 151 * high 66(mm) System rated voltage :12V/24V	2	1,456.00	2,912.00
	Grand Total			2,912.00

TERMS AND CONDITIONS:

Price: Quoted in Ringgit Malaysia
Validity: 30 days
Delivery: 2-6 weeks subject to Manufacturer's final confirmation
Payment: 30 days

Prodigy Integration

Fu Chee Ket (Marketing Manager)
Mobile: 019-2108646